INTERNATIONAL CENTER FOR NUMERICAL METHODS IN ENGINEERING

A Finite Element Method for Solving the Incompressible Navier-Stokes Equations at Low and High Reynolds number using Finite Calculus. Application to Fluid-Structure Interaction

H. Linga

Monograph CIMNE Nº-104, November 2007

A Finite Element Method for Solving the Incompressible Navier-Stokes Equations at Low and High Reynolds number using Finite Calculus. Application to Fluid-Structure Interaction

H. Lynga

Monograph CIMNE Nº-104, **November 2007**

International Center for Numerical Methods in Engineering
Gran Capitán s/n, 08034 Barcelona, Spain

INTERNACIONAL CENTER FOR NUMERICAL METHODS IN ENGINEERING
Edificio C1, Campus Norte UPC
Gran Capitán s/n
08034 Barcelona, sPAIN
www.cimne.upc.es

Fist edition: November 2007

A FINITE ELEMENT METHOD FOR SOLVING THE INCOMPRESSIBLE NAVIER-STOKES EQUATIONS AT LOW AND HIGH REYNOLDS NUMBERS USING FINITE CALCULUS. APPLICATION TO FLUID-STRUCTURE INTERACTION
Monograph CIMNE M104

ISBN: 978-84-96736-33-7

Depósito legal: B-55687-2007

Contents

Acknowledgements

This monograph has been developed as a part of my doctoral studies at the Department of Strength of Materials and Structural Engineering (RMEE), Technical University of Catalonia (UPC), Spain. The work has been carried out at the autonomous research center CIMNE (International Center for Numerical Methods in Engineering).

First of all I would like to express my gratitude to my supervisor Prof. Eugenio Oñate, who is the director of CIMNE.

I would also like to thank the rest of the staff at CIMNE, for many useful discussions about scientific topics related to this monograph as well as for backing up with computer and software resources. A special gratitude is directed to Dr. Pooyan Dadvand, the main developer of KRATOS.

I am also very grateful to Prof. K.-U. Bletzinger and the staff at the Chair of Structural Analysis at Technical University of Munich, Germany, who hosted me during 4 months 2006, during which an important part of this work was realized.

Barcelona, October 2007

Henrik Lyngå

Summary

Introduction

The main objective of this monograph is to develop a stabilized finite element method (FEM) for solving the incompressible Navier-Stokes equations. Using Finite Calculus (FIC), which is a methodology developed by E. Oñate and co-workers at CIMNE (International Center for Numerical Methods in Engineering), flows with a wide range of Reynolds numbers can be modeled. The secondary objective is to test the applicability of the FIC/FEM model to fluid-structure interaction (FSI) emphasizing aero-elasticity. The implementation of the model is carried out within KRATOS, a finite element code for solving multi-physics problems developed at CIMNE.

Convection-Diffusion problem

As the convection-diffusion equation can be regarded as a linear and scalar version of the Navier-Stokes equations governing conservation of momentum and shares the problem of oscillating solutions due to a dominant convection term a whole chapter is dedicated to this equation.

The FIC/FEM model is introduced and its ability to solve the convection-diffusion equation is tested and compared with other standard stabilized methods such like Galerkin/Least-Squares (GLS), Streamline Upwind Petrov-Galerkin (SUPG) etc.

Satisfying results are obtained using linearly as well as quadratically interpolated elements although, besides from being computationally cheaper, the linear results are typically better.

Navier-Stokes equations

Apart from the problems occurring in the presence of a dominant convection term the incompressible Navier-Stokes equations suffer from another source of instability which comes from the fact that the incompressibility condition for some combinations of velocity-pressure interpolation gives rise to incompatibility between these with oscillations in the pressure field as a consequence. One example of this is equal order interpolation which is used in this monograph and obliges the design of stabilized methods in order to obtain physically meaningful results.

The equations are first implemented with a GLS/FEM method which provides the necessary stabilizing effect for the convection term as well as for the incompressibility constraint. Quadratically and linearly interpolated elements are used. The time discretization is carried out with a backward Euler scheme and the global assembled system of equations is solved monolithically. The method is tested and validated by performing simulations of "driven cavity flow" and "flow around cylinder".

The FIC/FEM model for incompressible flow is next derived. The FIC equations are written in the principle curvature directions of the velocity components of the solution and by this manner the desired stabilizing effect is obtained. Moreover, the induced dissipation replaces the need for any additional turbulence model for flows with high Reynolds number. The model is tested for laminar and turbulent flow by simulating "driven cavity flow", "flow around cylinder" and "backward-facing step flow".

An aerodynamic study of a telescope and its enclosing structure is carried out for different positions with respect to the wind inflow.

Fluid-structure interaction

The FIC/FEM model is next extended to an FSI model using a sequential staggered coupling scheme. Flow-induced vibration of a flexible beam is simulated using conforming meshes. The structural domain is constituted of geometrically nonlinear solid elements.

As an aero-elastic FSI application the 750 m tall skyscraper Burj Dubai is modeled assuming that it behaves like a vertical beam with varying cross-section. The wind-induced swaying is simulated.

Using the FSI coupling scheme the airflow around a thin-walled elastic cylinder is simulated. The cylinder is modeled in CARAT which is a code for nonlinear structural dynamics developed by K.-U. Bletzinger and co-workers at the Chair of Structural Analysis, Technical University of Munich. The coupling with the FSI model in KRATOS is done using the software MpCCI. In the flow-induced vibrations of the cylinder the ovalling phenomena can be observed.

Chapter 1

Introduction

1.1 Background

Many challenging areas within multidisciplinary analysis lie in dealing with fluid-structure interaction (FSI) types of problem. FSI indeed has a wide range of applications within very different fields. In bioengineering such as interaction between blood flow and blood vessels, in marine engineering or aeronautics different kinds of shape optimization problems or in civil engineering such as simulation of the dynamic behavior of flexible structures subjected to wind load.

The latter is of certain interest as the wind effect becomes a more dominant factor when the design process goes towards building lighter and taller structures. One example is the air control tower at Sturup airport in Malmö, Sweden, which sways when the wind lies on to such extent that the staff becomes seasick and have to go home.

A suspension bridge is a structure which can be brought to fluttering at a certain wind speed. This might cause damage or in the worst case lead to collapse, as for the Tacoma bridge, USA [47]. It had only been open for traffic for a few months. Another suspension bridge, the Great Belt bridge in Denmark, has been subjected to an aerodynamic analysis using a fluid-rigid body model in [43].

A different kind of project under development which constitutes an interesting and challenging application to FSI is the design and construction of an extremely large telescope (ELT) on the island of La Palma, the Canary Islands.

It is by far the world´s largest optics telescope. The consortium in charge of performing a design study of this project consists of partners from Finland, Ireland, Spain, Sweden and UK [45]. According to this study the diameter of the primary mirror is 50 meters wide and built up by 618 hexagonal segments, each held in position by three actuators on the back side. The advanced adaptive optics system responsible for keeping the mirror segments in position has to take into account the gravity load, temperature changes and wind effects.

The wind is probably the most difficult part to predict. One preliminary aerodynamic analysis of the telescope structure is done in [46]. It provides some data about the quality of ventilation and temperature distribution inside the enclosure

of the telescope. The study also gives an idea of the actions by the wind on the telescope.

Besides from static wind load, which creates significant forces on the mirror segments and on the tripod structure bearing the secondary mirror, dynamic wind effects must be considered as they may excite eigenmodes on the structure. Another effect is turbulence close to the mirror segments, which is to be held at its minimum as it disturbs the optics quality.

In recent years the numerical modeling of FSI has become a focus of major research activity, see e.g. [35] for a review of the field. One main categorization of solution strategies for FSI problems can be based on whether the fluid and the structure are strongly or weakly coupled.

The former is used in [36] where the set of nonlinear equations are solved based on the Newton-Raphson methodology and incorporates the full linearization of the problem. In [37] shape optimization with respect to drag force of a flexible body in a surrounding fluid is carried out using strong coupling and an approximate Newton method.

Weak coupling is characterized by the presence of different solvers for the fluid and the structure and the data at the interface being transferred between the domains using so-called staggered solution algorithms, see e.g. [38].

An iterative staggered scheme with substructured computation of a relaxation parameter is presented in [39], where interaction of thin-walled structures with incompressible viscous fluid is solved.

In [40] code coupling is used for FSI problems involving membranes as well as thin-walled shell structures. These highly specialized models for nonlinear structural dynamics are parts of CARAT (Computer Aided Research Analysis Tool), the in-house code developed at the Chair of Structural Analysis at the Technical University of Munich, Germany. In [41] a strategy for numerical form finding of membranes is outlined.

The advantage of using different solvers is the freedom of combining highly specialized codes for each physical domain. However the coupling issues become more complex.

1.1.1 New features in stabilization techniques

When comes to modeling air flow a fluid model governed by the incompressible Navier-Stokes equations is suitable. Finding a numerical solution to this problem is a task where special considerations have to be taken. It is well known that standard numerical methods such as the Galerkin finite element method lead to unstable solutions when applied to problems involving different scales, multiple constraints and/or high gradients. These situations typically appear when dealing with the Navier-Stokes equations or the related convection-diffusion equation.

One of the sources of instability is due to the diffusion term being underestimated in relation to the convection term in the numerical approximation. There exist numerous of stabilization techniques in order to deal with this problem, the

most classical one being the SUPG method as described in Codina [1] where also optimal upwind functions are derived for linear as well as for quadratic elements. Comparison with other stabilization approaches is carried out in [2] ranging from the Galerkin/least-squares (GLS) and the subgrid scales (SGS) method, first introduced by Hughes [3], to the Characteristic Galerkin (CG) and the Taylor-Galerkin method.

Essentially, the effect of applying any of these methods is that a stabilizing term is added to the original Galerkin formulation of the problem. These methods are also compared in [5], together with the Finite Calculus (FIC) approach. The FIC method, developed by Oñate and co-workers [6], is a consistent procedure to reformulate the differential equations governing a multiphysics problem by introducing new terms involving characteristic space and/or time dimensions. In the case of the convection-diffusion equation this is achieved by invoking the balance of flux in a finite domain and the terms induced when bringing the balance equation back to the continuous level contain the necessary stabilizing effect.

A recent development within FIC is presented in [7] and consists in writing the governing equations in the principle curvature axes of the solution. This introduces an orthotropic diffusion which stabilizes the numerical solution both in smooth regions and in the presence of sharp gradients.

The possibilities of FIC are further outlined in [8] which apart from the convection-diffusion problem include treatment of incompressible fluids and solids.

The second source of numerical instabilities when obtaining a numerical solution to the incompressible Navier-Stokes equations using the Galerkin method is the incompressibility constraint which causes spurious pressure oscillations if the finite element spaces interpolating the velocity and the pressure fields do not satisfy the so-called Babuska-Brezzi (LBB) stability condition, see [10]. Equal order interpolation does not accomplish the LBB condition and therefore has to be treated by means of stabilizing methods. In [11] a finite element formulation for solving the Stokes problem using equal order velocity-pressure interpolation is presented. More stability issues regarding the incompressible Navier-Stokes equations, also including Coriolis forces and permeability of the medium, are discussed in [12] where a method stabilized by means of SGS is set up and solved using a monolithic time integration scheme. In [13] pressure stability of fractional step methods is analyzed with and without pressure gradient projection.

The development of arbitrary Lagrangian-Eulerian (ALE) methods in order to solve fluids in moving domains was an attempt to combine the advantages of the Lagrangian approach and the Eulerian one. Lagrangian algorithms, in which each individual node of the computational mesh follows the associate material particle during motion, are mainly used in structural mechanics but also in computational fluid dynamics (CFD), for example in the recently developed particle finite element method (PFEM) [14]. In the Eulerian algorithms, being the more commonly used in CFD, the computational mesh is fixed and the continuum moves freely with respect to the grid. This freedom allows large distortions to be handled but at the expense of precise interface definition. In the ALE approach the grid is moved arbitrary,

independently of the continuum, and thus it applies very well to FSI problems with a time changing fluid domain. An in-depth survey of ALE methods is found in [15] where also various mesh displacement prescription algorithms are reviewed. In [16] an ALE method is used for a wind engineering application for controlling bridge profiles and tested comparing first order and second order time accuracy.

In [18] a finite element method for solving a fluid with surface waves interacting with a completely or partly submerged body is presented. The fluid problem is formulated in an ALE framework with the FIC method, which provides the necessary stabilization for the pressure and the convection term, and solved using a semi-implicit fractional step scheme. A mesh updating technique based on solving a fictitious elastic problem in the fluid domain is set up.

In this monograph, in particular the modeling of air flows is addresses, which typically have high Reynolds numbers, and hence one has to deal with turbulence phenomena. Turbulence is characterized by the presence of large differences between the scales in the flow pattern. These differences increase with the Reynolds number. The typical treatment of this effect is to average the large scale entities in time or space. The smaller scales are left unresolved but the effect of them on the large scale has to be modeled, often in terms of the so-called Reynolds stress tensor, scaled by the turbulent viscosity. In [20] an overview of existing turbulence models is given. Within the Reynolds-Averaged-Navier-Stokes (RANS) family of methods, the $k-\epsilon$ method is perhaps the most popular one, where the turbulent viscosity is calculated from an estimation of the turbulent kinematic energy level and its dissipation rate. The other big family of methods is Large-Eddy-Simulation (LES) where the turbulent viscosity depends on the grid-size. It is computationally more expensive than RANS methods as it requires a finer grid but provides more accurate results.

In [22] an LES formulation is developed from the variational multiscale method. In [23], also using the variational multiscale method and separation in three scales, the close relationship between stabilized numerical methods and turbulence modeling is discussed and the possibilities of this approach to serve these two, at first sight different, goals: stabilization and accounting for the physical effects from the numerically unresolved scales.

This duality is also present in the FIC method. In [25], following the ideas of writing the FIC equations in the direction of the principle curvature axes of the solution, a matrix form of the stabilization parameters is obtained. Apart from providing the necessary numerical stabilization this allows to model a wide range of flow problems for low and high Reynolds numbers, without introducing a turbulence model. This will be the approach to be followed in the monograph.

1.2 Formulation of the problem

A finite element method for solving the incompressible Navier-Stokes equations using the Finite Calculus approach is presented and its adaptivity for fluid-structure interaction problems is investigated. The model is suited to aero-elastic problems where flexible structures are subjected to moderate deformations under the influence of wind load. The dynamic response of large scale ground structures is analyzed.

1.3 Procedure of solving the problem

All programming is done in C++ within the framework of KRATOS, a finite element code for solving multi-physics problems [42]. For pre- and postprocessing is used GiD, www.gidhome.com/. The procedure of solving the presented task can be summarized in the following order.

- Trying out methods of stabilization for the convection-diffusion equation with emphasis laid on the Finite Calculus (FIC) technique
- Defining a fluid model governed by the incompressible Navier-Stokes equations stabilized by means of the GLS method
- Writing the equations in an arbitrary Lagrangian Eulerian (ALE) form and setting up a mesh moving strategy
- Setting up the incompressible fluid model using FIC in the principle curvature direction
- Validation of the fluid model by comparing numerical results to other works and to experimental results
- Aerodynamic analysis of an extremely large telescope
- Establishing an FSI algorithm in Kratos
- Aero-elastic analysis of a swaying tower in 3D
- Code coupling between the fluid solver in KRATOS and a structure solver in the structural code CARAT for FSI analysis

1.4 Layout

In Chapter 2 the convection diffusion equation is implemented. Starting with linear finite elements and using a one-dimensional formulation in Section 2.1 numerical results using the FIC method are compared to those obtained by other standard stabilization methods. In Section 2.2 the formulation is extended to two dimensions

and the FIC equations are written in the principle curvature directions, here approximated to the gradient. The formulation is next extended to quadratic finite elements where the actual principle curvature directions are used. The one-dimensional case is presented in Section 2.3 using 3-noded line elements and the two-dimensional case in Section 2.4 where 6-noded triangles are used. The outcome of this chapter is a completely stable method to solve the convection-diffusion equation by means of the FIC technique using linear and quadratic elements. However, besides from being computationally cheaper, the linear results are typically better.

In Capter 3 the incompressible Navier-Stokes equations are dealt with and in the first Section 3.1 they are stabilized using the GLS method. Linear as well as quadratic approximation of equal order is employed and the equations are solved monolithically. In Section 3.2 the formulation is extended to an ALE framework in order to account for a moving mesh. In Section 3.3 the FIC/FEM model for an incompressible flow is set up and solved using a fractional step scheme. Linear elements of equal order approximation are used. An algorithm for computation of the characteristic length tensor h_{ij} is explained. Numerical examples are presented for flows with low and high Reynolds numbers. These are "driven cavity flow", "flow around cylinder" and "backward-facing step flow". Last, an aerodynamic simulation of a telescope is carried out.

In Chapter 4 the ability of the FIC/FEM model to simulate fluid-structure interaction (FSI) problems with emphasis on aero-elasticity is investigated. The dynamic behavior of ground structures subjected to wind load is of interest. In Section 4.1 the fluid solver is outlined. This includes the FIC/FEM model and the mesh moving strategy, which are repeated here. Next in Section 4.2 the FSI interface via KRATOS is explained. The coupling scheme is defined and an application to the skyscraper Burj Dubai is performed. Finally, in Section 4.3, the structural code CARAT is coupled to KRATOS and airflow around an elastic cylinder is simulated.

Chapter 2

Convection-Diffusion problem

When solving a multiscale problem the solution may vary in different orders of magnitude. Solving the convection-diffusion problem is an example when such effects have to be dealt with. If the convection term is dominant, sharp gradients at the boundary or at internal layers may occur and if the approximation is of "central difference-type"($\frac{dT}{dx} \approx \frac{T_{i+1}-T_{i-1}}{2l}$), as in the case of standard Galerkin finite element procedure, numerical instabilities will follow. Therefore it is necessary that the mathematical model provides some sort of stabilization. For the finite element formulation of a simple convection-diffusion problem different methods of stabilization are tried out using linear and quadratic elements [1],[5],[2].

Special consideration is given the Finite Calculus (FIC) method, developed by E. Oñate and co-workers [8],[6]. A Lagrangian finite element formulation is tested on the FIC-equation expressed in the principle curvature directions of the solution as proposed in [7]. The numerical results are compared to other standard stabilized methods, such like the Petrov-Galerkin, the Streamline Upwind Petrov-Galerkin (SUPG) and the Galerkin-Least squares (GLS).

Using first finite elements with linear approximation, in Section 2.1 the equations are implemented in one dimension and in Section 2.2 the two-dimensional case is presented. Thereafter, in Sections 2.3 and 2.4, the same is done using quadratic approximation.

2.1 One-dimensional linear formulation

By introducing the heat equation in steady state in a one-dimensional (1D) domain Ω, the simplest possible form of the convection-diffusion equation is achieved.

$$\begin{aligned} u\frac{dT}{dx} - k\frac{d^2T}{dx^2} - Q = 0 \qquad & in\ \Omega \\ T = \overline{T} \qquad & on\ \partial\Omega \end{aligned} \tag{2.1}$$

The convection term is governed by the constant velocity u, the diffusion term by the heat conductivity k. T is the temperature and Q the distributed heat source.

The boundary conditions are here assumed to be of Dirichlet type. No Neumann boundary condition is considered.

Introducing the weighted residual method and the following functional spaces

$$\begin{aligned} S &= [v \epsilon H^1(\Omega) | v = \overline{T} \ on \ \partial\Omega] \\ V &= [v \epsilon H_0^1(\Omega)] \end{aligned} \tag{2.2}$$

and integrating by parts the weak form is constituted in finding $T \epsilon S$ such that

$$\begin{aligned} \int_\Omega \left(wu\frac{dT}{dx} + k\frac{dw}{dx}\frac{dT}{dx} \right) \, d\Omega &= \int_\Omega wQ \, d\Omega \qquad in \ \Omega \\ T &= \overline{T} \qquad on \ \partial\Omega \end{aligned} \tag{2.3}$$

for all $w \epsilon V$

2.1.1 Unstabilized scheme

To solve the problem the standard Galerkin FEM is used. The temperature field is approximated by linear finite elements and the element length is denoted with l^e. Introducing the following finite element spaces

$$\begin{aligned} S_h &= [v \epsilon H^1(\Omega) | v \epsilon P^1(\Omega^e) | v = \overline{T} \ on \ \partial\Omega] \\ V_h &= [v \epsilon H_0^1(\Omega) | v \epsilon P^1(\Omega^e)] \end{aligned} \tag{2.4}$$

the discretized weak form of the differential equation (2.1) is written as

Find $T_h \epsilon S_h$ such that

$$\begin{aligned} \int_\Omega \left(w_h u\frac{dT_h}{dx} + k\frac{dw_h}{dx}\frac{dT_h}{dx} \right) \, d\Omega &= \int_\Omega w_h Q \, d\Omega \qquad in \ \Omega \\ T_h &= \overline{T} \qquad on \ \partial\Omega \end{aligned} \tag{2.5}$$

for all $w_h \epsilon V_h$.

In Figure 2.2 the solution of the unstabilized scheme is plotted. The solution is oscillating and this is because the diffusion is too small compared to the convection for a given element size. This critical relationship is quantified in the so-called Peclet number, $\gamma = \frac{ul^e}{2k}$ which quantifies the need for stabilization.

The reason for the oscillation induced by the Galerkin method can be explained using a central difference scheme, which coincides with the Galerkin FEM using linear elements. The discretized equations can therefore be written as

$$u\frac{dT}{dx} - k\frac{d^2T}{dx^2} \simeq u\frac{T_{i+1} - T_{i-1}}{2l^e} - k\frac{T_{i+1} - 2T_i + T_{i-1}}{(l^e)^2} = 0$$

where T_i are the nodal unknowns. For the sake of simplicity the source term Q is left out.

T_i can be expressed in terms of T_{i+1} and T_{i-1}

$$\frac{2k}{(l^e)^2}T_i = T_{i+1}\left(\frac{k}{(l^e)^2} - \frac{u}{2l^e}\right) + T_{i-1}\left(\frac{k}{(l^e)^2} + \frac{u}{2l^e}\right)$$

Clearly if the term multiplying T_{i+1} is less than zero, or equivalently the Peclet number is greater than one,

$$\left(\frac{k}{(l^e)^2} - \frac{u}{2l^e}\right) < 0 \Leftrightarrow \frac{k}{(l^e)^2} < \frac{u}{2l^e} \Leftrightarrow \gamma > 1$$

and furthermore assuming $T_{i+1} > T_{i-1}$ and all other parameters positive, a non-physical result will yield, namely $T_i < T_{i-1}$. T_i is expected to be between T_{i-1} and T_{i+1} or at least coincide with T_{i-1}.

2.1.2 Upwinding methods

The trick to avoid T_i taking spurious non-physical values leading to oscillations in the solution is pushing the central difference $(T_{i+1} - T_{i-1})$ of the convection term towards $(T_i - T_{i-1})$. The approximation of $\frac{dT}{dx}$ is in this case said to be "upwinded". The approximated equation for the node i is now

$$u\frac{dT}{dx} - k\frac{d^2T}{dx^2} \simeq u\frac{\theta T_{i+1} + (1-\theta)T_i - T_{i-1}}{l^e(1+\theta)} - k\frac{T_{i+1} - 2T_i + T_{i-1}}{(l^e)^2} = 0$$

where θ is introduced, $(0 \leq \theta \leq 1)$. $\theta = 0$ means full upwinding whereas for $\theta = 1$ the central difference scheme is recovered. Now the following expression for T_i is obtained

$$\left(\frac{2k}{(l^e)^2} + \frac{u(1-\theta)}{l^e(1+\theta)}\right)T_i = T_{i+1}\left(\frac{k}{(l^e)^2} - \frac{\theta u}{l^e(1+\theta)}\right) + T_{i-1}\left(\frac{k}{(l^e)^2} + \frac{u}{l^e(1+\theta)}\right)$$

Solving the critical value of θ in order not to obtain non-physical value of T_i gives the following result.

$$\begin{aligned} \theta &= 1 \qquad && for\ \gamma \leq 1 \\ \theta &= \frac{1}{\frac{ul^e}{k} - 1} \qquad && for\ \gamma > 1 \end{aligned} \tag{2.6}$$

2.1.3 Artificial diffusion scheme

A popular stabilizing method is the so-called artificial diffusion scheme [5] where the upwinding effect is achieved by simply increasing the heat conductivity parameter k with an artificial term according to

$$k := k + \alpha\frac{ul^e}{2} \tag{2.7}$$

where the parameter α is given as

$$\alpha = 1 - \frac{1}{\gamma} \qquad \text{critical value, ensuring a physical stable solution}$$
$$\alpha = \coth\gamma - \frac{1}{\gamma} \qquad \text{optimal value, providing exact solution at nodes}$$

Using the optimal value of α the result of this scheme is well stabilized as shown in Figure 2.2. However, the idea of having to change the physical properties to achieve it is somewhat unsatisfactory.

2.1.4 Petrov-Galerkin method

In this approach the upwinding effect is achieved by modifying the test function w according to (2.8)

$$w = w + \frac{\alpha l^e}{2}\frac{dw}{dx} \tag{2.8}$$

where the optimal value of α is adapted.

Integrating by parts, approximating T and choosing w in the piece-wise linear finite element spaces S_h and V_h following scheme arises.

Find $T_h \epsilon S_h$ such that

$$\int_\Omega \left(w_h u \frac{dT_h}{dx} + \frac{dw_h}{dx} k \frac{dT_h}{dx} \right) d\Omega + \sum_e \int_{\Omega^e} \frac{\alpha l^e}{2} \frac{dw_h}{dx} u \frac{dT_h}{dx}\, d\Omega = \int_\Omega w_h Q\, d\Omega + \int_{\Omega^e} \frac{\alpha l^e}{2} \frac{dw_h}{dx} Q\, d\Omega \qquad in\ \Omega$$
$$T_h = \overline{T} \qquad on\ \partial\Omega \tag{2.9}$$

for all $w_h \epsilon V_h$. It should be pointed out that in case of $Q = 0$ this is equivalent to the artificial diffusion scheme.

2.1.5 Finite Calculus

By means of the Finite Calculus method (FIC) [6] the original differential equation

$$u\frac{dT}{dx} - k\frac{d^2T}{dx^2} - Q = 0 \tag{2.10}$$

is first written in terms of heat flux q

$$\frac{dq}{dx} - Q = 0 \qquad \text{where} \qquad q(x) = u \cdot T(x) - \frac{dT}{dx}$$

If linear distribution of the heat source is assumed the balance of fluxes in a finite domain of length l, see figure 2.1, is expressed according to

$$q_A - q_B + l\frac{Q_A + Q_B}{2} = 0 \tag{2.11}$$

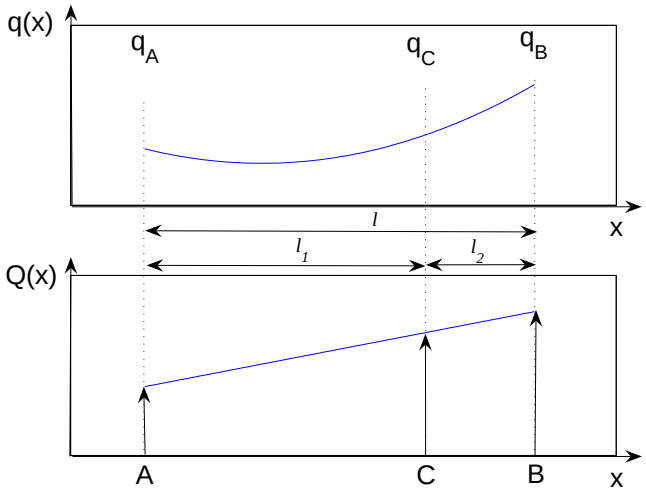

Figure 2.1: Balance of flux in a finite domain.

An arbitrary point C is defined around which the above quantities can be approximated using Taylor expansion

$$\begin{aligned} q_A &= q_C - l_1\frac{dq}{dx}|_C + \frac{l_1^2}{2}\frac{d^2q}{dx^2}|_C + \mathcal{O}(l^3) \\ q_B &= q_C + l_2\frac{dq}{dx}|_C + \frac{l_2^2}{2}\frac{d^2q}{dx^2}|_C + \mathcal{O}(l^3) \\ Q_A &= Q_C - l_1\frac{dQ}{dx}|_C + \mathcal{O}(l^2) \\ Q_B &= Q_C + l_2\frac{dQ}{dx}|_C + \mathcal{O}(l^2) \end{aligned}$$

and substituting in (2.11) leads to the following expression

$$-l\frac{dq}{dx}|_C + \frac{l_1^2 - l_2^2}{2}\frac{d^2q}{dx^2}|_C + l\cdot\left(Q_C + \frac{l_1 - l_2}{2}\frac{dQ}{dx}|_C\right) = 0$$

Division by $(-l)$, introducing the characteristic length $h = l_1 - l_2$ and making the definition that the quantities at point C now yield at the continuous level the finite

calculus equation is obtained which together with the Dirichlet boundary conditions is written as

$$u\frac{dT}{dx} - k\frac{d^2T}{dx^2} - Q - \frac{h}{2}\frac{d}{dx}\left(u\frac{dT}{dx} - k\frac{d^2T}{dx^2} - Q\right) = 0 \qquad in\ \Omega$$
$$T = \overline{T} \qquad on\ \partial\Omega \tag{2.12}$$

Applying the Galerkin FEM to this equation, using the piece-wise linear finite element spaces defined above, leads to the following discretized weak form.

For all $w_h \epsilon V_h$ find $T_h \epsilon S_h$ such that

$$\int_\Omega \left(w_h u\frac{dT_h}{dx} + k\frac{dw_h}{dx}\frac{dT_h}{dx}\right)\, d\Omega + \int_{\Omega^e} \frac{dw_h}{dx}\frac{h}{2}u\frac{dT_h}{dx}\, d\Omega =$$
$$\int_\Omega w_h Q\, d\Omega + \int_{\Omega^e} \frac{dw_h}{dx}\frac{h}{2}Q\, d\Omega \qquad in\ \Omega$$
$$T_h = \overline{T} \qquad on\ \partial\Omega \tag{2.13}$$

Taking the value of the characteristic length as $h = \alpha \cdot l^e$ using the same optimal value of $\alpha = \coth\gamma - \frac{1}{\gamma}$ makes the FIC scheme equivalent to the Petrov-Galerkin scheme as well as to the artificial diffusion scheme. Figure 2.2 shows an example with velocity pointing towards the right and Dirichlet conditions creating a sharp gradient at the right boundary.

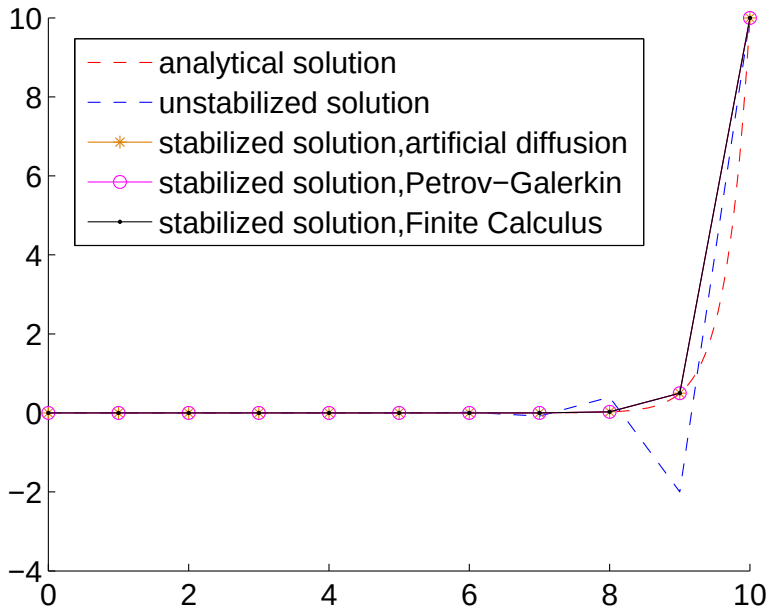

Figure 2.2: 1D element mesh with 10 element of length $l^e = 1$, Peclet number $\gamma = 1.5$, no heat source

2.2 Two-dimensional linear formulation

The heat equation with only Dirichlet conditions in steady state is introduced in 2D

$$\begin{aligned} u_j \frac{\partial T}{\partial x_j} - k \frac{\partial^2 T}{\partial x_j^2} - Q = 0 \qquad & in\ \Omega \\ T = \overline{T} \qquad & on\ \partial\Omega \end{aligned} \tag{2.14}$$

where $j = 1, 2$

Introducing the following functional spaces

$$\begin{aligned} S = [v \epsilon H^1(\Omega) | v = \overline{T}\ on\ \partial\Omega] \\ V = [v \epsilon H_0^1(\Omega)] \end{aligned} \tag{2.15}$$

the weighted residual method is adapted and the weak form of the unstabilized 2D problem after integrating by parts takes the following shape. Find $T \epsilon S$ such that

$$\begin{aligned} \int_\Omega \left(w u_j \frac{\partial T}{\partial x_j} + k \frac{\partial w}{\partial x_j} \frac{\partial T}{\partial x_j} \right) d\Omega = \int_\Omega wQ\ d\Omega \qquad & in\ \Omega \\ T_h = \overline{T} \qquad & on\ \partial\Omega \end{aligned} \tag{2.16}$$

for all $w \epsilon V$

2.2.1 Unstabilized scheme

Using piecewise linear finite element spaces

$$\begin{aligned} S_h = [v \epsilon H^1(\Omega) | v \epsilon P^1(\Omega^e) | v = \overline{T}\ on\ \partial\Omega] \\ V_h = [v \epsilon H_0^1(\Omega) | v \epsilon P^1(\Omega^e)] \end{aligned} \tag{2.17}$$

the discretized weak form of the unstabilized 2D problem is set up as follows.

Find $T_h \epsilon S_h$ such that

$$\begin{aligned} \int_\Omega \left(w_h u_j \frac{\partial T_h}{\partial x_j} + k \frac{\partial w_h}{\partial x_j} \frac{\partial T_h}{\partial x_j} \right) d\Omega = \int_\Omega w_h Q\ d\Omega \qquad & in\ \Omega \\ T_h = \overline{T} \qquad & on\ \partial\Omega \end{aligned} \tag{2.18}$$

for all $w_h \epsilon V_h$

Below the 1D-problem is represented in a 2D domain by extending the y-axis so that a unit square is obtained. The domain is meshed with 200 triangular elements and the following result is obtained using the above unstabilized scheme.

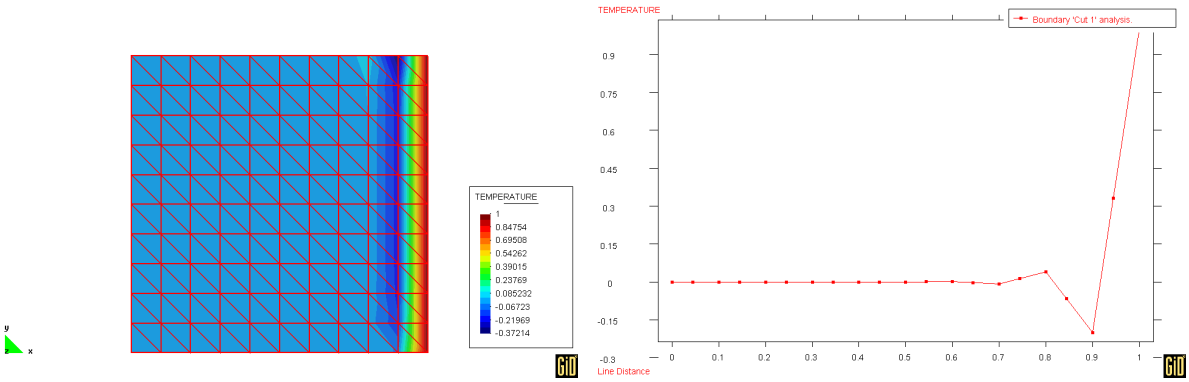

Figure 2.3: Structured mesh with linear triangles of meshsize $l^e = 0.1$, Peclet number $\gamma = 1.5$, no heat source

2.2.2 Streamline Upwind Petrov Galerkin method

The stabilization method in the multidimensional case that corresponds to the Petrov-Galerkin scheme is the so-called Streamline Upwind Petrov Galerkin scheme (SUPG). The "modification" of the test function w is expressed as a perturbation function $\mathcal{P}$ acting on w multiplied by a stabilization parameter τ with dimensions of time. Perturbed Galerkin forms can be written in a general form as

$$\int_\Omega \left(w u_j \frac{\partial T}{\partial x_j} + k \frac{\partial w}{\partial x_j} \frac{\partial T}{\partial x_j} - wQ \right) \, d\Omega + \Sigma_e \int_{\Omega^e} \tau^e \cdot \mathcal{P}(w) \cdot r \, d\Omega = 0 \qquad (2.19)$$

where r expresses the residual of the original differential equation and τ^e is element-wise evaluated. If $\mathcal{P} := u_j \frac{\partial}{\partial x_j}$ and $\tau^e = \frac{\alpha \cdot l^e}{2|u|}$ the stabilization term emerging from this scheme has the properties of the one described in the Petrov-Galerkin 1D-case. Furthermore, it is in the "streamline" direction, the direction of the velocity. Moreover, element-wise integration and summation of the perturbation term is required because $\frac{\partial w_h}{\partial x_j}$ is discontinuous across the element boundaries.

Excluding terms that are zero due to the linear interpolation the discretized weak form is set up as following. Find $T_h \epsilon S_h$ such that

$$\int_\Omega \left(w_h u_j \frac{\partial T_h}{\partial x_j} + k \frac{\partial w_h}{\partial x_j} \frac{\partial T_h}{\partial x_j} \right) \, d\Omega + \Sigma_e \int_{\Omega^e} \tau^e \cdot u_k \frac{\partial w_h}{\partial x_k} \cdot u_j \frac{\partial T_h}{\partial x_j} \, d\Omega =$$
$$\int_\Omega w_h Q \, d\Omega + \Sigma_e \int_{\Omega^e} \tau^e \cdot u_k \frac{\partial w_h}{\partial x_k} \cdot Q \, d\Omega \qquad in \ \Omega$$
$$T_h = \overline{T} \qquad on \ \partial\Omega \qquad (2.20)$$

for all $w_h \epsilon V_h$. As the stabilization parameter τ^e tends to zero when the approximation is fine enough the SUPG, as well as other Galerkin forms will approach the exact solution and are said to be consistent. This is also the case for the Finite Calculus approach.

Here are the perturbation functions for some other Galerkin forms [5]

$$\begin{aligned} \text{Galerkin/Least-Squares (GLS)} \quad & \mathcal{P} := u_j \frac{\partial}{\partial x_j} - k \frac{\partial^2}{\partial x_j^2} \\ \text{Subgrid Scales (SGS)} \quad & \mathcal{P} := u_j \frac{\partial}{\partial x_j} + k \frac{\partial^2}{\partial x_j^2} \end{aligned}$$

However, since the finite element approximation is linear, the second derivative term vanishes and these methods reduce to the SUPG method.

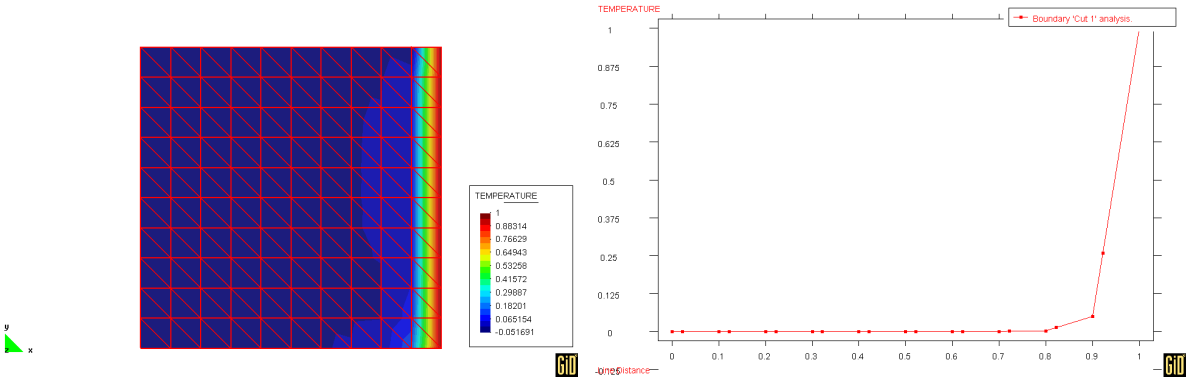

Figure 2.4: Mesh with linear triangles $l^e = 0.1$, $\gamma = 1.5$, no heat source. SUPG.

Figure 2.4 shows an SUPG stabilized solution of a problem where the velocity vector has the same direction as the temperature gradient. If the velocity vector is not aligned with the gradient of the solution, oscillation may occur in the transverse direction and the SUPG method which only adds diffusion in the velocity, or streamline, direction will fail. Extra diffusion has to be added in the transverse direction in order to stabilize the solution. This is traditionally taken care of by the so-called "shock capturing" or "discontinuity-capturing" schemes [9], which become non-linear due to the dependence of the gradient of the solution.

Figure 2.5 shows the inability of the SUPG method to capture sharp gradients not aligned with the velocity direction.

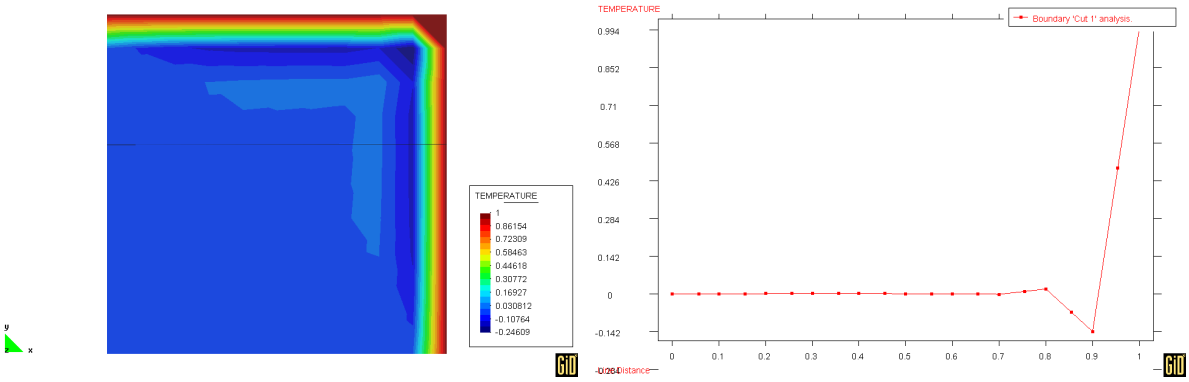

Figure 2.5: The diagonal velocity $u = \frac{3}{\sqrt{2}}[1, 1]$ is not aligned with the sharp gradient at the upper and right boundary, $l^e = 0.1$, $\gamma = 15$. SUPG results. Left: temperature distribution. Right: horisontal cut

2.2.3 Finite Calculus

Writing the Finite Calculus (FIC) formulation of the problem in 2D

$$u_j \frac{\partial T}{\partial x_j} - k\frac{\partial^2 T}{\partial x_j^2} - Q - \frac{h_i}{2}\frac{\partial}{\partial x_i}\left(u_j \frac{\partial T}{\partial x_j} - k\frac{\partial^2 T}{\partial x_j^2} - Q\right) = 0 \quad in\ \Omega$$
$$T = \overline{T} \quad on\ \partial\Omega \tag{2.21}$$

Once again excluding terms that are zero due to the linear interpolation the discretized weak form is set up as following. Find $T_h \epsilon S_h$ such that

$$\int_\Omega \left(w_h u_j \frac{\partial T_h}{\partial x_j} + k\frac{\partial w_h}{\partial x_j}\frac{\partial T_h}{\partial x_j}\right)\, d\Omega + \Sigma_e \int_{\Omega^e} \frac{h_k}{2}\frac{\partial w_h}{\partial x_k} \cdot u_j \frac{\partial T_h}{\partial x_j}\, d\Omega =$$
$$\int_\Omega w_h Q\, d\Omega + \Sigma_e \int_{\Omega^e} \frac{h_k}{2}\frac{\partial w_h}{\partial x_k} \cdot Q\, d\Omega \qquad in\ \Omega$$
$$T_h = \overline{T} \qquad on\ \partial\Omega \tag{2.22}$$

for all $w_h \epsilon V_h$

If h_i is taken in the velocity direction as

$$h_i = \alpha \cdot l^e \frac{u_i}{|u|} \qquad \text{where} \quad \alpha = \coth\gamma - \frac{1}{\gamma}$$

the SUPG scheme is recovered. It is however convenient to split h_i into a streamline and a transverse characteristic length vector. In [8] these are derived via a non-linear iterative scheme.

In [7] a slightly different and more consistent method is proposed. Instead of splitting the characteristic length vector in a streamline and transverse part the FIC balance equation is expressed in the principle curvature directions of the solution. For linear elements the principle curvature is approximated as the gradient. Based on these directions, a transformed coordinate system is defined with ξ_i as basis. Denoting vector quantities with a prime the FIC formulation of the problem in the ξ_i-system is written as

$$u'_j \frac{\partial T}{\partial \xi_j} - k\frac{\partial^2 T}{\partial \xi_j^2} - Q - \frac{h'_i}{2}\frac{\partial}{\partial \xi_i}\left(u'_j \frac{\partial T}{\partial \xi_j} - k\frac{\partial^2 T}{\partial \xi_j^2} - Q\right) = 0 \qquad in\ \Omega$$
$$T = \overline{T} \qquad in\ \Omega \tag{2.23}$$

This equation contains the necessary additional diffusion to stabilize the solution in all situations. The next step is to transform the equation to the original basis. A piece-wise linear finite element approximation is carried out and the discretized weak form of the problem is expressed as follows.

For all $w_h \epsilon V_h$ find $T_h \epsilon S_h$ such that

$$\int_\Omega \left(w_h u_j \frac{\partial T_h}{\partial x_j} + k \frac{\partial w_h}{\partial x_j} \frac{\partial T_h}{\partial x_j} \right) \, d\Omega + \Sigma_e \int_{\Omega^e} \frac{\partial w_h}{\partial x_j} R_{ij} \bar{D}'_{il} R_{lk} \frac{\partial T_h}{\partial x_k} \, d\Omega =$$
$$\int_\Omega w_h Q \, d\Omega + \Sigma_e \int_{\Omega^e} R_{ij} \frac{h'_i}{2} \frac{\partial w_h}{\partial x_j} \cdot Q \, d\Omega \qquad in \ \Omega$$
$$T_h = \overline{T} \qquad on \ \partial\Omega \qquad (2.24)$$

The additional diffusion matrix is defined as

$$\bar{D}'_{ij} = \begin{bmatrix} \frac{u_\xi h_\xi}{2} & 0 \\ 0 & \frac{u_\eta h_\eta}{2} \end{bmatrix} \qquad (2.25)$$

where the subindices ξ and η refer to the respective component of the ξ_i-system in 2D. The characteristic length distances h_ξ and h_η are evaluated according to

$$h_\xi = \alpha_\xi \cdot l_\xi$$
$$h_\eta = \alpha_\eta \cdot l_\eta$$

where the values of the stabilization parameters α_ξ and α_η are computed by considering the solution of two uncoupled 1D problems along the ξ and the η directions.

$$\text{If} \quad (u_\xi \neq 0) \qquad \alpha_\xi = \coth\gamma_\xi - \frac{1}{\gamma_\xi} \qquad , \qquad \gamma_\xi = \frac{u_\xi l_\xi}{2k}$$
$$\text{Else} \qquad \alpha_\xi = 0$$

$$\text{If} \quad (u_\eta \neq 0) \qquad \alpha_\eta = \coth\gamma_\eta - \frac{1}{\gamma_\eta} \qquad , \qquad \gamma_\eta = \frac{u_\eta l_\eta}{2k}$$
$$\text{Else} \qquad \alpha_\eta = 0$$

Note that the Peclet numbers γ_ξ and γ_η can take negative values as they depend on the respective velocity component and not, as in the SUPG method, the absolute value of the velocity. The lengths l_ξ and l_η are the maximum projections of u_ξ and u_η along the element sides.

The (ξ, η) coordinate system forms the angle θ to the original basis, see Figure 2.6. The transformation matrix R_{ij} is defined according to

$$R_{ij} = \begin{bmatrix} \cos\theta & \sin\theta \\ -\sin\theta & \cos\theta \end{bmatrix}$$

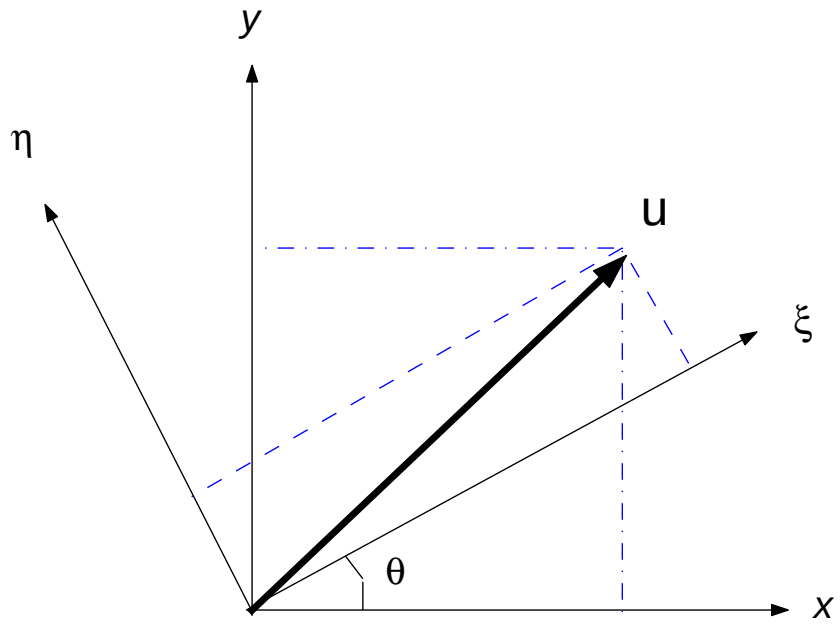

Figure 2.6: Transformed coordinate system

The solution to (2.24) is obtained by setting up a fictitious transient problem using a forward Euler scheme with small time steps and bringing it to steady state. This allows to treat easily the nonlinearity arising from the dependence of the temperature gradient. Furthermore, using a lumped mass matrix, a diagonal solver can be adapted which reduces the computational cost.

In Figure 2.7 it is shown that the FIC method provides a well-stabilized result for the example with diagonal velocity in contrast with the SUPG method.

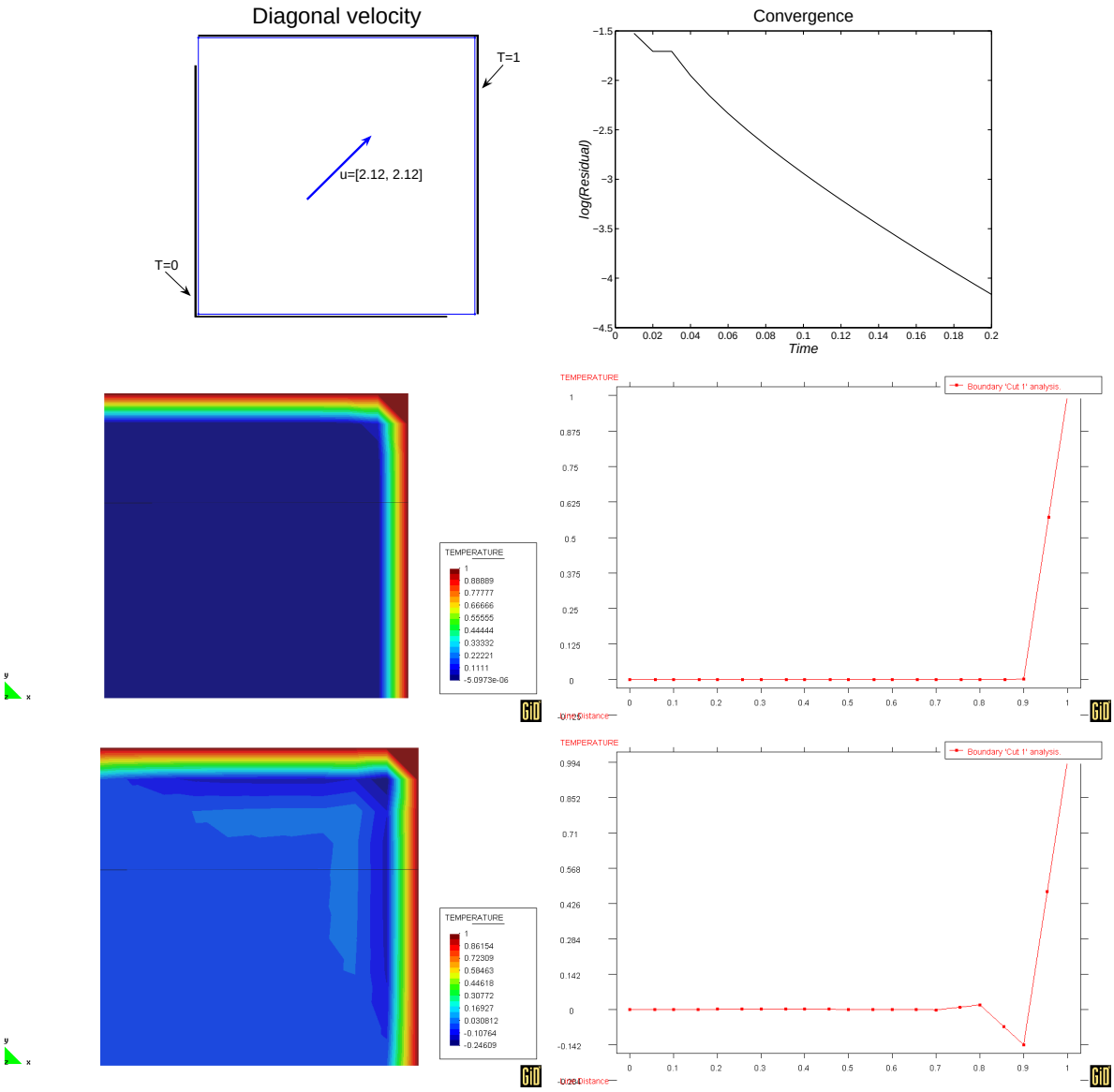

Figure 2.7: Diagonal velocity $u = \frac{3}{\sqrt{2}}[1,1]$, $l^e = 0.1$, $\gamma = 15$ FIC solution using a forward euler scheme ($\theta = 0$) with $\Delta t = 0.01$. Above to the right the residual is plotted versus time. In the middle temperature distribution is plotted and horizontal cut. Below SUPG solution.

In Figure 2.8 an example with non-uniform conditions causing a sharp internal temperature gradient perpendicular to the velocity direction is shown.

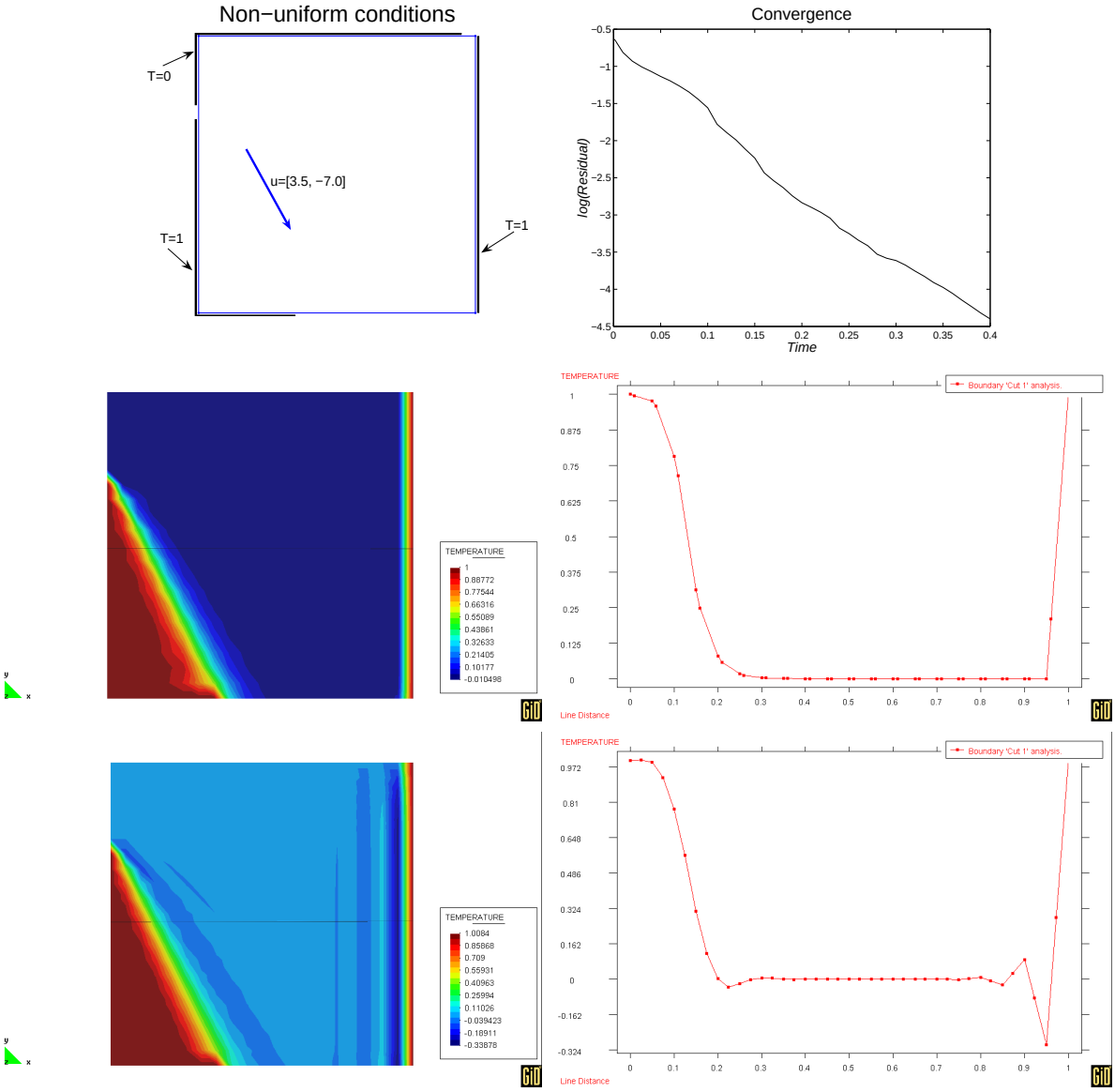

Figure 2.8: $u = [3.5, -7.0]$, $l^e = 0.05$, $\gamma = 20$, FIC solution ($\theta = 0$), $\Delta t = 0.001$. Below SUPG solution.

In Figure 2.9 the velocity is rotational varying from 0 to $\sqrt{2}$, Dirichlet conditions are set on the left and upper edge so that a sharp internal gradient occurs perpendicular to the velocity. Whereas the SUPG-method fails to capture the oscillations the FIC-method provides a well stabilized result.

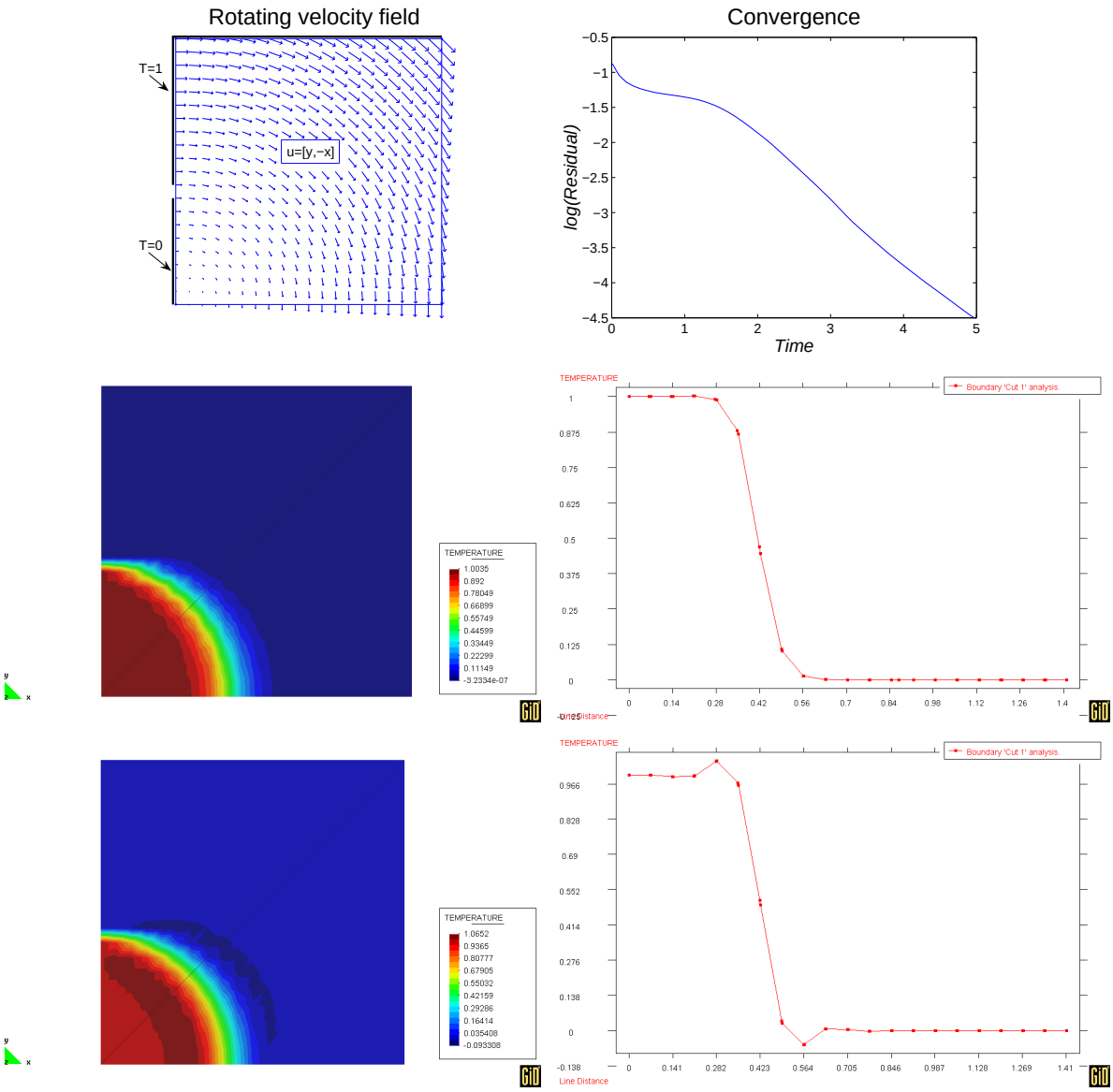

Figure 2.9: Rotational velocity $u = [-y, x]$, $l^e = 0.05$, $\gamma = 125$. FIC results ($\theta = 0$), $\Delta t = 0.01$. Below SUPG results.

2.3 One-dimensional quadratic formulation

Introducing Lagrangian quadratic elements in 1D, the shape functions in local coordinates ξ are written as

$$\begin{aligned} N_1 &= \frac{1}{2}\xi\,(\xi - 1) \\ N_2 &= 1 - \xi^2 \\ N_3 &= \frac{1}{2}\xi\,(\xi + 1) \end{aligned} \tag{2.26}$$

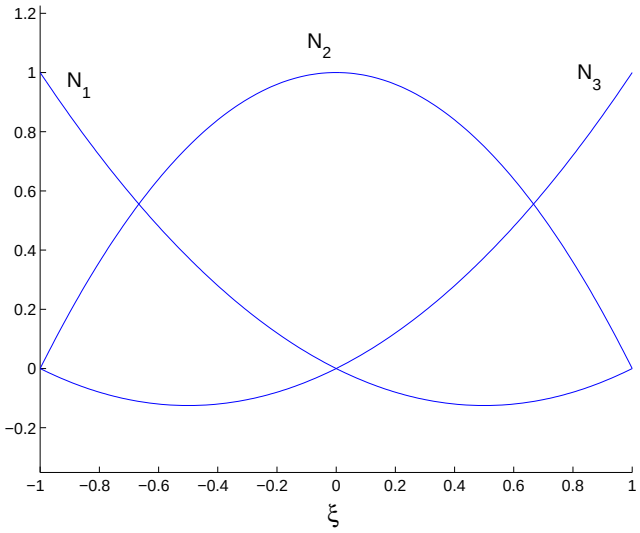

Figure 2.10: Lagrangian quadratic shape functions

2.3.1 Unstabilized scheme

Starting from the weak form of the convection-diffusion equation as formulated in Section 2.1, see Equation (2.3), the finite element approximation is carried out now using the quadratic shape functions (2.26). The discretized weak form is stated as follows.

Find $T_h \epsilon S_h$ such that

$$\begin{aligned} \int_\Omega \left(w_h u \frac{dT_h}{dx} + k \frac{dw_h}{dx}\frac{dT_h}{dx} \right) d\Omega &= \int_\Omega w_h Q \; d\Omega \qquad in\ \Omega \\ T_h &= \overline{T} \qquad on\ \partial\Omega \end{aligned} \tag{2.27}$$

for all $w_h \epsilon V_h$ where

$$\begin{aligned} S_h &= [v \epsilon H^1(\Omega) | v \epsilon P^2(\Omega^e) | v = \overline{T}\ on\ \partial\Omega] \\ V_h &= [v \epsilon H_0^1(\Omega) | v \epsilon P^2(\Omega^e)] \end{aligned} \tag{2.28}$$

2.3.2 Petrov-Galerkin method

The perturbation of the test functions w that stands for the upwinding effect is formulated as

$$w = w + \frac{\alpha l^e}{2}\frac{dw}{dx}$$

for the two end nodes and

$$w = w + \frac{\beta l^e}{2}\frac{dw}{dx}$$

for the midnode. The expressions for the optimal upwind functions α and β providing nodally exact solution yield [1]

$$\begin{aligned} \beta &= \frac{1}{2}\left(\coth\frac{\gamma}{2} - \frac{2}{\gamma}\right) \\ \alpha &= \frac{(3 + 3\gamma\beta + \gamma^2)\tanh\gamma - (3\gamma + \gamma^2\beta)}{(2 - 3\beta\tanh\gamma)\gamma^2} \end{aligned} \tag{2.29}$$

Abandoning the requirement of nodally exact values there is a possibility to substitute α and β by a unique upwind function α^1 according to

$$\alpha^1 = \frac{1}{2}\left(\coth\gamma - \frac{1}{\gamma}\right) \tag{2.30}$$

Using α^1 the discretized weak form of the Petrov-Galerkin scheme for solving the convection-diffusion equation using quadratic elements is set as finding $T_h \epsilon S_h$ such that

$$\begin{aligned} \int_\Omega \left(w_h u\frac{dT_h}{dx} + k\frac{dw_h}{dx}\frac{dT_h}{dx}\right)\, d\Omega + \sum_e \int_{\Omega^e} \frac{\alpha^1 l^e}{2}\frac{dw_h}{dx}\left(u\frac{dT_h}{dx} - k\frac{d^2T_h}{dx^2}\right)\, d\Omega = \\ \int_\Omega w_h Q\, d\Omega + \sum_e \int_{\Omega^e} \frac{\alpha^1 l^e}{2}\frac{dw_h}{dx} Q\, d\Omega \qquad in\ \Omega \\ T_h = \overline{T} \qquad on\ \partial\Omega \end{aligned} \tag{2.31}$$

for all $w_h \epsilon V_h$

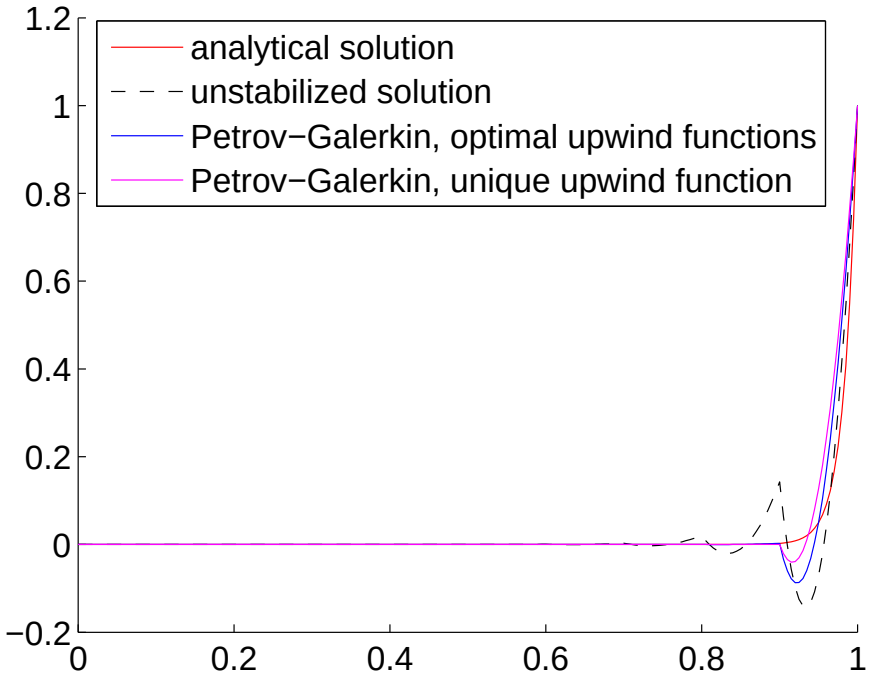

Figure 2.11: 1D quadratic elements, $l^e = 0.1$, Peclet number γ= 3. Petrov-Galerkin solution

2.3.3 Galerkin/Least-Squares method

The perturbation of the test functions w that stands for the upwinding effect is formulated as

$$w = w + \frac{\alpha l^e}{2}\frac{dw}{dx} - \frac{\alpha l^e k}{2u}\frac{d^2 w}{dx^2}$$

for the end nodes and

$$w = w + \frac{\beta l^e}{2}\frac{dw}{dx} - \frac{\beta l^e k}{2u}\frac{d^2 w}{dx^2}$$

for the midnode. The upwind functions are

$$\beta = \frac{\gamma^2\left(\coth\frac{\gamma}{2} - \frac{2}{\gamma}\right)}{6 - 3\gamma\coth\frac{\gamma}{2} + 2\gamma^2}$$
$$\alpha = \frac{(3 + \gamma^2 + 6\gamma\beta + 9\frac{\beta}{\gamma})\tanh\gamma - (3\gamma + 9\beta + \gamma^2\beta)}{(2\gamma^2 - 3\beta\gamma^2\tanh\gamma)} \tag{2.32}$$

The optimal choice for the corresponding unique upwind function is

$$\alpha^1 = \left(\frac{3}{2\gamma^2} + \frac{1}{2}\right)\left(\coth\gamma - \frac{1}{\gamma}\right) - \frac{1}{2\gamma}$$

(2.33)

and with this choice the discretized weak form of the GLS-stabilized scheme is written as follows.

Find $T_h \epsilon S_h$ such that

$$\begin{aligned} \int_\Omega \left(w_h u \frac{dT_h}{dx} + k \frac{dw_h}{dx} \frac{dT_h}{dx} \right) \, d\Omega + \\ \sum_e \int_{\Omega^e} \left(\frac{\alpha^1 l^e}{2} \frac{dw_h}{dx} - \frac{\alpha^1 l^e k}{2u} \frac{d^2 w_h}{dx^2} \right) \left(u \frac{dT_h}{dx} - k \frac{d^2 T_h}{dx^2} \right) \, d\Omega = \\ \int_\Omega w_h Q \, d\Omega + \sum_e \int_{\Omega^e} \left(\frac{\alpha^1 l^e}{2} \frac{dw_h}{dx} - \frac{\alpha^1 l^e k}{2u} \frac{d^2 w_h}{dx^2} \right) Q \, d\Omega \qquad in \ \Omega \\ T_h = \overline{T} \qquad on \ \partial\Omega \end{aligned} \tag{2.34}$$

for all $w_h \epsilon V_h$

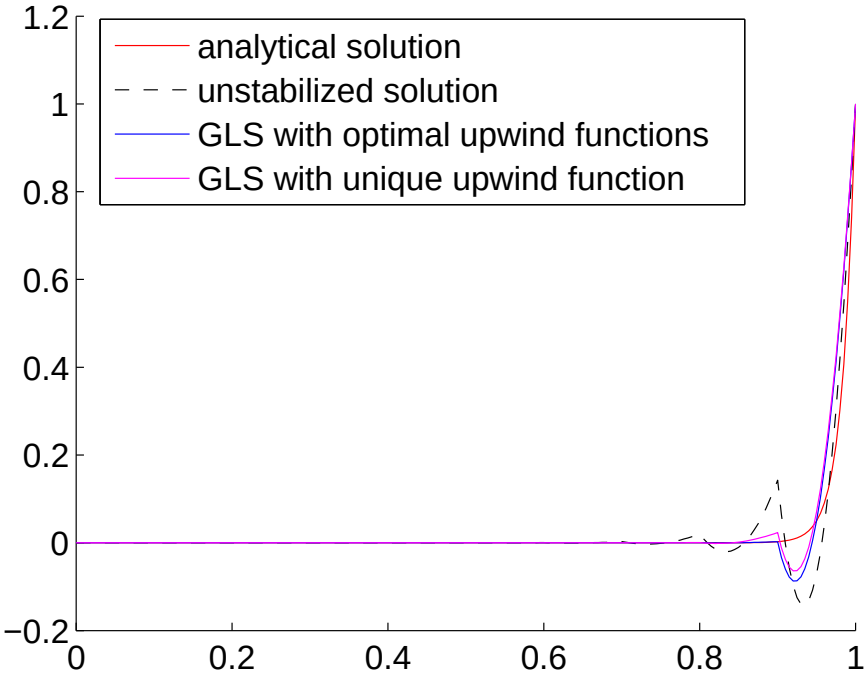

Figure 2.12: 1D quadratic elements, $l^e = 0.1$, $\gamma = 3$. GLS method

2.4 Two-dimensional quadratic formulation

The Lagrangian quadratic approximation is now introduced in 2D. The geometry is an iso-parametric triangle as shown in figure 2.13. The shape functions are specified according to

$$\begin{aligned} N_1 &= (1-2\xi-2\eta)(1-\xi-\eta) \\ N_2 &= \xi(2\xi-1) \\ N_3 &= \eta(2\eta-1) \\ N_4 &= 4\xi(1-\xi-\eta) \\ N_5 &= 4\xi\eta \\ N_6 &= 4\eta(1-\xi-\eta) \end{aligned}$$

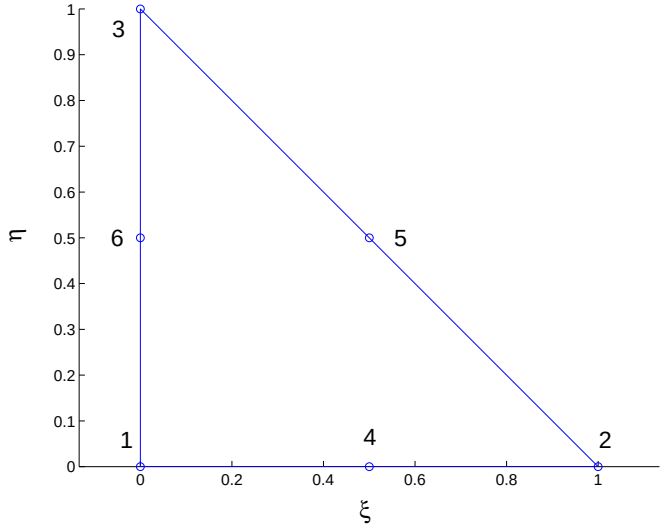

Figure 2.13: Iso-parametric triangular element with quadratic shape functions

2.4.1 Unstabilized scheme

The weak form from Equation (2.16) is approximated in the piece-wise quadratic finite element spaces

$$\begin{aligned} S_h &= [v \epsilon H^1(\Omega) | v \epsilon P^2(\Omega^e) | v = \overline{T} \ on \ \partial\Omega] \\ V_h &= [v \epsilon H_0^1(\Omega) | v \epsilon P^2(\Omega^e)] \end{aligned} \tag{2.35}$$

and the unstabilized discretized weak form is stated as follows.

For all $w_h \epsilon V_h$ find $T_h \epsilon S_h$ such that

$$\begin{aligned} \int_\Omega \left(w_h u_j \frac{\partial T_h}{\partial x_j} + k \frac{\partial w_h}{\partial x_j} \frac{\partial T_h}{\partial x_j} \right) \, d\Omega &= \int_\Omega w_h Q \, d\Omega \qquad in \ \Omega \\ T_h &= \overline{T} \qquad on \ \partial\Omega \end{aligned} \tag{2.36}$$

In the following example a quadratic analytic solution is used to check the implementation of the quadratic scheme. A unit square with constant velocity towards the right and Dirichlet condition $T = 0$ to the left and $T = 1$ to the right.

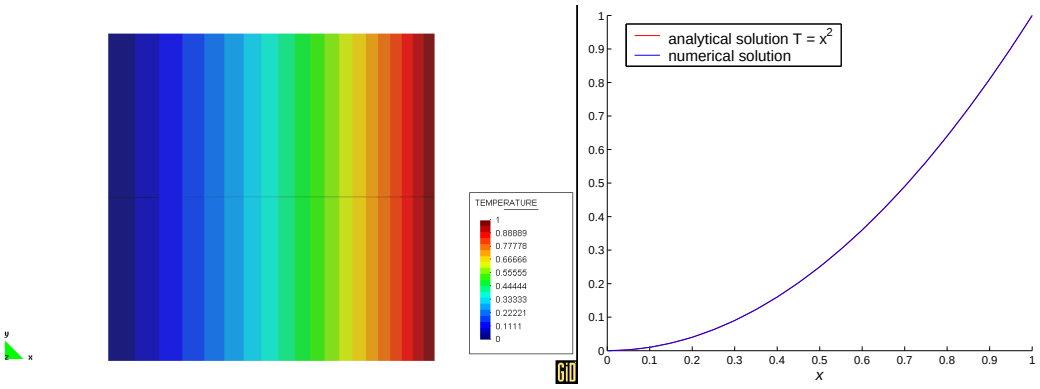

Figure 2.14: $u = [100, 0]$, $l^e = 0.1$, $k = 1$, $Q = 200 \cdot x - 2$

2.4.2 Galerkin/Least-Squares method

The modified test function w for the GLS method is written in 2D as

$$w = w + \tau u_j^e \frac{\partial w}{\partial x_j} - \tau^e k \frac{\partial^2 w}{\partial x_j^2}$$

The time parameter τ^e is taken as

$$\tau^e = \frac{\alpha^1 l^e}{2|u|}$$

where the optimal unique upwind function α^1 from the 1D case, see (2.33), is used. The discretized weak form of the problem in 2D is now set up. Find $T_h \epsilon S_h$ such that

$$\begin{aligned} \int_\Omega \left(w_h u_j \frac{\partial T_h}{\partial x_j} + k \frac{\partial w_h}{\partial x_j} \frac{\partial T_h}{\partial x_j} \right) \, d\Omega + \\ \sum_e \int_{\Omega^e} \tau^e \left(u_j \frac{\partial w_h}{\partial x_j} - k \frac{\partial^2 w_h}{\partial x_j^2} \right) \left(u_k \frac{\partial T_h}{\partial x_k} - k \frac{\partial^2 w_h}{\partial x_k^2} \right) \, d\Omega = \\ \int_\Omega w_h Q \, d\Omega + \sum_e \int_{\Omega^e} \tau^e \left(u_j \frac{\partial w_h}{\partial x_j} - k \frac{\partial^2 w_h}{\partial x_j^2} \right) Q \, d\Omega \qquad in \ \Omega \\ T_h = \overline{T} \qquad on \ \partial\Omega \end{aligned} \tag{2.37}$$

for all $w_h \epsilon V_h$

Figure 2.15 shows the example with a diagonal velocity creating a sharp boundary layer at the upper and the right edge.

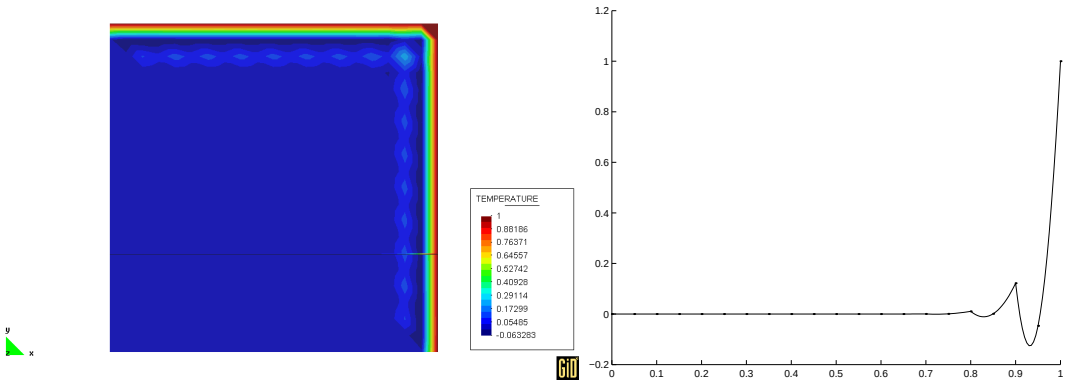

Figure 2.15: Diagonal velocity $u = \frac{3}{\sqrt{2}}[1,1]$, $l^e = 0.1$, $\gamma = 15$. GLS results. Temperature distribution and horizontal cut

2.4.3 Streamline Upwind Petrov Galerkin method

The modified test function w for the SUPG method is written as

$$w = w + \tau^e u_j \frac{\partial w}{\partial x_j}$$

Using the optimal unique upwind function α^1 from the 1D case, see (2.30), the discretized weak form consists in, for all $w_h \epsilon V_h$, finding $T_h \epsilon S_h$ such that

$$\int_\Omega \left(w_h u_j \frac{\partial T_h}{\partial x_j} + k \frac{\partial w_h}{\partial x_j} \frac{\partial T_h}{\partial x_j} \right) d\Omega + \sum_e \int_{\Omega^e} \tau^e u_j \frac{\partial w_h}{\partial x_j} \left(u_k \frac{\partial T_h}{\partial x_k} - k \frac{\partial^2 w_h}{\partial x_k^2} \right) d\Omega =$$
$$\int_\Omega w_h Q \, d\Omega + \sum_e \int_{\Omega^e} \tau^e u_j \frac{\partial w_h}{\partial x_j} Q \, d\Omega \qquad in \ \Omega$$
$$T_h = \overline{T} \qquad on \ \partial\Omega \tag{2.38}$$

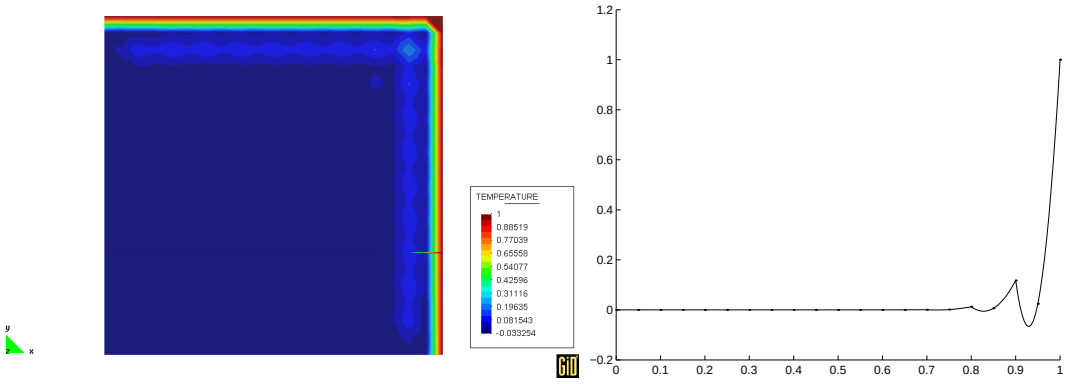

Figure 2.16: Diagonal velocity $u = \frac{3}{\sqrt{2}}[1,1]$, $l^e = 0.1$, $\gamma = 15$. SUPG results. Temperature distribution and horizontal cut

2.4.4 Finite Calculus

In this section the FIC equation is introduced in the principle curvature directions [7]. Using a quadratic interpolation a new term appears in the finite element formulation as the second derivative of the discretized variable has to be taken into account. The FIC equation is written as

$$u'_j\frac{\partial T}{\partial \xi_j} - k\frac{\partial^2 T}{\partial \xi_j^2} - Q - \frac{h'_i}{2}\frac{\partial}{\partial \xi_i}\left(u'_j\frac{\partial T}{\partial \xi_j} - k\frac{\partial^2 T}{\partial \xi_j^2} - Q\right) = 0 \qquad in\ \Omega \tag{2.39}$$

or in matrix format

$$\mathbf{u}'\cdot\nabla'^T T - k\nabla'\cdot\nabla'^T T - \nabla'\mathbf{D}'_{add}\cdot\nabla'^T T + \nabla'\mathbf{E}'\cdot(\nabla^2)'^T T = Q - \nabla'\mathbf{F}'\cdot Q \qquad in\ \Omega \tag{2.40}$$

the prime denoting that the principle curvature ξ is taken as basis. The velocity $\mathbf{u}' = [u_\xi\ u_\eta]$, the operators $\nabla' = \left[\frac{\partial}{\partial\xi}\ \frac{\partial}{\partial\eta}\right]$ and $(\nabla^2)' = \left[\frac{\partial^2}{\partial\xi^2}\ \frac{\partial^2}{\partial\eta^2}\right]$ and the following matrices

$$\mathbf{D}'_{add} = \begin{bmatrix} \frac{u_\xi h_\xi}{2} & 0 \\ 0 & \frac{u_\eta h_\eta}{2} \end{bmatrix}$$

$$\mathbf{E}' = \begin{bmatrix} \frac{h_\xi}{2}k & 0 \\ 0 & \frac{h_\eta}{2}k \end{bmatrix}$$

$$\mathbf{F}' = \begin{bmatrix} \frac{h_\xi}{2} \\ \frac{h_\eta}{2} \end{bmatrix}$$

are defined in the (ξ,η)-system. The definition of the characteristic length vector $\mathbf{h}' = [h_\xi\ h_\eta]$ is

$$h_\xi = \alpha^1_\xi \cdot l_\xi$$
$$h_\eta = \alpha^1_\eta \cdot l_\eta$$

where $\alpha^1 = \frac{1}{2}\left(\coth\gamma - \frac{1}{\gamma}\right)$ is the optimal unique upwind function for quadratic elements using the SUPG method [1]. Note that the Peclét number in this case is component-wise evaluated taking into account each of u_ξ and u_η.

The matrices $\mathbf{D}'_{add}$, $\mathbf{E}'$ and $\mathbf{F}'$ are now brought back to the original basis (x,y) by the following operations

$$\mathbf{D}_{add} = \mathbf{R}^T\mathbf{D}'_{add}\mathbf{R}$$
$$\mathbf{E} = \mathbf{R}^T\mathbf{E}'\mathbf{R}$$
$$\mathbf{F} = \mathbf{R}^T\mathbf{F}'$$

using the transformation matrix $\mathbf{R}$ defined as

$$\mathbf{R} = \begin{bmatrix} \cos\theta & \sin\theta \\ -\sin\theta & \cos\theta \end{bmatrix}$$

where θ is the angle of the transformed system (ξ,η) in the original basis (x,y) according to figure 2.17.

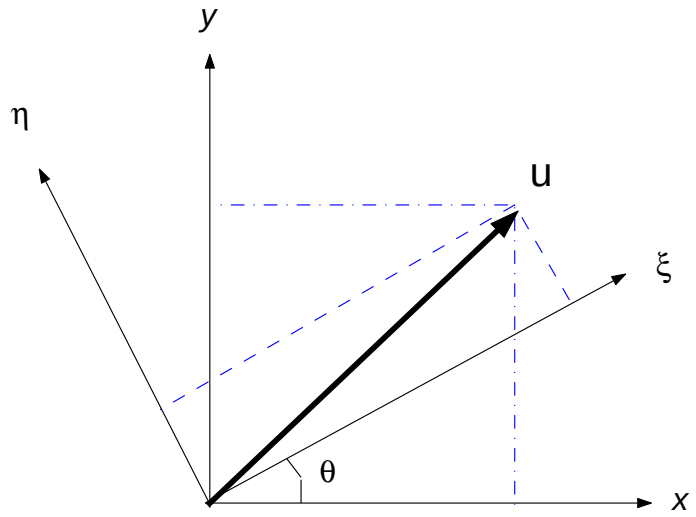

Figure 2.17: Transformed coordinate system

In order to determine ξ the second order derivatives of the temperature are evaluated and the eigenvalue problem is solved for the curvature matrix.

$$\mathbf{C} = \begin{bmatrix} \frac{\partial^2 T}{\partial x^2} & \frac{\partial^2 T}{\partial x \partial y} \\ \frac{\partial^2 T}{\partial x \partial y} & \frac{\partial^2 T}{\partial y^2} \end{bmatrix} \tag{2.41}$$

As the principle curvature direction ξ is chosen the eigenvector that has the corresponding eigenvalue of largest magnitude. η is then orthogonal to ξ in an anticlockwise sense.

The FIC equation is now written in the (x, y)-coordinates as

$$\mathbf{u} \cdot \nabla^T T - k \nabla \cdot \nabla^T T - \nabla \mathbf{D}_{add} \cdot \nabla^T T + \nabla \mathbf{E} \cdot (\nabla^2)^T T = Q - \nabla \mathbf{F} \cdot Q \qquad in\ \Omega \tag{2.42}$$

and the usual galerkin procedure is carried out. The weak form is constituted as follows. For all $w \epsilon V$ find $T \epsilon S$ such that

$$\begin{aligned} \int_\Omega \left(w\mathbf{u} \cdot \nabla^T T + k \nabla w \cdot \nabla^T T + \nabla w \mathbf{D}_{add} \cdot \nabla^T T - \nabla w \mathbf{E} \cdot (\nabla^2)^T T \right) \, d\Omega = \\ \int_\Omega (w + \nabla w \mathbf{F}) \cdot Q \, d\Omega \qquad in\ \Omega \\ T = \overline{T} \qquad on\ \partial\Omega \end{aligned} \tag{2.43}$$

for all $w \epsilon V$. Using piece-wise quadratic finite elements the discretized weak form consists in, for all $w_h \epsilon V_h$, finding $T_h \epsilon S_h$ such that

$$\begin{aligned} \int_{\Omega^e} \left(w_h \mathbf{u} \cdot \nabla^T T_h + k \nabla w_h \cdot \nabla^T T_h + \nabla w_h \mathbf{D}_{add} \cdot \nabla^T T_h - \nabla w_h \mathbf{E} \cdot (\nabla^2)^T T_h \right) \, d\Omega = \\ \int_{\Omega^e} (w_h + \nabla w_h \mathbf{F}) \cdot Q \, d\Omega \qquad in\ \Omega \\ T = \overline{T} \qquad on\ \partial\Omega \end{aligned} \tag{2.44}$$

The nonlinearity arising from the dependence of the second order derivative of the temperature is dealt with by solving a fictitious transient problem using an explicit forward Euler scheme which is brought to steady-state using small time steps.

In figure 2.18 the results using FIC for the example with diagonal velocity is shown. Using the cubic term $\nabla' \mathbf{E}' \cdot (\nabla^2)'^T T$ and the principle curvature direction the solution does not converge. However, excluding the cubic term and using the gradient direction, convergence is obtained.

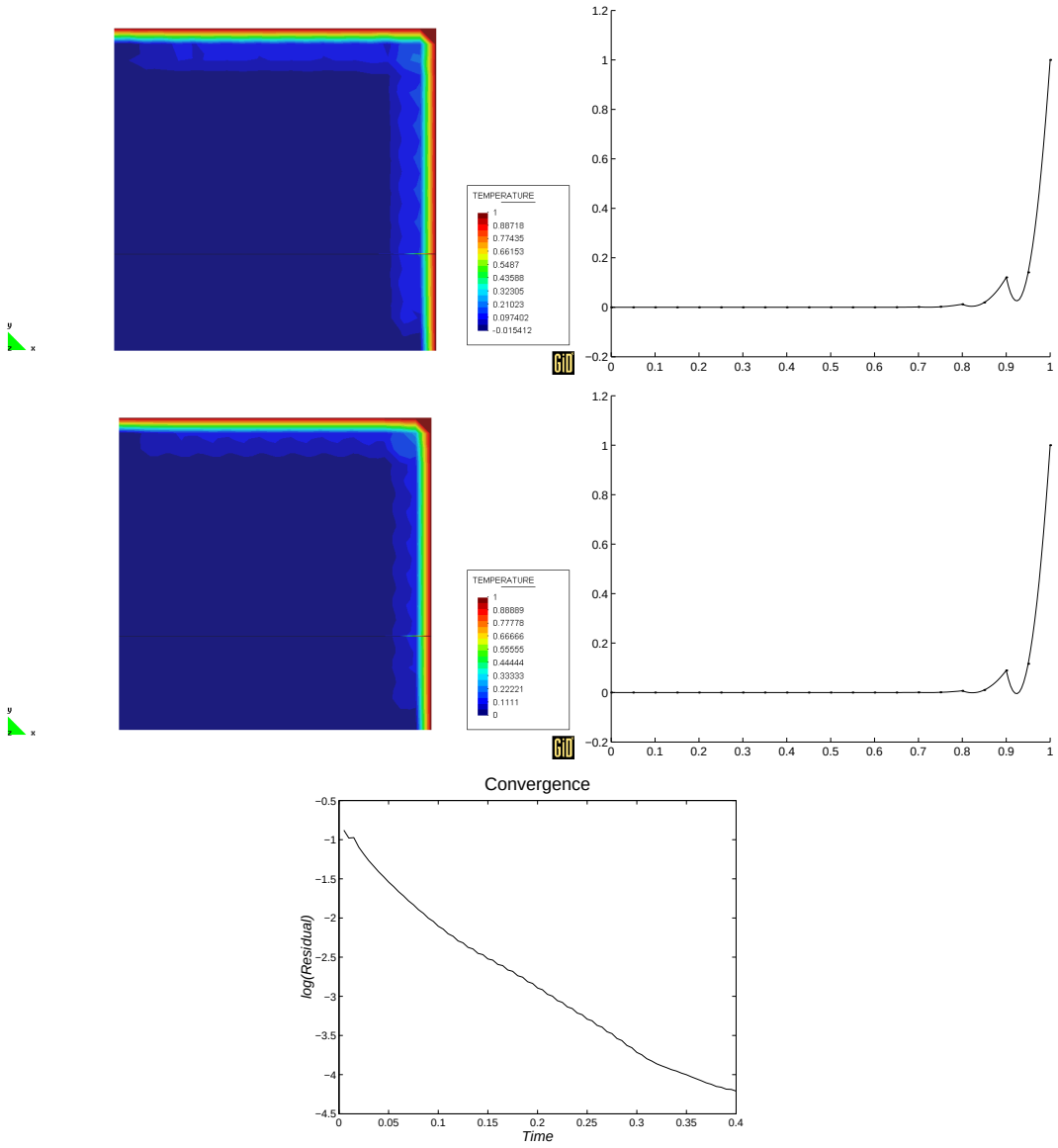

Figure 2.18: Diagonal velocity $u = 3/\sqrt{2}[1, 1]$, quadratically interpolated elements $l^e = 0.1$, $\gamma = 15$, $\Delta t = 0.005$, $\theta = 0$. Above: FIC in principle curvature direction. Below: without the cubic term and FIC in gradient direction

2.4.5 Concluding remarks

Below the result from simulations using the quadratic FIC formulation are compared with the GLS and SUPG methods for the two examples with non-uniform conditions and rotational velocity. In both cases the FIC equations are implemented in the principle curvature direction and the cubic term is taken into account. In Figure 2.19 the temperature distribution is visualized for the example with non-uniform conditions. The spurious oscillations that occur when the GLS and SUPG schemes are used are absent, but the scheme is more diffusive than the linear results in Figure 2.8. Moreover the sharp boundary layer at the right boundary can not be captured so well by quadratic elements.

In Figure 2.20 the internal boundary layer that appears due to the rotating velocity field is well captured by the quadratic elements, which also is the case for the linear elements in Figure 2.9.

From the above results it can be concluded that the FIC formulation expressed in the principle curvature directions of the solution can be used to solve convection-diffusion problems using linear as well as quadratic elements. In general terms, however, linear elements are more suitable, besides from being computationally cheaper.

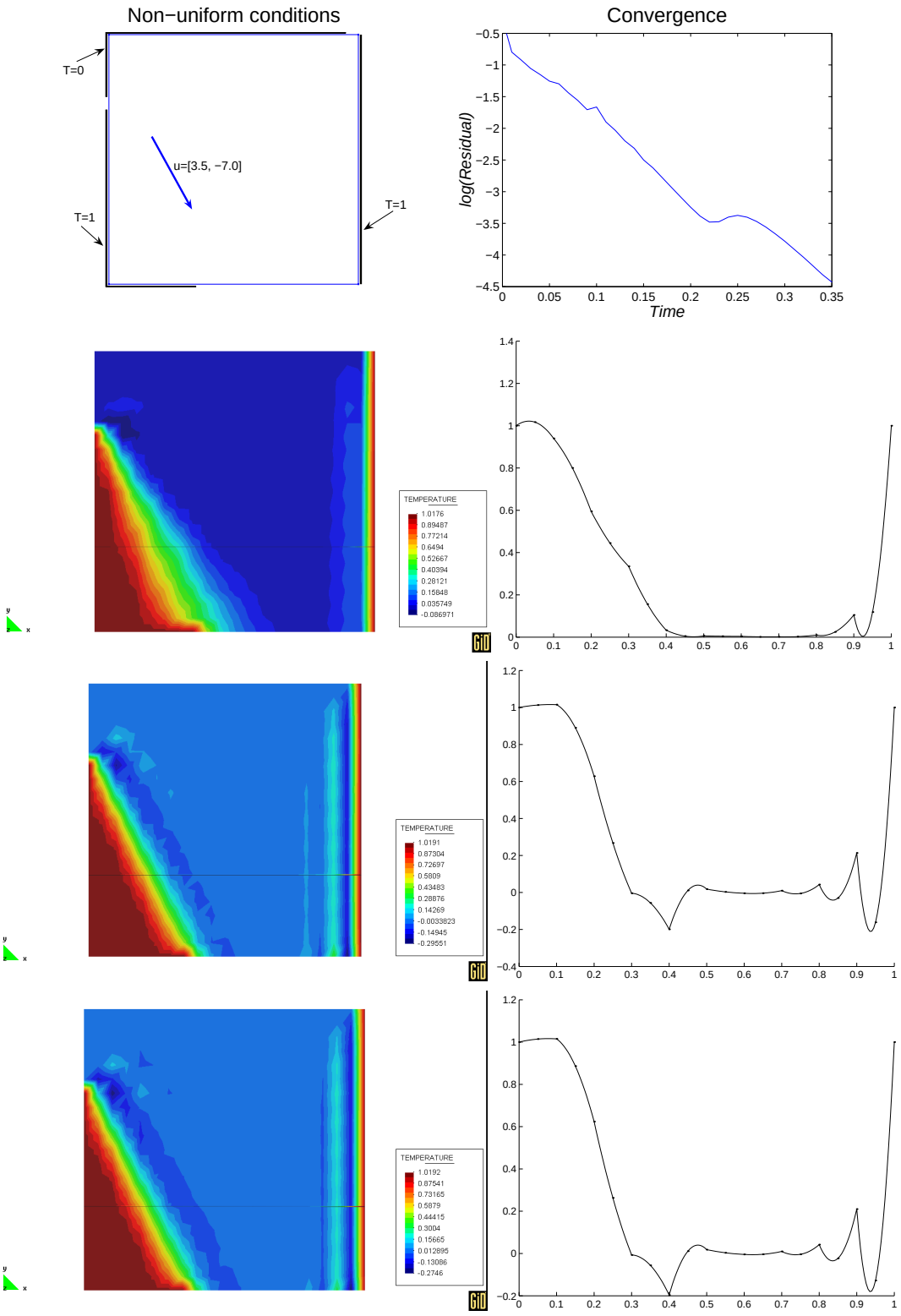

Figure 2.19: $u = [3.5, -7.0]$, quadratically interpolated elements $l^e = 0.1$, $\gamma = 39$, $\Delta t = 0.001$, $\theta = 0$. Above: FIC. In the middle: GLS results. Below: SUPG results.

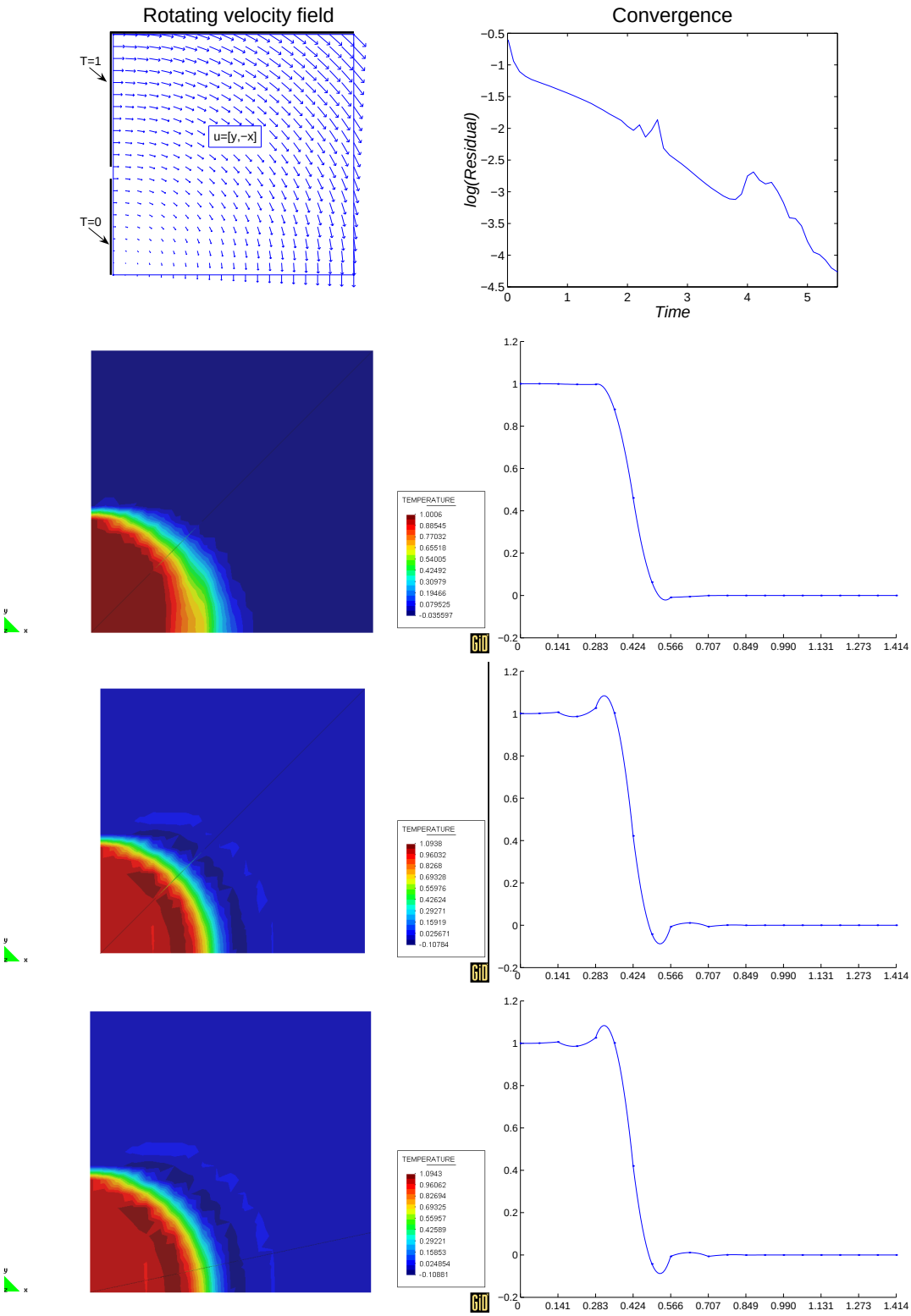

Figure 2.20: Rotational velocity $u = [y, -x]$, quadratically interpolated elements $l^e = 0.1$, $\gamma = 250$, $\Delta t = 0.01$, $\theta = 0$. Above: FIC. In the middle: GLS results. Below: SUPG results.

Chapter 3

Navier-Stokes equations

In this chapter the incompressible Navier-Stokes equations and numerical methods for solving them using linear as well as quadratic finite elements are presented. Equal order velocity-pressure interpolation is employed.

First the Galerkin/Least-Squares (GLS) method is implemented and solved using a monolithic strategy. The transient Navier-Stokes equations are then written in an arbitrary Lagrangian-Eulerian (ALE) form and a mesh moving strategy is set up. Then the Finite Calculus (FIC) approach in the principle curvature direction is implemented in 2D and 3D and solved using a fractional step method. The formulation is first tested by performing standard flow simulations at low and high Reynolds numbers. Next a simulation is carried out in a control volume surrounding a large telescope building. The so-called EURO50 [45] is a joint European project in charge of planning for the construction of the world´s so far largest optics telescope. Its size combined with the precise optics needed for astronomic observations sets high requirements on the mechanical design and analysis tools such as a fluid-structure interaction (FSI) model of the telescope might be feasible. This is not done in this monograph, however critical issues that come from the wind effect are discussed and the results from the aerodynamic simulation reproduce the flow pattern inside and outside the telescope building.

3.1 Stabilized Incompressible flow

The incompressible Navier-Stokes equations are governed by instability problems of different character. One is the underestimation of the diffusion term, as introduced in Chapter 2. Another source of instability lies within the fact that, even though the pressure is a dependent variable in the whole system of equations, it is uncoupled from the incompressibility condition, as expressed in Equation (3.1b) which governs the conservation of mass. The consequence of this is that the final system to be solved might be not positive definite, leading to oscillations in the pressure field. The requirements for the velocity and pressure spaces in order to avoid this instability is that they accomplish the so-called Ladyzhenskaya/Babuska/Brezzi (LBB) condition.

Equal order velocity and pressure interpolations, which are used here, do not

accomplish the LBB condition. However stabilizing methods like the GLS method, the related method of subgrid-scales (SGS) [12] as well as the Finite Calculus (FIC) method [19],[25] are able to circumvent the LBB condition and thus allow the use of equal order interpolation. Additionally all these methods induce the necessary additional diffusion to compensate for the instabilities due to a dominant convection term.

In this first section the incompressible Navier-Stokes equations are solved using a monolithic scheme and they are stabilized by means of the GLS method. After establishing the strong form of the equations with boundary conditions the weak form is derived. The GLS method is applied to the weak form and the arising terms provide stabilization for the convection term as well as for the incompressibility constraint. This allows to use an equal order interpolation for the velocity and the pressure fields. The formulation is tested using linear as well as quadratic elements by setting up divergence free velocity fields for which analytic solutions exist. Also the stationary solution for a cavity flow is presented.

The GLS-formulation is then extended to the transient case and tried out for a problem of flow around a cylinder.

3.1.1 Strong form

The incompressible Navier-Stokes equations consist in a) the equations governing the conservation of momentum and b) the equation for conservation of mass, which because of the incompressibility constraint reduces to conservation of volume. Sometimes b) is called the divergence or incompressibility equation. The equations together with the c) Neumann and d) Dirichlet boundary conditions are

$$\begin{aligned} \rho u_j \frac{\partial u_i}{\partial x_j} - \frac{\partial s_{ij}}{\partial x_j} + \frac{\partial p}{\partial x_i} - f_i = 0 \qquad & in\ \Omega \qquad a) \\ \frac{\partial u_j}{\partial x_j} = 0 \qquad & in\ \Omega \qquad b) \\ n_j \left(s_{ij} - p\delta_{ij}\right) - \bar{t}_i = 0 \qquad & on\ \Gamma_N \qquad c) \\ u_i = \overline{u}_i \qquad & on\ \Gamma_D \qquad d) \end{aligned} \tag{3.1}$$

The deviatoric stress tensor is written as $s_{ij} = 2\mu e_{ij}$ where μ is the viscostiy and the deviatoric strain tensor $e_{ij} = \frac{1}{2}\left(\frac{\partial u_i}{\partial x_j} + \frac{\partial u_j}{\partial x_i}\right) - \frac{1}{3}\frac{\partial u_k}{\partial x_k}\delta_{ij}$.

Using the fact that for a divergence free velocity field the following relation holds

$$\frac{\partial s_{ij}}{\partial x_j} = \frac{\partial}{\partial x_j}\left(2\mu e_{ij}\right) = \mu\left(\frac{\partial^2 u_i}{\partial x_j^2} + \frac{\partial}{\partial x_i}\left(\frac{\partial u_j}{\partial x_j} - \frac{2}{3}\frac{\partial u_k}{\partial x_k}\right)\right) = \mu\frac{\partial^2 u_i}{\partial x_j^2} \tag{3.2}$$

the momentum equation (3.1a) can be rewritten in a Laplacian form according to

$$\rho u_j \frac{\partial u_i}{\partial x_j} - \mu\frac{\partial^2 u_i}{\partial x_j^2} + \frac{\partial p}{\partial x_i} - f_i = 0 \qquad in\ \Omega \tag{3.3}$$

The Neumann boundary conditions (3.1c) are now

$$n_j \left(\mu \frac{\partial u_i}{\partial x_j} - p\delta_{ij} \right) - \bar{t}_i = 0 \qquad on\ \Gamma_N \tag{3.4}$$

which are consistent with the approximation (3.3) for internal flows, excluding free surface effects.

3.1.2 Weak form

Test functions w_i for the momentum equations and q for the incompressibility equation are introduced, integration by parts is performed and using the Green-Gauss theorem the Neumann boundary condition is introduced. Together with the Dirichlet boundary condition the weak form of the problem is stated as follows.

Find $(u_i,\ p)\ \epsilon\ (\boldsymbol{S},\ \boldsymbol{Q})$ such that

$$\begin{aligned} \int_\Omega \left(w_i \rho u_j \frac{\partial u_i}{\partial x_j} + \frac{\partial w_i}{\partial x_j} \mu \frac{\partial u_i}{\partial x_j} - \frac{\partial w_i}{\partial x_i} p - w_i f_i \right)\ d\Omega - \\ \oint_{\Gamma_N} w_i \bar{t}_i\ d\Gamma + \int_\Omega q \frac{\partial u_j}{\partial x_j}\ d\Omega = 0 \qquad in\ \Omega \\ u_i = \overline{u}_i \qquad on\ \Gamma_D \end{aligned} \tag{3.5}$$

for all $(w_i,\ q)\ \epsilon\ (\boldsymbol{V},\ \boldsymbol{Q})$ where

$$\begin{aligned} \boldsymbol{V} &= \{ v\ \epsilon\ H_0^1(\Omega)\ |\ v = 0\ on\ \Gamma_D \} \\ \boldsymbol{S} &= \{ u\ \epsilon\ H^1(\Omega)\ |\ u = \overline{u}\ on\ \Gamma_D \} \\ \boldsymbol{Q} &= L_2(\Omega) \end{aligned}$$

3.1.3 GLS formulation

In the GLS method the differential operators of the original equation act on the test functions and are multiplied by a stabilization parameter and to the residual of the differential equation. As already pointed out in Chapter 2 the GLS method is consistent in the sense that if the exact solution of the original differential equation (3.1) is inserted in the GLS formulation a zero residual is obtained. Furthermore the amount of stabilization induced also depends on the meshsize and vanishes as the meshsize goes to zero.

First of all a division of the domain Ω into triangular subdomains Ω^e is made. The finite element functional spaces for the variables are introduced in (3.6) using piecewise polynomial functions of order n ($n = 1$ or 2 as linear and quadratic interpolation are used in this section). Furthermore, the non-linear convection term is linearized introducing the advective velocity $a_j^h = u_j^h$ evaluated at the previous

iteration according to the Picard´s method.

$$\begin{aligned} \boldsymbol{V}^h &= \{v \in H_0^1(\Omega) \ | v \in P^n(\Omega^e)| \ v = 0 \ on \ \Gamma_D\} \ \subset \ \boldsymbol{V} \\ \boldsymbol{S}^h &= \{u \in H^1(\Omega) \ | u \in P^n(\Omega^e)| \ u = \overline{u} \ on \ \Gamma_D\} \ \subset \ \boldsymbol{S} \\ \boldsymbol{Q}^h &= \{q \in L_2(\Omega) \ | q \in P^n(\Omega^e)\} \ \subset \ \boldsymbol{Q} \end{aligned} \tag{3.6}$$

With the following definitions:

$$\begin{aligned} \mathcal{L}(u_i^h) &= \rho a_j^h \frac{\partial u_i^h}{\partial x_j} - \mu \frac{\partial^2 u_i^h}{\partial x_j^2} + \frac{\partial p^h}{\partial x_i} \\ \mathcal{L}(w_i^h) &= \rho a_j^h \frac{\partial w_i^h}{\partial x_j} - \mu \frac{\partial^2 w_i^h}{\partial x_j^2} + \frac{\partial q^h}{\partial x_i} \\ \mathcal{L}(p^h) &= \frac{\partial u_j^h}{\partial x_j} \\ \mathcal{L}(q^h) &= \frac{\partial w_j^h}{\partial x_j} \end{aligned} \tag{3.7}$$

the GLS-stabilized discretized weak form of the problem has the following form. Find $(u_i^h, \ p^h) \in (\boldsymbol{S}^h, \ \boldsymbol{Q}^h)$ such that

$$\begin{aligned} \int_\Omega \left(w_i^h \rho a_j^h \frac{\partial u_i^h}{\partial x_j} + \frac{\partial w_i^h}{\partial x_j} \mu \frac{\partial u_i^h}{\partial x_j} - \frac{\partial w_i^h}{\partial x_i} p^h - w_i^h f_i \right) \ d\Omega - \oint_{\Gamma_N} w_i^h \overline{t}_i \ d\Gamma + \\ \int_\Omega q^h \frac{\partial u_j^h}{\partial x_j} \ d\Omega + \sum_e \int_{\Omega^e} \mathcal{L}(w_i^h) \tau_u^e \left(\mathcal{L}(u_i^h) - f_i \right) \ d\Omega + \\ \sum_e \int_{\Omega^e} \mathcal{L}(q^h) \tau_p^e \mathcal{L}(p^h) \ d\Omega = 0 \qquad in \ \Omega \\ u_i^h = \overline{u}_i \qquad on \ \Gamma_D \end{aligned} \tag{3.8}$$

for all $(w_i^h, \ q^h) \in (\boldsymbol{V}^h, \ \boldsymbol{Q}^h)$ where τ_u^e and τ_p^e are stabilization parameters defined for each element according to

$$\begin{aligned} \tau_u^e &= \left(\frac{4\mu}{\rho (l^e)^2} + \frac{2\|a_k\|}{l^e} \right)^{-1} \\ \tau_p^e &= \frac{4\mu}{\rho} + 2\|a_k\| l^e \end{aligned} \tag{3.9}$$

To test the formulation in figure 3.1 are illustrated the results of an example with Dirichlet condition $u_i = (-x_2, x_1)$ at the boundaries and $p = 0$ at the bottom left corner. Above linear elements are used and a body force $f_i = (-x_1, -x_2)$ is imposed. The analytical solution $p = 0$, $u_i = (-x_2, x_1)$ is obtained in the whole domain. Below, using quadratic elements, the body force is set to zero in order to test the pressure term. The analytical solution $p = \frac{1}{2}(x_1^2, x_2^2)$, $u_i = (-x_2, x_1)$ is obtained.

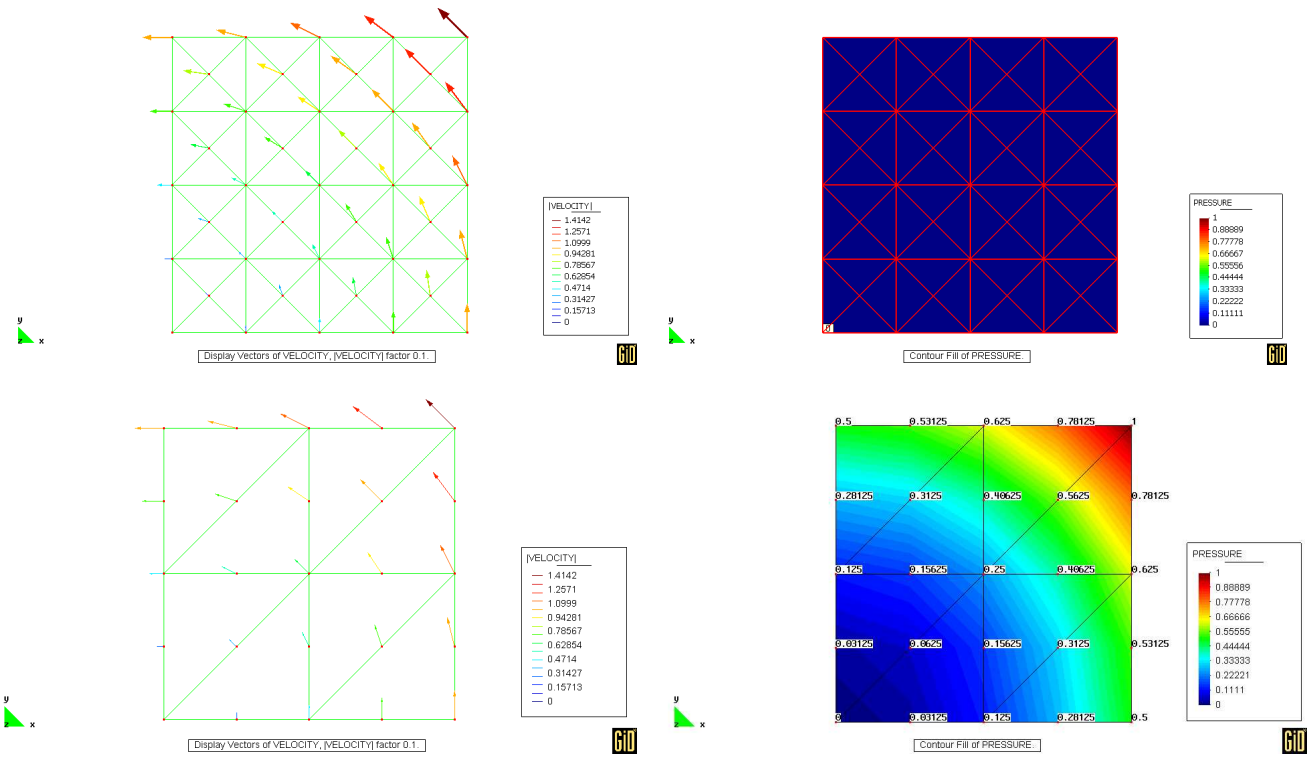

Figure 3.1: Above linear interpolation ($n = 1$). Below quadratic interpolation ($n = 2$)

Below in Figure 3.2 is the cavity example with only Dirichlet conditions, prescribed velocity $\overline{u} = (1, 0)$ at the upper edge and velocity no-slip condition at the rest of the boundary. Pressure is set to zero at the bottom left corner and the Reynolds number is 1000. Comparison between linear and quadratic elements is made. The total number of nodes is the same for the two cases. In the colorplots are visualized the norm of the velocity and the pressure field. Apart from the main vortex two secondary vortices appear, one located to the bottom right (BR) corner and one to the bottom left (BL) corner. The coordinates of the center of each vortex as well as the horizontal H and vertical V distance to the flow separation points are indicated in table 3.1.

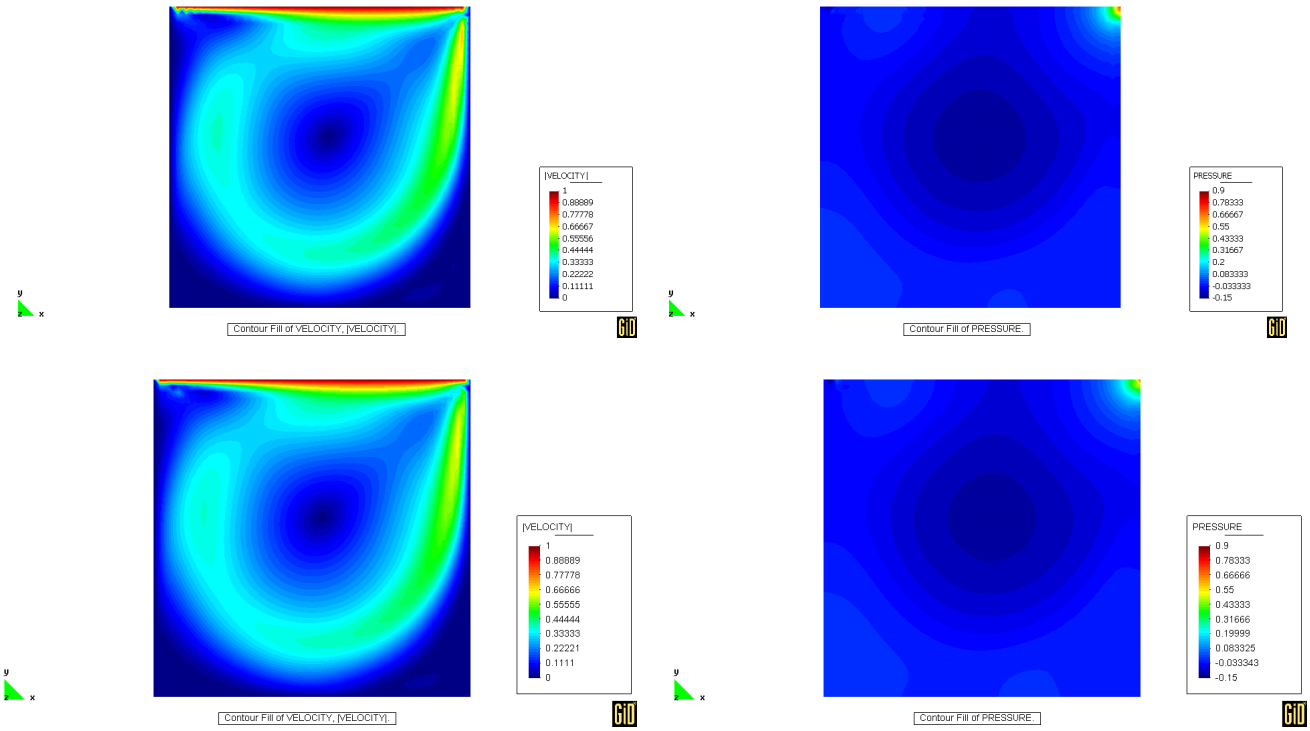

Figure 3.2: Cavity. Norm of the velocity and pressure field. GLS solution. Above linear interpolation ($n = 1$), meshsize $l^e = 0.028$. Below quadratic interpolation ($n = 2$), meshsize $l^e = 0.04$

Table 3.1: Cavity Re =1000, vortex characteristics

	Linear	Quadratic	Donea, Huerta [10]
x_c	0.530	0.531	0.540
y_c	0.568	0.566	0.573
x_{BR}	0.862	0.869	
y_{BR}	0.115	0.109	
x_{BL}	0.081	0.085	
y_{BL}	0.076	0.077	
H_{BR}	0.305	0.296	
V_{BR}	0.332	0.325	
H_{BL}	0.193	0.200	
V_{BL}	0.164	0.162	

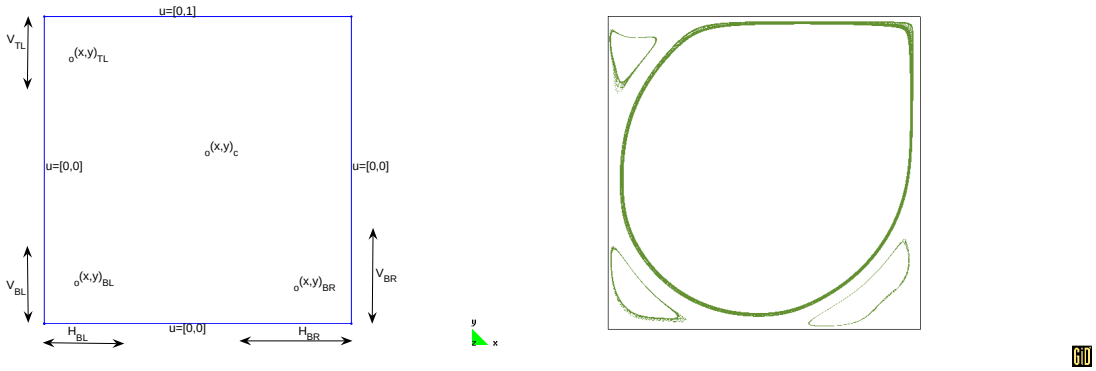

Figure 3.3: Cavity. Definition of the vortex characteristics

Transient formulation

Introducing the time derivative of the velocity in the momentum equations and using a backward Euler scheme the transient GLS-stabilized discretized weak form is written as follows.

For all time steps $n = \{1, 2, ...,$number of time steps$\}$ find $(u_i^{h,n},\ p^{h,n})\ \epsilon\ (\boldsymbol{S}^h,\ \boldsymbol{Q}^h)$ such that

$$\int_\Omega \left(w_i^h \rho \frac{\partial u_i^{h,n}}{\partial t} + w_i^h \rho a_j^{h,n} \frac{\partial u_i^{h,n}}{\partial x_j} + \frac{\partial w_i^h}{\partial x_j} \mu \frac{\partial u_i^{h,n}}{\partial x_j} - \frac{\partial w_i^h}{\partial x_i} p^{h,n} - w_i^h f_i^n \right) \, d\Omega -$$

$$\oint_{\Gamma_N} w_i^h \overline{t}_i^n \, d\Gamma + \int_\Omega q^h \frac{\partial u_j^{h,n}}{\partial x_j} \, d\Omega + \sum_e \int_{\Omega^e} \mathcal{L}(w_i^h) \tau_u^e \left(\mathcal{L}(u_i^{h,n}) + \rho \frac{\partial u_i^{h,n}}{\partial t} - f_i^n \right) \, d\Omega +$$

$$\sum_e \int_{\Omega^e} \mathcal{L}(q^h) \tau_p^e \mathcal{L}(p^{h,n}) \, d\Omega = 0 \qquad in\ \Omega$$

$$u_i^{h,n} = \overline{u}_i \qquad on\ \Gamma_D \tag{3.10}$$

for all $(w_i^h,\ q^h)\ \epsilon\ (\boldsymbol{V}^h,\ \boldsymbol{Q}^h)$ with initial conditions

$$u_i^{h,0} = \overline{u}_i^0 \qquad in\ \Omega$$

The time derivative is approximated by first order according to

$$\frac{\partial u_i^{h,n}}{\partial t} = \frac{u_i^{h,n} - u_i^{h,n-1}}{\Delta t} \tag{3.11}$$

Below is the transient solution of a flow around a cylinder with Reynolds number 2000. The above described backward Euler scheme is employed and the time step used in the simulations is $\Delta t = 0.5$. First linear triangular elements are used. The geometry with boundary conditions and the different meshes A, B and C are shown in Figure 3.4. The element size in the coarse mesh A is $l^e = 0.5$, in mesh B $l^e = 0.25$ and in mesh C $l^e = 0.16667$. The elements at the cylinder wall are 10 times smaller.

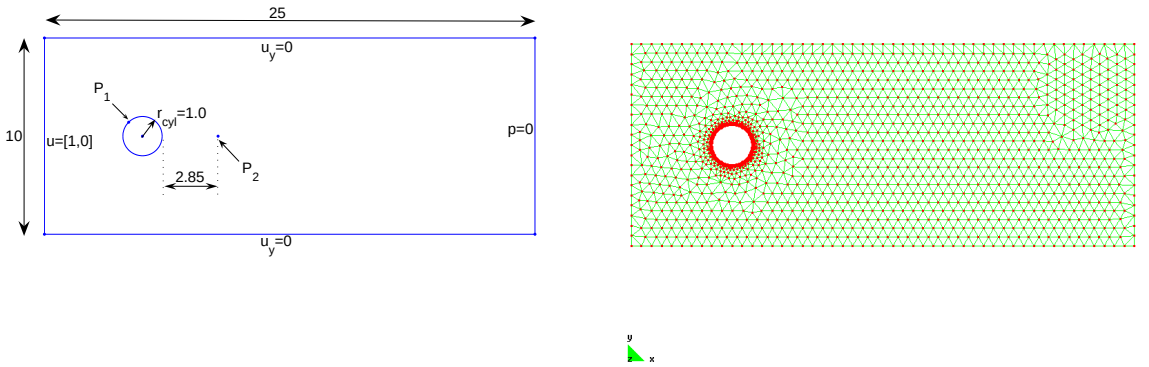

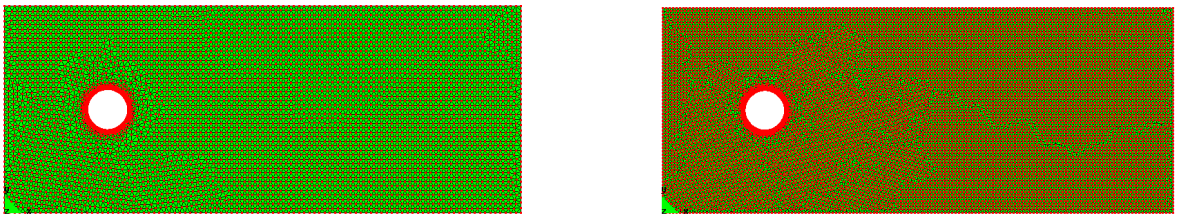

Figure 3.4: Flow around cylinder. GLS solution. Above to the right mesh A with 2920 elements. Below to the left mesh B with 10323 elements. Below to the right mesh C with 22129 elements

Quasi-stationary solutions are obtained in which periodic vortex shedding occur. In Figure 3.5 the pressure and the velocity fields at the beginning of one vortex shedding period are shown.

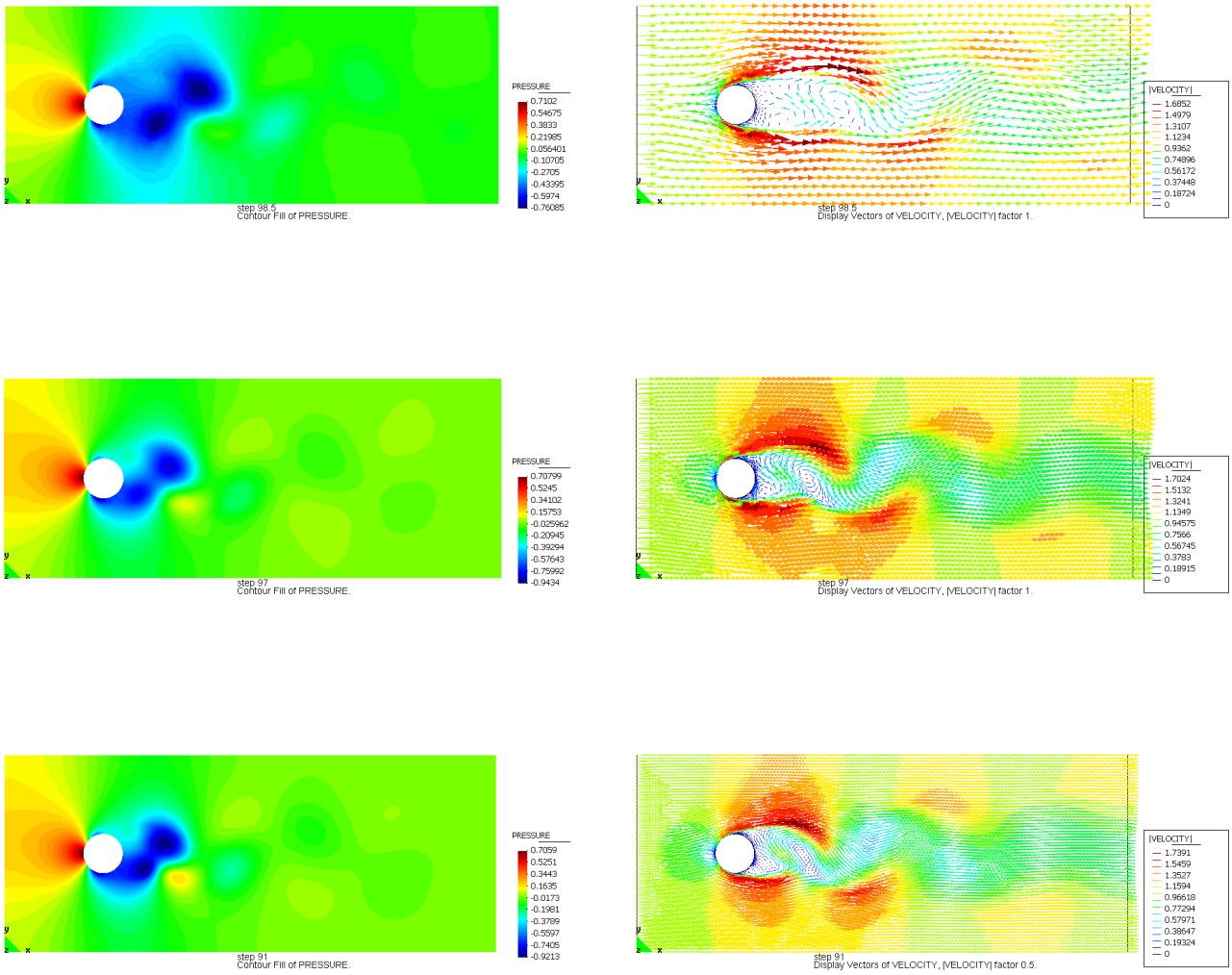

Figure 3.5: Flow around cylinder, linear elements. GLS solution. From above mesh A($l^e = 0.5$), mesh B($l^e = 0.25$) and mesh C($l^e = 0.16667$). Pressure and velocity field

In Figure 3.6 the pressure at point P_1 on the cylinder wall, the velocity components at point P_2 2.85 units downstream of the cylinder as well as drag and lift forces are plotted versus time. The points P_1 and P_2 are defined in Figure 3.4.

It can be seen that mesh A is too coarse for representing the flow correctly.

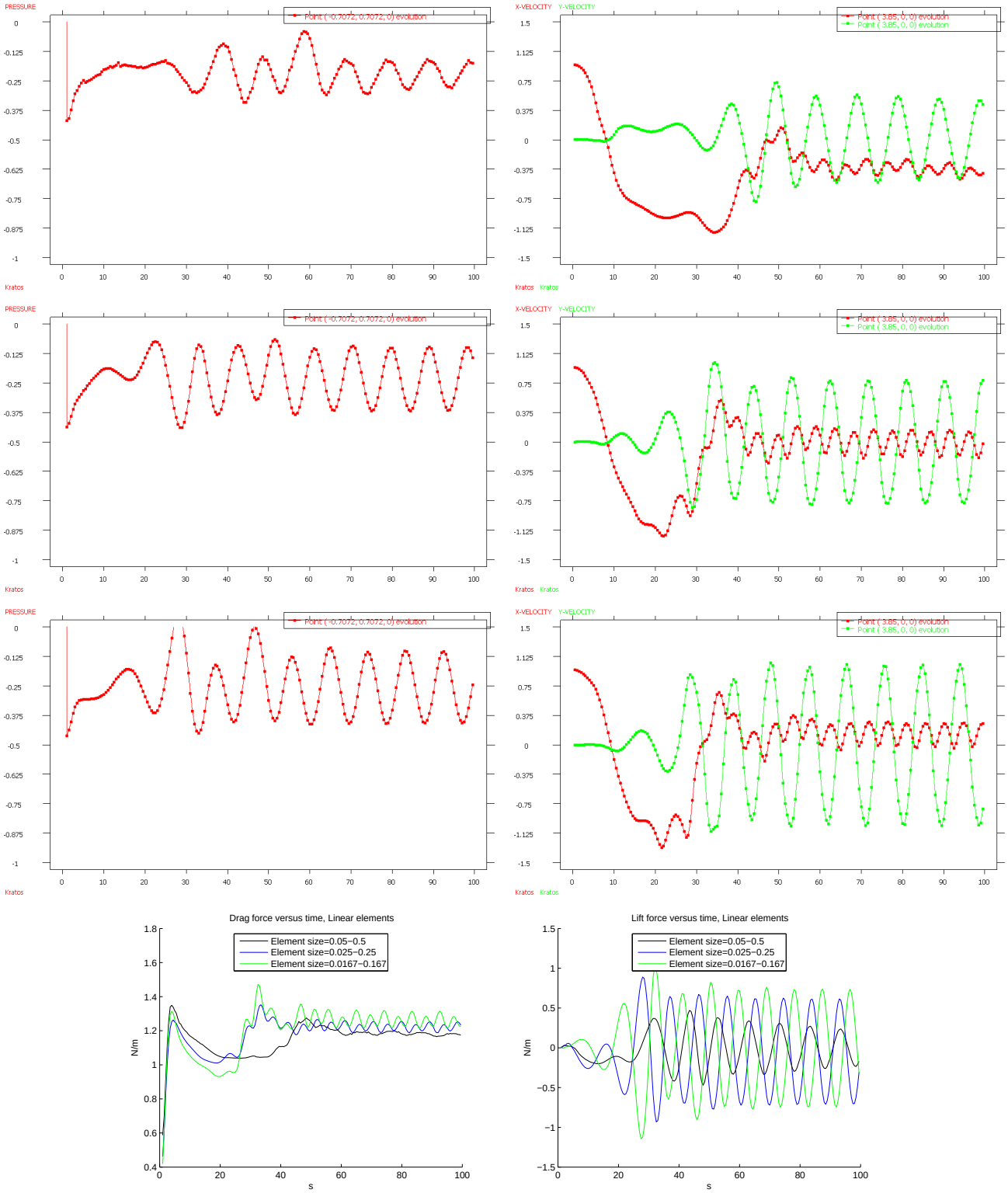

Figure 3.6: Flow around cylinder, linear elements. Time development of GLS solution. Left: pressure in P_1. Right: velocity components in P_2. From above mesh A, B and C. Below drag and lift forces.

Below quadratic elements are employed using the same problem setup as for linear elements. Two meshes are used. The coarser mesh to the left consists of 907 6-noded triangular elements whereas the finer mesh to the right has 2920 elements.

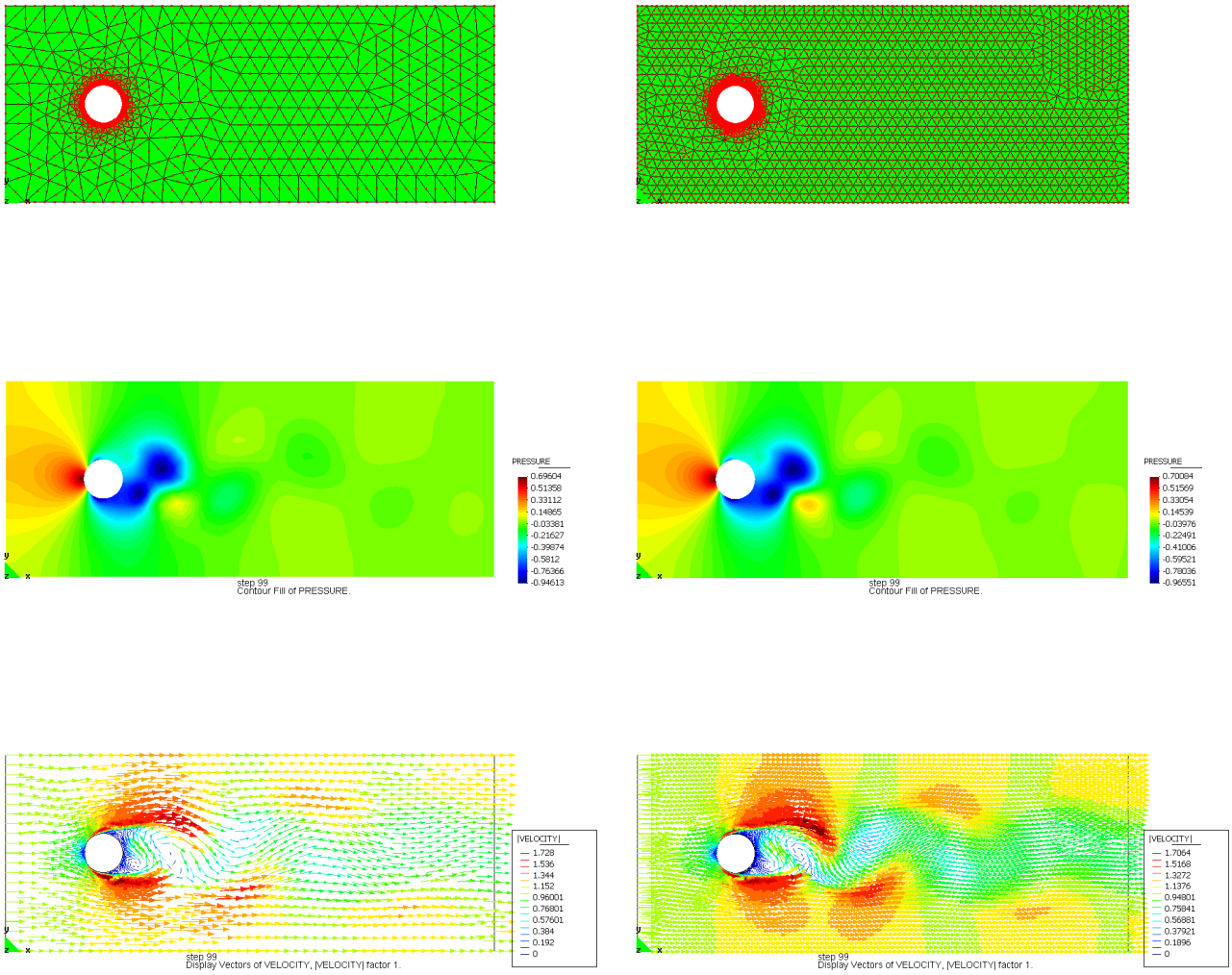

Figure 3.7: Flow around cylinder, quadratic elements. GLS solution. Coarse mesh with $l^e = 1.0$ and fine mesh with $l^e = 0.5$

The plots of the pressure and velocity field are shown above in figure 3.7. Figure 3.8 shows the time evolution of the pressure and velocity components as well as the drag and lift forces are illustrated.

The quadratic results from the two meshes coincide reasonably well between themselves and with the linear results using meshes B and C. The computed Strouhal numbers are listed in table 3.2.

Table 3.2: Flow around cylinder. Strouhal number for the different meshes

Linear elements		Quadratic elements	
Mesh A	0.202	Coarse mesh	0.217
Mesh B	0.218	Fine mesh	0.220
Mesh C	0.219		
Experimental value [33]	0.21		

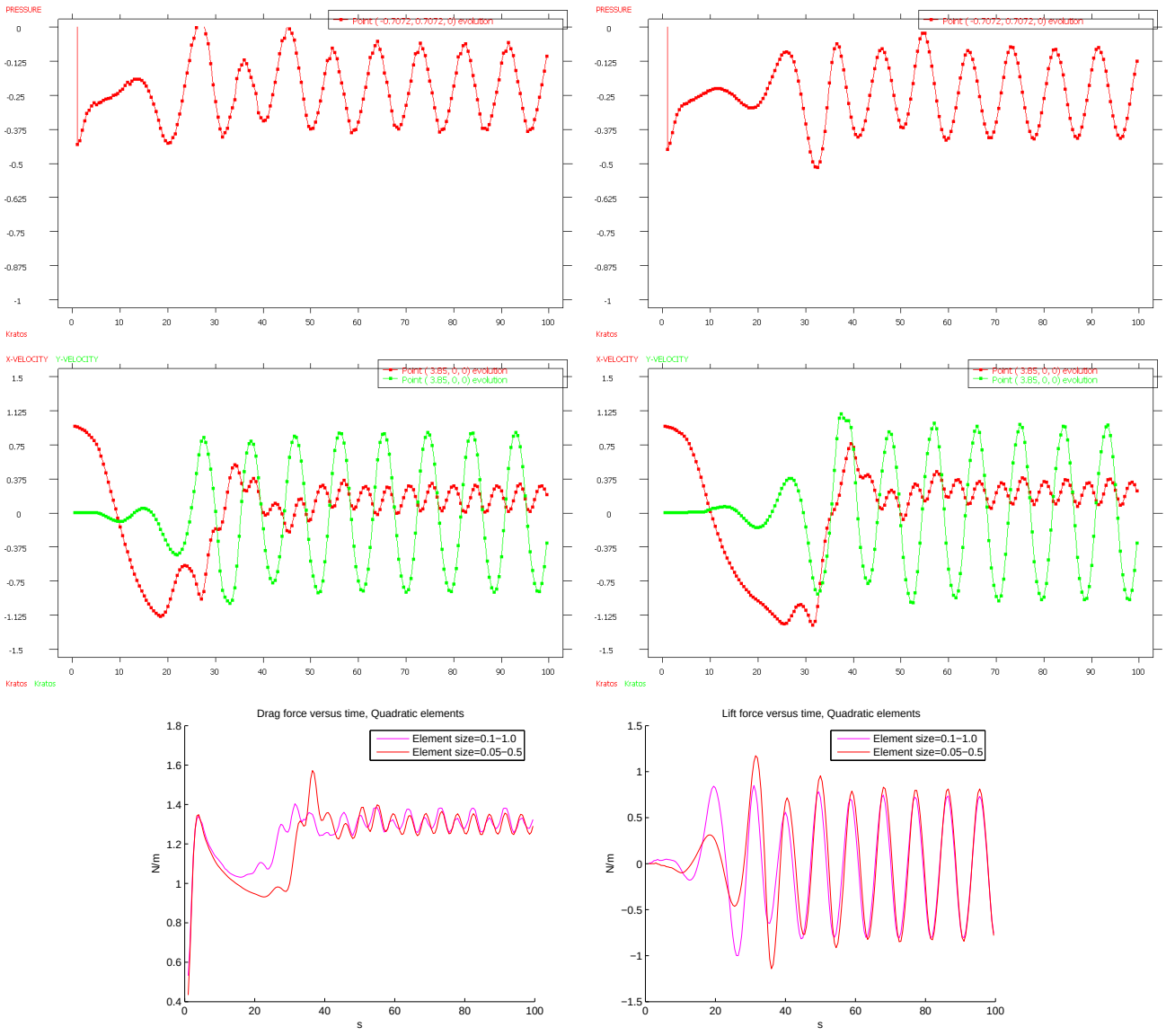

Figure 3.8: Flow around cylinder, quadratic elements. GLS solution. From above: evolution of pressure at point P_1, velocity components at point P_2, drag and lift forces

3.2 ALE formulation

The transient Navier-Stokes equations are written in an arbitrary Lagrangian-Eulerian (ALE) form. To motivate this choice first the advantages and disadvantages of the two classical approaches, the Lagrangian and the Eulerian approach, should be pointed out.

The basic idea in the Eulerian approach is that the physical quantities evaluated in the fluid are associated to a fixed region of space. The equations are formulated in terms of the spatial coordinates x_i and the time t. The mesh is fixed in time and complex fluid patterns like vortices etc can be simulated as might occur in flows with high Reynolds number. However, since this does not allow the fluid domain to move, it does not apply to fluid-structure interaction problems with a moving interface. The transient momentum equation with the Eulerian approach takes the following form.

$$\rho\frac{\partial u_i}{\partial t} + \rho u_j\frac{\partial u_i}{\partial x_j} - \mu\frac{\partial^2 u_i}{\partial x_j^2} + \frac{\partial p}{\partial x_i} - f_i = 0$$

On the other hand, in the Lagrangian approach, the physical quantities are attached to the material, that is the equations are formed for the moving fluid keeping track of the fluid particles. This makes it easy to take into account history-dependence of the motion of the material. The freedom of following a changing geometry makes the Lagrangian approach suitable for modeling problems including free surfaces and flow separation which may occur in for example marine applications. The drawback is that a loss of accuracy is expected if the flow pattern is complex or in the case of large deformations. Remeshing at several or at each time step may be needed which is costly.

For these reasons from now on the ALE-approach is used as it combines the advantages of the Eulerian and the Lagrangian formulation making it suitable for fluid-structure interaction applications. In the ALE-formulation the mesh is allowed to move with an arbitrary mesh velocity v_i^h different from the velocity u_i^h. v_i^h is chosen so that it follows moving boundaries, such as those at the interface of a deformable structural domain.

The fluid domain is now free to change in time which has essential advantages in fluid-structure interaction problems. In the numerical formulation of the Navier-Stokes equations the ALE-formulation introduces a new transport term. This can be seen as a modification of the convection term and, using GLS-stabilization, the problem to solve, expressed in its discretized weak form, is now the following.

For all time steps $n = \{1, 2, ...,\text{number of time steps}\}$ find $(u_i^{h,n},\ p^{h,n})\ \epsilon\ (\boldsymbol{S}^h,\ \boldsymbol{Q}^h)$ such that

$$\int_\Omega \left(\rho w_i^h \frac{\partial u_i^{h,n}}{\partial t} + \rho w_i^h (u_j^{h,n} - v_j^{h,n}) \frac{\partial u_i^{h,n}}{\partial x_j} + \frac{\partial w_i^h}{\partial x_j} \mu \frac{\partial u_i^{h,n}}{\partial x_j} - \frac{\partial w_i^h}{\partial x_i} p^{h,n} - w_i^h f_i^n \right) \, d\Omega -$$
$$\oint_{\Gamma_N} w_i^h \overline{t}_i^n \, d\Gamma + \sum_e \int_{\Omega^e} \mathcal{L}(w_i^h) \tau_u^e \left(\mathcal{L}(u_i^{h,n}) + \rho \frac{\partial u_i^{h,n}}{\partial t} - f_i^n \right) \, d\Omega +$$
$$\int_\Omega q^h \frac{\partial u_j^{h,n}}{\partial x_j} \, d\Omega + \sum_e \int_{\Omega^e} \mathcal{L}(q^h) \tau_p^e \mathcal{L}(p^{h,n}) \, d\Omega = 0 \qquad in\ \Omega$$
$$u_i^h = \overline{u}_i \qquad on\ \Gamma_D \tag{3.12}$$

for all $(w_i^h,\ q^h)\ \epsilon\ (\boldsymbol{V}^h,\ \boldsymbol{Q}^h)$ with initial conditions

$$u_i^{h,0} = \overline{u}_i^0 \qquad in\ \Omega$$

3.2.1 Mesh moving strategy

Moving the nodes at each time step so they fit to the time dependent computational domain requires a strategy so that the elements do not become distorted. As the positions of the nodes at the boundaries are predetermined, fixed at the external boundaries or following the movement of the structure at the fluid-structure interface, the positions of the internal nodes have to be calculated.

Different approaches to determine the positions in an optimal way exist, defining master-slave nodes and moving them using some kinematic assumptions, with the objective of obtaining good quality of the mesh and avoid distorsion.

Most common is perhaps solving a fictitious elastic problem in the fluid domain and using the displacements as the new node positions. Here a particular and very simple case of this family of methods is adapted: the Laplacian method, originally introduced as a mesh smoothing technique [17]. This consists of solving a Laplacian form in each dimension separately for computing the new positions of the nodes. The method works fine if the mesh movements are not too large and if the stiffness is increased for smaller elements.

In order to illustrate how this mesh moving strategy works below is an example with a horizontal flow around a square solid. The solid is considered as a rigid body but it has not any degree of freedom fixed. The pressure from the fluid sets the square in movement towards the right only resisted by inertial forces due to its mass. As the solid changes position the ALE-formulation allows the fluid mesh to move. This is done with the Laplacian method and when the mesh displacement gets too large the smaller elements close to the solid interface become distorted as shown in Figure 3.10. The ALE-scheme breaks down at $t \simeq 80$ and the mesh displacement for a critical node is plotted in figure 3.11.

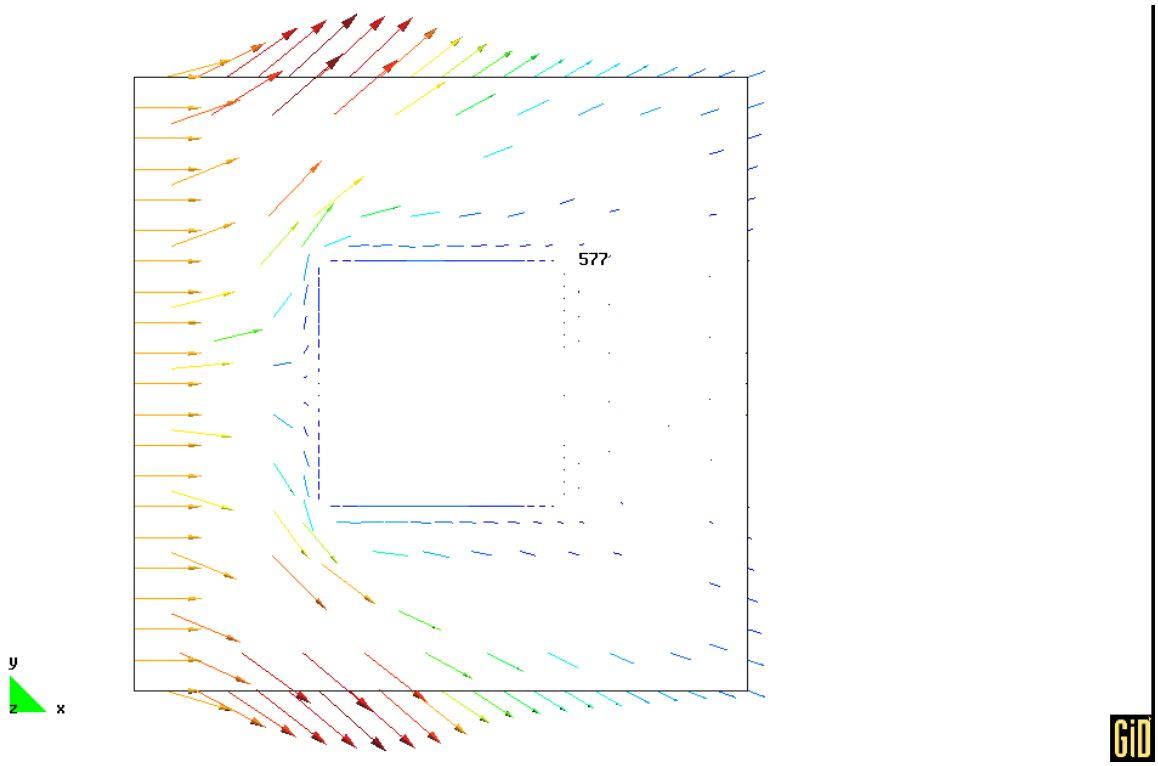

Figure 3.9: Velocity field at time $t = 50$

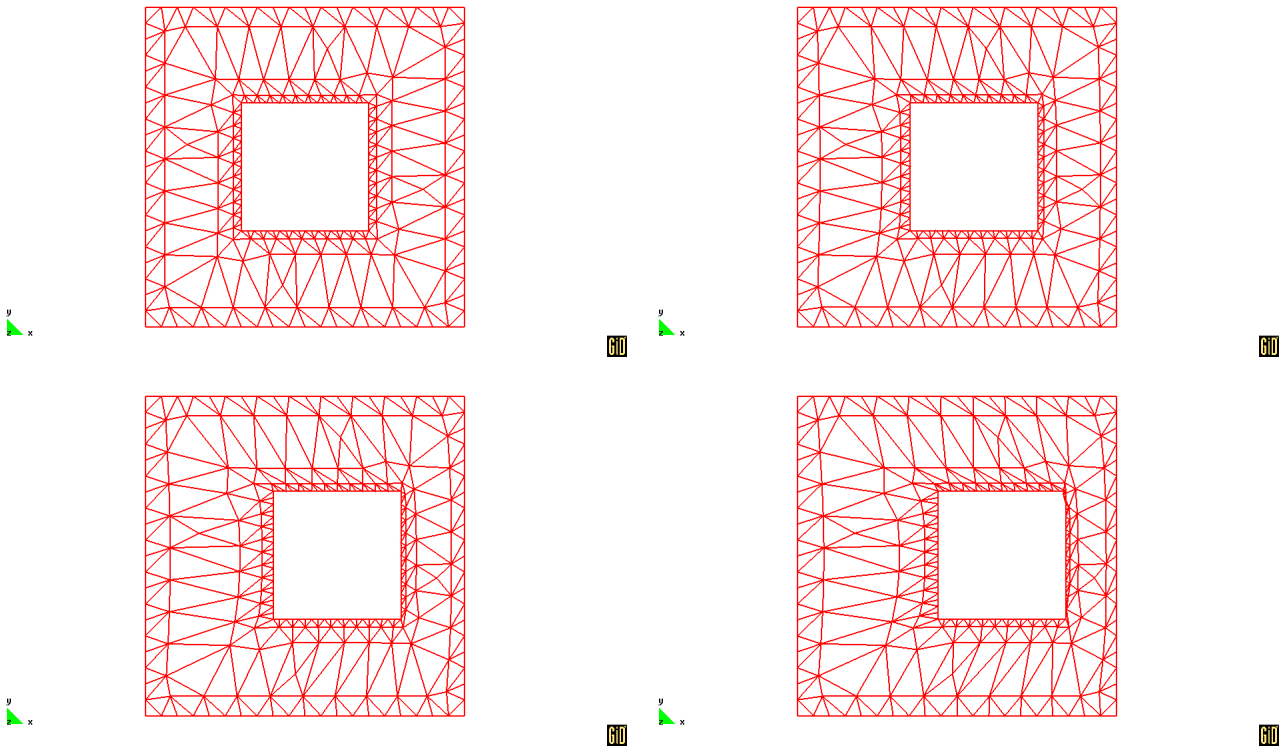

Figure 3.10: ALE meshes at time $t = 0$, 30, 60 & 90

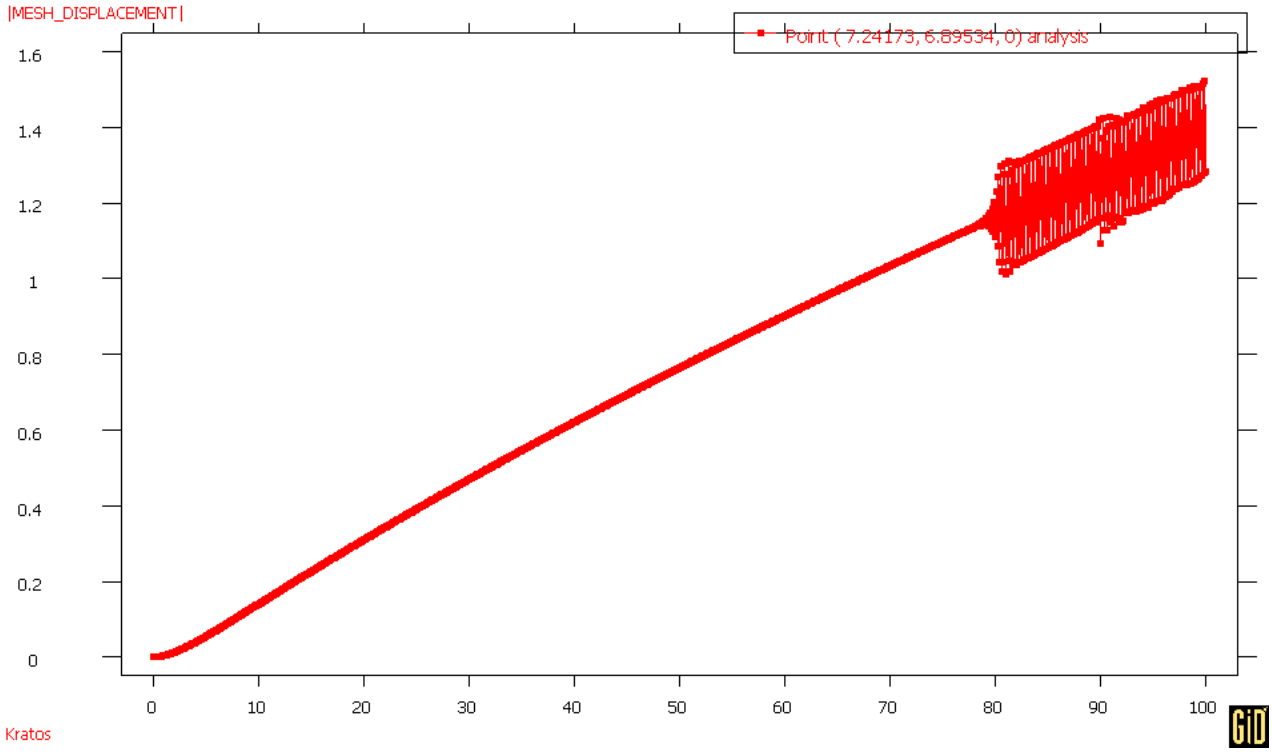

Figure 3.11: Absolute value of mesh displacement at node 577.

3.3 Finite Calculus

In this section the Finite Calculus (FIC) equations for an incompressible flow are implemented. The equations are written in the principle curvature direction of the solution. As pointed out in previous Chapter 2, dealing with the convection-diffusion problem, the basis of the FIC method is invoking the balance of fluxes in a domain of finite size. This introduces at the continuous level new terms in the equations which after discretizing the problem with finite elements have stabilizing properties.

In order to illustrate how this works first the stationary Navier-Stokes momentum equation in a 1D domain Ω is considered

$$\rho u \frac{du}{dx} - \frac{d\sigma}{dx} - f = 0 \qquad in\ \Omega \tag{3.13}$$

It can be expressed in terms of the "flux" q according to

$$\frac{dq}{dx} = f \qquad in\ \Omega$$

where

$$q = \frac{1}{2}\rho u^2 - \sigma$$

A finite subdomain $\Omega^l \subset \Omega$ with length l is now considered, see Figure 3.12. The balance of fluxes in Ω^l is expressed as

$$q_A - q_B + \int_{\Omega^l} f(x)dx = 0 \tag{3.14}$$

The integral of the body force term f is computed as

$$\int_{\Omega^l} f(x)dx = l\frac{f_A + f_B}{2} + \mathcal{O}(l^2) \tag{3.15}$$

where the force at point A and B is expressed using a first order Taylor expansion around point C according to

$$f_A = f_C - l_1 \frac{df}{dx}|_C + \mathcal{O}(l^2)$$
$$f_B = f_C + l_2 \frac{df}{dx}|_C + \mathcal{O}(l^2)$$

Furthermore the fluxes are expressed with second order Taylor expansion

$$q_A = q_C - l_1 \frac{dq}{dx}|_C + \frac{l_1^2}{2}\frac{d^2q}{dx^2}|_C + \mathcal{O}(l^3)$$
$$q_B = q_C + l_2 \frac{dq}{dx}|_C + \frac{l_2^2}{2}\frac{d^2q}{dx^2}|_C + \mathcal{O}(l^3) \tag{3.16}$$

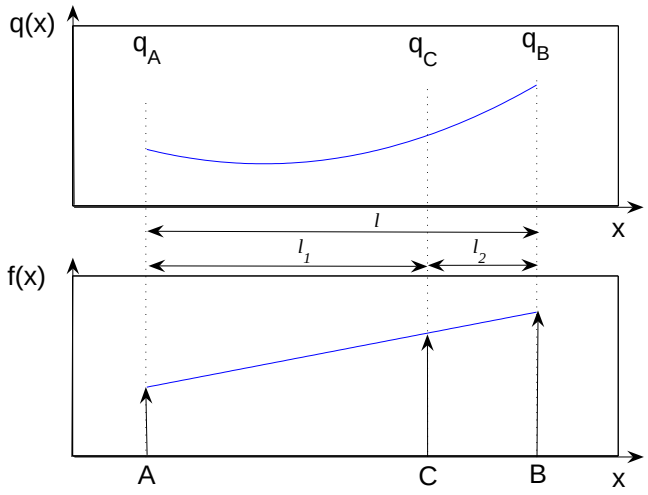

Figure 3.12: Balance of flux in a finite domain.

Inserting Equation (3.16) and (3.15) into (3.14) and defining the characteristic length $h = l_1 - l_2$ the balance of fluxes becomes

$$q_A - q_B + \int_{\Omega^l} f(x)dx =$$
$$-l\frac{dq}{dx}|_C + \frac{hl}{2}\frac{d^2q}{dx^2}|_C + \frac{l}{2}\left(2f_C - h\frac{df}{dx}|_C\right) + \mathcal{O}(l^2) = 0$$

Division by $(-l)$ gives

$$\frac{dq}{dx}|_C - \frac{h}{2}\frac{d^2q}{dx^2}|_C - f_C + \frac{h}{2}\frac{df}{dx}|_C + \mathcal{O}(l) = 0 \tag{3.17}$$

Equation (3.17) is now brought back to the continuous level by stating $\frac{dq}{dx}|_C \approx \frac{dq}{dx} = u\frac{du}{dx} - \frac{d\sigma}{dx}$ and $Q_C \approx Q$ and hereby the FIC equation is obtained as

$$u\frac{du}{dx} - \frac{d\sigma}{dx} - f - \frac{h}{2}\frac{d}{dx}\left(u\frac{du}{dx} - \frac{d\sigma}{dx} - f\right) = 0 \qquad in\ \Omega \tag{3.18}$$

or expressed in terms of the residual of the original differential equation

$$r - \frac{h}{2}\frac{dr}{dx} = 0 \qquad in\ \Omega \tag{3.19}$$

where $r = u\frac{du}{dx} - \frac{d\sigma}{dx} - f$

In the multidimensional case the corresponding system of equations, also including the divergence equation is written as

$$r_{m_i} - \frac{h_{ij}}{2}\frac{\partial r_{m_i}}{\partial x_j} = 0 \qquad a)$$
$$r_d - \frac{h_k}{2}\frac{\partial r_d}{\partial x_k} = 0 \qquad b) \tag{3.20}$$

where the residuals of the momentum equation and the divergence equations are expressed as

$$r_{m_i} = \rho\frac{\partial u_i}{\partial t} + \rho(u_j - v_j)\frac{\partial u_i}{\partial x_j} - \frac{\partial \sigma_{ij}}{\partial x_j} - f_i \tag{3.21}$$

$$r_d = \frac{\partial u_k}{\partial x_k} \tag{3.22}$$

with the stress tensor σ_{ij}, consisting of a viscous part and the pressure, explicitly written as

$$\sigma_{ij} = 2\mu\left(\frac{1}{2}\left(\frac{\partial u_i}{\partial x_j} + \frac{\partial u_j}{\partial x_i}\right) - \frac{1}{3}\frac{\partial u_k}{\partial x_k}\delta_{ij}\right) - p\delta_{ij}$$

The following definitions are introduced

$$\overline{r}_{m_i} = r_{m_i} - \frac{2\mu}{3}\frac{\partial r_d}{\partial x_i} \tag{3.23}$$

$$R_{m_i} = r_{m_i} + \rho u_i \cdot r_d \tag{3.24}$$

The FIC equation for this modified residual of the momentum equation R_{m_i} is expressed as

$$R_{m_i} - \frac{h_{ik}}{2}\frac{\partial R_{m_i}}{\partial x_k} = r_{m_i} + \rho u_i \cdot r_d - \frac{h_{ik}}{2}\frac{\partial R_{m_i}}{\partial x_k} = 0$$

Substituting r_{m_i} from Equation (3.23) and r_d from Equation (3.20b) leads to

$$\overline{r}_{m_i} + \frac{2\mu}{3}\frac{\partial r_d}{\partial x_i} + \rho u_i \frac{h_k}{2}\frac{\partial r_d}{\partial x_k} = \frac{h_{ik}}{2}\frac{\partial R_{m_i}}{\partial x_k}$$

By making the approximations $\overline{r}_{m_i} \approx 0$ and $R_{m_i} \approx r_{m_i}$ the following expression is obtained

$$\frac{\partial r_d}{\partial x_k} = \left(\frac{h_{kk}}{\rho u_k \cdot h_k + \frac{4}{3}\mu}\right)\frac{\partial r_{m_k}}{\partial x_k}$$

which is substituted in (3.20*b*). This results in a FIC divergence equation expressed in terms of the residual of the momentum equation, according to

$$r_d - \frac{\tau_k}{\rho}\frac{\partial r_{m_k}}{\partial x_k} = 0 \qquad \text{where} \qquad \tau_k = \frac{h_k \cdot h_{kk}}{2u_k \cdot h_k + \frac{8\mu}{3\rho}} \tag{3.25}$$

The stabilization parameter τ_k is sometimes called the time intrinsic parameter. There exists the possibility of calculating a scalar τ which yield for all directions within one element. The characteristic lengths are simply taken as a typical element size l^e and the expression for τ then becomes

$$\tau^e = \left(\frac{8\mu}{3\rho(l^e)^2} + \frac{2\|u_k\|}{l^e}\right)^{-1} \tag{3.26}$$

Regarding the momentum equations, since the flow is incompressible, the viscous part of the gradient of the stress tensor can be written in Laplacian form and Equation (3.20*a*) is simplified according to

$$r_{m_i} - \frac{h_{ij}}{2}\frac{\partial r_{m_i}}{\partial x_j} = 0 \tag{3.27}$$

where $r_{m_i} = \rho\frac{\partial u_i}{\partial t} + \rho(u_j - v_j)\frac{\partial u_i}{\partial x_j} - \mu\frac{\partial^2 u_j}{\partial x_j^2} + \frac{\partial p}{\partial x_i} - f_i$

The last concern before stating the strong form of the FIC equations for an incompressible flow is expressing the momentum equations in the direction of the principle curvatures of the solution. This was done in previous Chapter 2 for the scalar convection-diffusion equation. The only difference now is that it is done for each velocity component separately. The basis of this new coordinate system is denoted by ξ_j and quantities that are expressed in it with a prime. Using this notation the strong form of the FIC formulated incompressible Navier-Stokes equations are

$$\begin{aligned}
\rho\frac{\partial u_i'}{\partial t} + \rho(u_j' - v_j')\frac{\partial u_i'}{\partial \xi_j} - \mu\frac{\partial^2 u_i'}{\partial \xi_j^2} + \frac{\partial p}{\partial \xi_i} - f_i' - \frac{h_{ij}'}{2}\frac{\partial r_{m_i}'}{\partial \xi_j} = 0 \qquad & in\ \Omega \qquad a)\\
\frac{\partial u_k}{\partial x_k} - \frac{\tau}{\rho}\frac{\partial r_{m_k}}{\partial x_k} = 0 \qquad & in\ \Omega \qquad b)\\
n_j \cdot \left(\mu\frac{\partial u_i'}{\partial \xi_j} - p\delta_{ij}\right) - \overline{t}_i' + n_j \cdot \frac{h_{ij}'}{2} r_{m_i}' = 0 \qquad & on\ \Gamma_N \qquad c)\\
u_i' = \overline{u}_i' \qquad & on\ \Gamma_D \qquad d)
\end{aligned} \tag{3.28}$$

where $r_{m_i}' = \rho\frac{\partial u_i'}{\partial t} + \rho(u_j' - v_j')\frac{\partial u_i'}{\partial \xi_j} - \mu\frac{\partial^2 u_i'}{\partial \xi_j^2} + \frac{\partial p}{\partial \xi_i} - f_i'$

The characteristic length tensor $h_{ij}'(\xi_i)$ is now transformed to $h_{ij}(x_i)$ in the original basis and other quantities are also expressed in the original x_i coordinate system.

Furthermore, introducing projections of the convection term (c_i) and of the pressure gradient (π_i), it is possible to express r_{m_i} as follows

$$r_{m_i} = \rho(u_j - v_j)\frac{\partial u_i}{\partial x_j} - \rho c_i$$
$$r_{m_i} = \frac{\partial p}{\partial x_i} - \pi_i$$

The vanishing of the momentum residuals introduces two new equations, one for each projection.

$$\rho(u_j - v_j)\frac{\partial u_i}{\partial x_j} - \rho c_i = 0 \qquad a)$$
$$\frac{\partial p}{\partial x_i} - \pi_i = 0 \qquad b) \tag{3.29}$$

The Galerkin procedure is now carried out for Equation (3.28) and (3.29) leading to the following weak form of the problem.

Find $u_i \epsilon \boldsymbol{S}$ and $(p,\ c_i,\ \pi_i)\epsilon \boldsymbol{Q}$ such that

$$\int_\Omega \left(\rho w_i \left(\frac{\partial u_i}{\partial t} + (u_j - v_j)\frac{\partial u_i}{\partial x_j}\right) + \frac{\partial w_i}{\partial x_j}\left(\mu\frac{\partial u_i}{\partial x_j} - p\delta_{ij}\right) - f_i\right)\, d\Omega - \int_{\Gamma_N} w_i \bar{t}_i\, d\Gamma +$$
$$\int_\Omega \rho\frac{h_{ij}}{2}\frac{\partial w_i}{\partial x_j}\left((u_j - v_j)\frac{\partial u_i}{\partial x_j} - c_i\right)\, d\Omega + \int_\Omega q\frac{\partial u_k}{\partial x_k}\, d\Omega + \int_\Omega \frac{\tau}{\rho}\frac{\partial q}{\partial x_k}\left(\frac{\partial p}{\partial x_k} - \pi_k\right) +$$
$$\int_\Omega \rho\zeta_i\left((u_j - v_j)\frac{\partial u_i}{\partial x_j} - c_i\right)\, d\Omega + \int_\Omega \chi_i\left(\frac{\partial p}{\partial x_i} - \pi_i\right)\, d\Omega = 0 \qquad in\ \Omega$$
$$u_i = \overline{u}_i \qquad on \Gamma_D \tag{3.30}$$

for all $w_i \epsilon \boldsymbol{V}$ and $(q,\ \zeta_i,\ \chi_i)\epsilon \boldsymbol{Q}$

3.3.1 Spatial discretization

The domain is subdivided into finite elements with an equal order approximation of all the variables using linear shape functions N^a according to

$$u_i^h = \sum_{a=1}^{number\ of\ nodes} N_i^a \cdot \hat{u}_i^a$$
$$p^h = \sum_{a=1}^{number\ of\ nodes} N^a \cdot \hat{p}^a$$
$$c_i^h = \sum_{a=1}^{number\ of\ nodes} N_i^a \cdot \hat{c}_i^a$$
$$\pi_i^h = \sum_{a=1}^{number\ of\ nodes} N_i^a \cdot \hat{\pi}_i^a$$

where $(\hat{\cdot})$ denote nodal variables.

The piecewise constant stabilization parameters h_{ij} and τ_i are evaluated in the center of each element. In matrix form the system of discrete variables to be solved is expressed as follows.

$$\begin{aligned} M \cdot \frac{\partial \hat{u}_i}{\partial t} + (A(u_j) + K + H) \cdot \hat{u}_i - G \cdot \hat{p} - C \cdot \hat{c}_i - F = 0 \qquad a) \\ G^T \cdot \hat{u}_j + \frac{\tau}{\rho} L \cdot \hat{p} - \frac{\tau}{\rho} Q \cdot \hat{\pi}_j = 0 \qquad b) \\ A(\hat{u}_j) \cdot \hat{u}_i - M \cdot \hat{c}_i = 0 \qquad c) \\ Q^T \cdot \hat{p} - \frac{1}{\rho} M \cdot \hat{\pi}_i = 0 \qquad d) \end{aligned} \tag{3.31}$$

where

$$M = \int_{\Omega^e} \rho N^a N^b d\Omega \qquad A(u_j) = \int_{\Omega^e} N^a \rho (u_j^h - v_j^h) \frac{\partial N^b}{\partial x_j} d\Omega$$

$$K = \int_{\Omega^e} \frac{\partial N^a}{\partial x_j} \mu \frac{\partial N^b}{\partial x_j} d\Omega \qquad H = \int_{\Omega^e} \rho \frac{h_{ij}}{2} \frac{\partial N^a}{\partial x_j} (u_k^h - v_k^h) \frac{\partial N^b}{\partial x_k} d\Omega$$

$$G = \int_{\Omega^e} \frac{\partial N^a}{\partial x_i} N^b d\Omega \qquad C = \int_{\Omega^e} \rho \frac{h_{ij}}{2} \frac{\partial N^a}{\partial x_j} N^b d\Omega$$

$$F = \int_{\Omega^e} N^a f_i d\Omega \qquad L = \int_{\Omega^e} \frac{\partial N^a}{\partial x_j} \frac{\partial N^b}{\partial x_j} d\Omega \qquad Q = \int_{\Omega^e} \frac{\partial N^a}{\partial x_j} N^b d\Omega$$

Upper index a refer to the nodal test functions and b to the interpolating functions of the nodal unknowns.

3.3.2 Time integration

The time integration is carried out using a second order fractional step scheme. The fractional velocity u_i^* is introduced and Equation (3.31a) is split in two equations. Together with Equation (3.31b), for each time step n, following system of equations is obtained.

$$\begin{aligned} M \cdot \frac{\hat{u}_i^* - \hat{u}_i^n}{\Delta t} + (A(u_j^*) + K + H) \cdot \hat{u}_i^* - G \cdot \hat{p}^n - C \cdot \hat{c}_i^n - F = 0 \qquad a) \\ M \cdot \frac{\hat{u}_i^{n+1} - \hat{u}_i^*}{\Delta t} - G \cdot (\hat{p}^{n+1} - \hat{p}^n) = 0 \qquad b) \\ G^T \cdot \hat{u}_j^{n+1} + \frac{\tau}{\rho} L \cdot \hat{p}^{n+1} - \frac{\tau}{\rho} Q \cdot \hat{\pi}_j^n = 0 \qquad c) \end{aligned} \tag{3.32}$$

As the first step, which is non-linear, u_i^* is solved from Equation (3.32a) for each dimension i and iterated until convergence is achieved. Then substituting $\hat{u}_i^{n+1}$ from Equation (3.32b) into (3.32c) the following expression is formed.

$$G^T \cdot \hat{u}_j^* + \frac{\Delta t}{\rho} L \cdot \left(\hat{p}^{n+1} - \hat{p}^n \right) + \frac{\tau}{\rho} L \cdot \hat{p}^{n+1} - \frac{\tau}{\rho} Q \cdot \hat{\pi}_j^n = 0 \tag{3.33}$$

In (3.33) we have introduced the approximation $G^T M^{-1} G \simeq \frac{1}{\rho} L$. In the third and fourth steps the projection variables $\hat{c}_i^{n+1}$ and $\hat{\pi}_i^{n+1}$ are solved from

$$A(u_j^*) \cdot \hat{u}_i^* - M_d \cdot \hat{c}_i^{n+1} = 0 \tag{3.34}$$

$$Q^T \cdot \hat{p}^{n+1} - \frac{1}{\rho} M_d \cdot \hat{\pi}_i^{n+1} = 0 \tag{3.35}$$

where M_d is the lumped mass matrix.

Finally $\hat{u}_i^{n+1}$ is solved from (3.32*b*), also using the lumped mass matrix.

3.3.3 Characteristic length

The calculation of the characteristic length tensor h_{ij} is presented in the algorithm below.

Algorithm for computing h_{ij}

The tensor h_{ij} is taken constant within each element and the $i-$th row of h_{ij} is to be evaluated in each nonlinear iterative step solving the $i-$th component of the fractional velocity $\hat{u}_i^*$. The steps in this computing procedure are summarized as:

• Defining the advective velocity $a_j = (u_j^* - v_j)$ at the centre of the element

If $a_j \neq 0$

• Evaluate $\frac{\partial u_i}{\partial x_j}$

For $i = 1, 2, 3$

If $|\frac{\partial u_i}{\partial x_j}| \cdot l < 0.001$

• $\xi_j = \frac{a_j}{|a_j|}$

Else

• $\xi_j = \frac{\partial u_i}{\partial x_j} / |\frac{\partial u_i}{\partial x_j}|$

• Evaluate $a_j \bigotimes \xi_j$

If $|a_j \bigotimes \xi_j| \neq 0$

• $\eta_j = \frac{a_j \bigotimes \xi_j}{|a_j \bigotimes \xi_j|}$

Else If $\xi_1^2 + \xi_2^2 \neq 0$

• $\eta_j = [\xi_2,\ -\xi_1,\ 0]/(\xi_1^2 + \xi_2^2)$

Else

- $\eta_j = [-\xi_3,\ 0,\ \xi_1]/(\xi_1^2 + \xi_3^2)$

- Evaluate $\zeta_j = \xi_j \bigotimes \eta_j$

- $T_{kj} = \begin{bmatrix} \xi_j \\ \eta_j \\ \zeta_j \end{bmatrix}$

- $u'_k = T_{kj} \cdot a_j$

- $l'_k = \underset{n}{max}\ (T_{kj} \cdot d_{nj})$ where d_{nj} describe the n edges of the triangle or tetrahedra

- $h'_k = \left(\coth(\gamma'_k) - \frac{1}{\gamma'_k}\right) \cdot l'_k$ where the Peclet number $\gamma'_k = \frac{\rho u'_k l'_k}{2\mu}$, no sum over k

- $h_{ij} = T_{kj} \cdot h'_k$

Else

- $h_{ij} = 0$

3.3.4 Numerical examples

The numerical solutions of three classical problems are now obtained in order to test the method. These are the cavity flow, flow around a cylinder and the backward facing step. The above presented fractional step scheme is used and the solution is brought to steady-state in the case of the cavity and backward facing step flows. The flow around a cylinder reaches an oscillating quasi-stationary behavior. The results are compared to experimental and numerical results from other works.

Cavity flow

The domain consists of a unit square with prescribed velocity $u_i = (1, 0)$ at the upper boundary, fixed at the other boundaries and prescribed pressure $p = 0$ at the bottom left corner. Comparison is made to works by Cruchaga and Oñate [26], Ghia [28], Tanaheshi [29] and to the monolithic solution obtained in Section 3.1.3. Here the mesh is composed by 11664 three-noded triangular elements with size $l^e = 0.0075 - 0.05$. In Figure 3.14 the vortices are visualized by plotting the direction of the velocity field and in Table 3.3 their exact positions. In Figure 3.15 horizontal and vertical cuts through the center of the domain are plotted and line variation of the velocity and pressure is visualized.

Apart from the central main vortex and two secondary vortices at the bottom corners (BR and BL), which are present in all the three examples, the flow with $Re = 5000$ has one vortex at the top left corner (TL). The flow with $Re = 10000$ also has two additional vortices at the bottom corners. However, these are not indicated in Table 3.3.

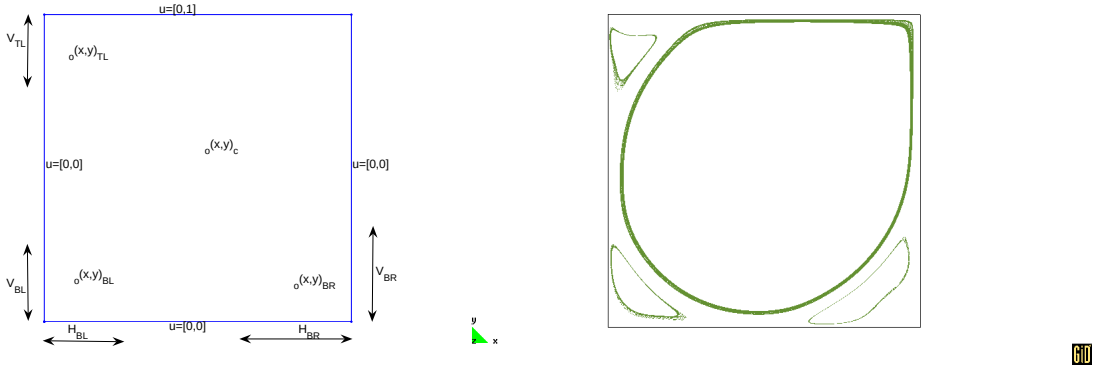

Figure 3.13: Cavity. Definition of the vortex characteristics

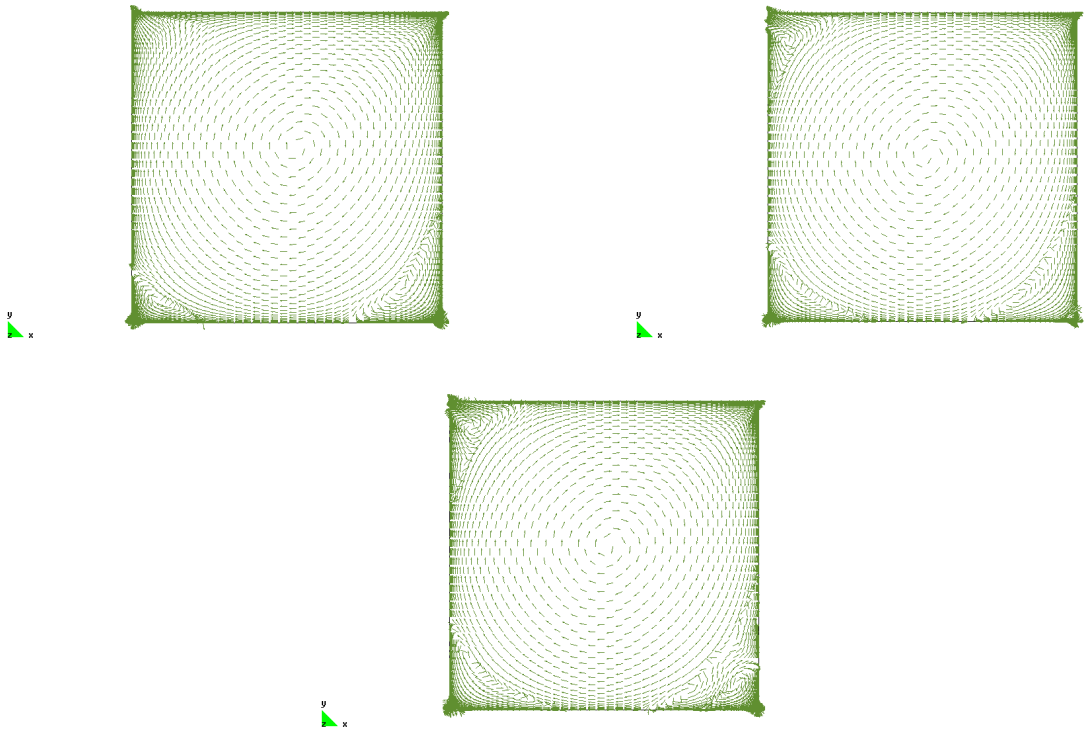

Figure 3.14: Cavity. Velociy field. Above to the left: Re =1000, above to the right: Re =5000, below: Re =10000

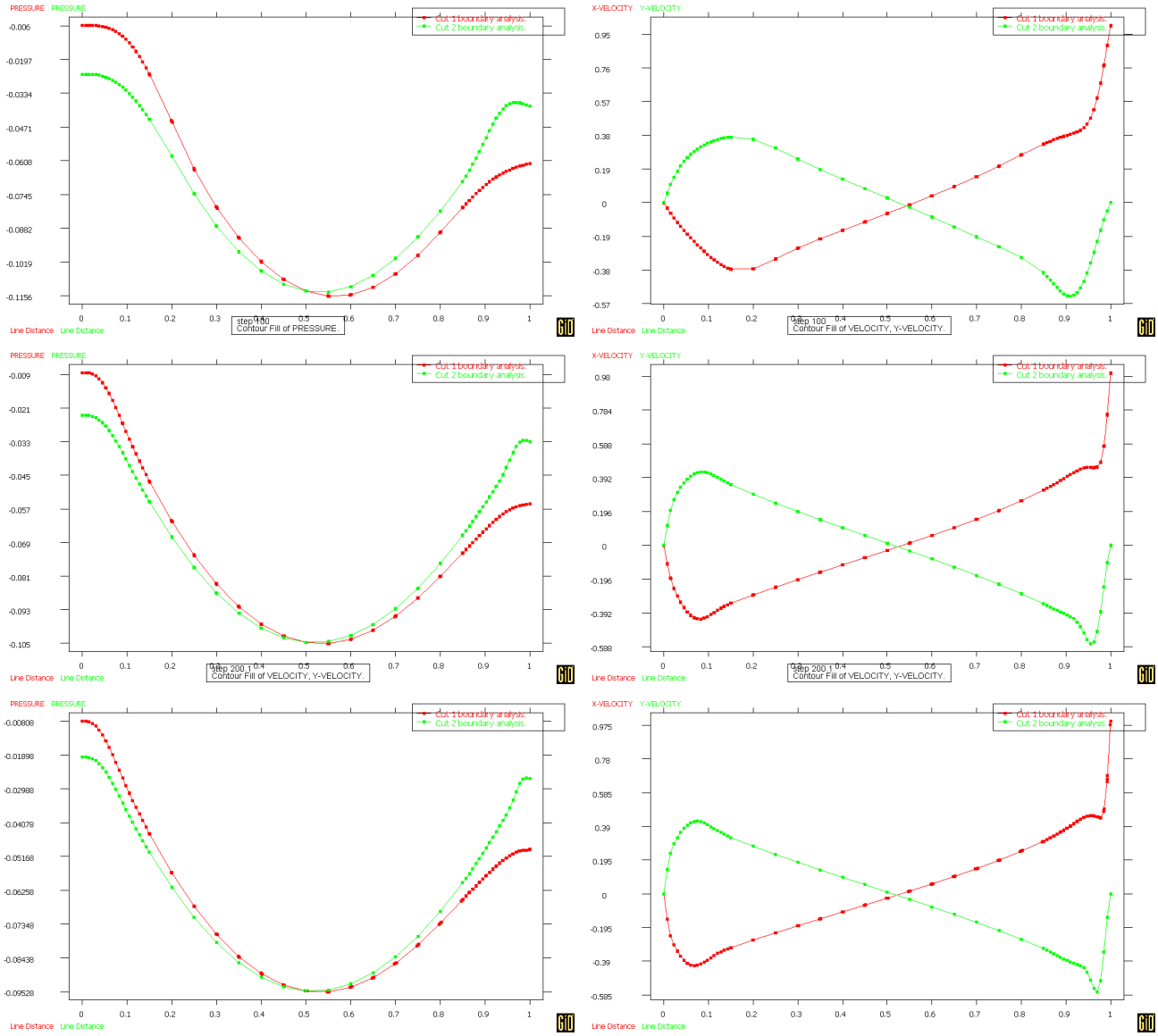

Figure 3.15: Cavity with $Re = 1000$, 5000 & 10000 (from above). Line variation of pressure and velocity component u_x at $x = 0.5$ (red curve) and u_y at $y = 0.5$ (green curve)

Table 3.3: Cavity. Vortex characteristics

	Tanahashi	Ghia	Cruchaga	FIC	FIC 3D	GLS(linear)
	Re=1000					
x_c	0.5335	0.5313	0.5409	0.531	0.530	0.530
y_c	0.5653	0.5625	0.5855	0.565	0.565	0.568
x_{BR}	0.8672	0.8594	0.8684	0.867	0.870	0.862
y_{BR}	0.1119	0.1094	0.1072	0.114	0.110	0.115
x_{BL}	0.0822	0.0859	0.0760	0.085	0.087	0.081
y_{BL}	0.0731	0.0781	0.0754	0.078	0.079	0.076
H_{BR}	0.3091	0.3034	0.3099	0.300	0.260	0.305
V_{BR}	0.3410	0.3536	0.3710	0.350	0.300	0.332
H_{BL}	0.2045	0.2188	0.2076	0.220	0.195	0.193
V_{BL}	0.1523	0.1680	0.1826	0.167	0.155	0.164
	Re=5000					
x_c	0.5120	0.5117	0.5029	0.517		
y_c	0.5337	0.5352	0.5420	0.536		
x_{BR}	0.8134	0.8086	0.8012	0.822		
y_{BR}	0.0753	0.0742	0.0638	0.078		
x_{BL}	0.0750	0.0703	0.0754	0.067		
y_{BL}	0.1318	0.1367	0.1345	0.155		
x_{TL}	0.0658	0.0625	0.0585	0.060		
y_{TL}	0.9045	0.9102	0.9130	0.909		
H_{BR}	0.3496	0.3565	0.3623	0.347		
V_{BR}	0.4350	0.4180	0.4145	0.401		
H_{BL}	0.3159	0.3184	0.2923	0.321		
V_{BL}	0.2693	0.2643	0.2840	0.264		
H_{TL}	0.1208	0.1211	0.1101	0.112		
V_{TL}	0.2555	0.2693	0.2923	0.298		
	Re=10000					
x_c	0.5125	0.5117	0.5000	0.515		
y_c	0.5274	0.5333	0.5420	0.532		
x_{BR}	0.7944	0.7656	0.7573	0.829		
y_{BR}	0.0640	0.0586	0.0551	0.080		
x_{BL}	0.0790	0.0586	0.0676	0.061		
y_{BL}	0.1400	0.1641	0.1536	0.165		
x_{TL}	0.0758	0.0703	0.0676	0.065		
y_{TL}	0.9120	0.9141	0.9130	0.911		
H_{BR}	0.3773	0.3906	0.3655	0.346		
V_{BR}	0.4529	0.4492	0.4522	0.445		
H_{BL}	0.3515	0.3438	0.3216	0.348		
V_{BL}	0.2834	0.2891	0.2899	0.298		
H_{TL}	0.1683	0.1589	0.1491	0.145		
V_{TL}	0.3463	0.3203	0.3333	0.341		

In 3D the cavity is modeled with 192000 four-noded tetrahedral elements with size $l^e = 0.05$ in a unit cube with velocity slip condition at the walls parallel with the xy-plane. In the results using Reynolds number 100 and 1000, see figure 3.16 and 3.17, no 3D effects can be seen, the solution reaches a steady-state and the velocity profiles coincide with those obtained by 2D simulation. For $Re = 100$ the position of the main vortex is $(x, y) = (0.61, 0.74)$ which coincides well with the value obtained by Donea and Huerta in [10]. For $Re = 1000$, just as in the 2D case a main vortex and two secondary vortices in the bottom right and left corners are present, see Table 3.3.

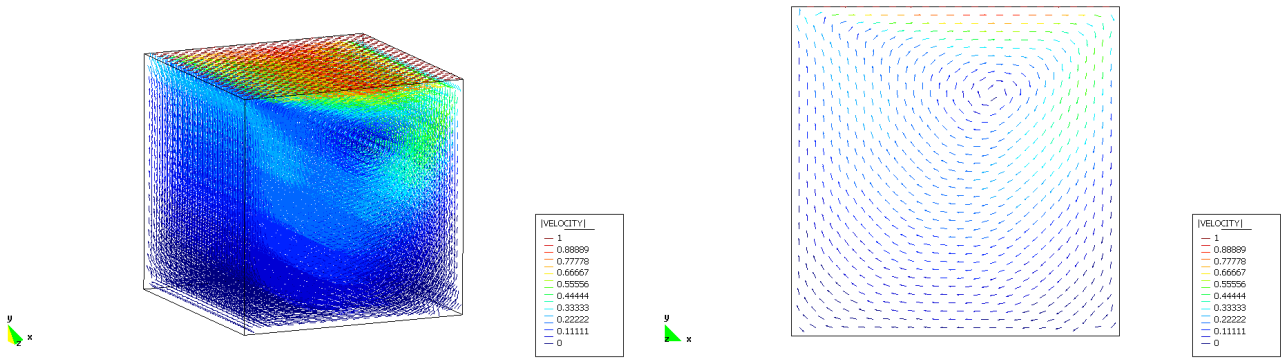

Figure 3.16: Cavity with $Re = 100$, to the left: Velocity field, to the right: cut at z=0.5

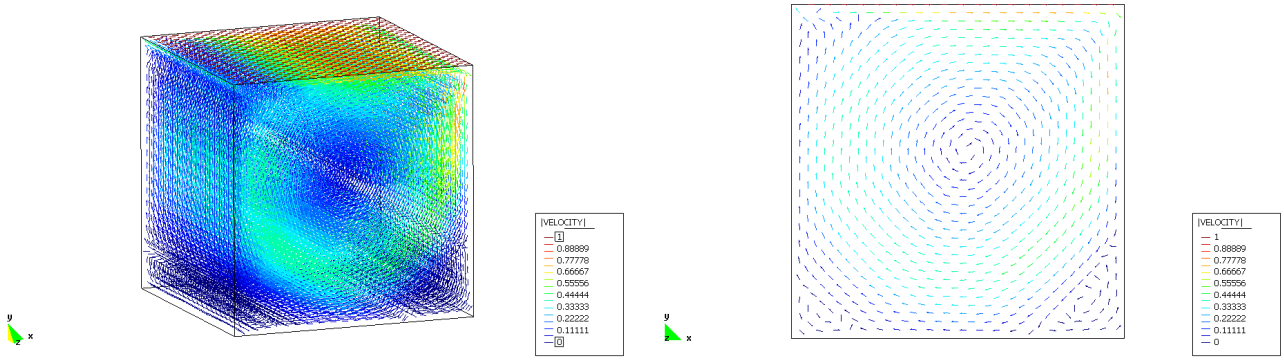

Figure 3.17: Cavity with $Re = 1000$, to the left: Velocity field, to the right: cut at z=0.5

Using Reynolds number 5000 and 10000 steady-state is not reached as fully transient flows are developed and the vortex characteristics can not be compared with the 2D results. The flow pattern at a certain time step is shown in Figures 3.18 and 3.19.

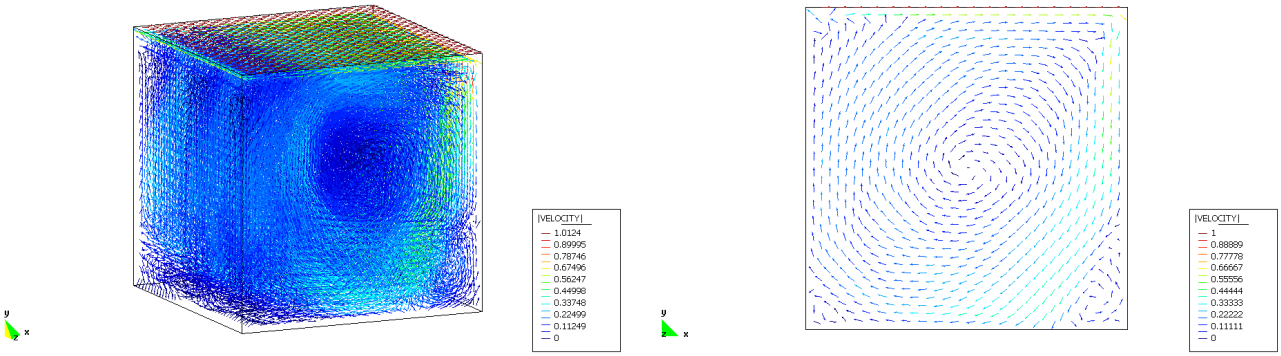

Figure 3.18: Cavity with $Re = 5000$, to the left: Velocity field, to the right: cut at z=0.5

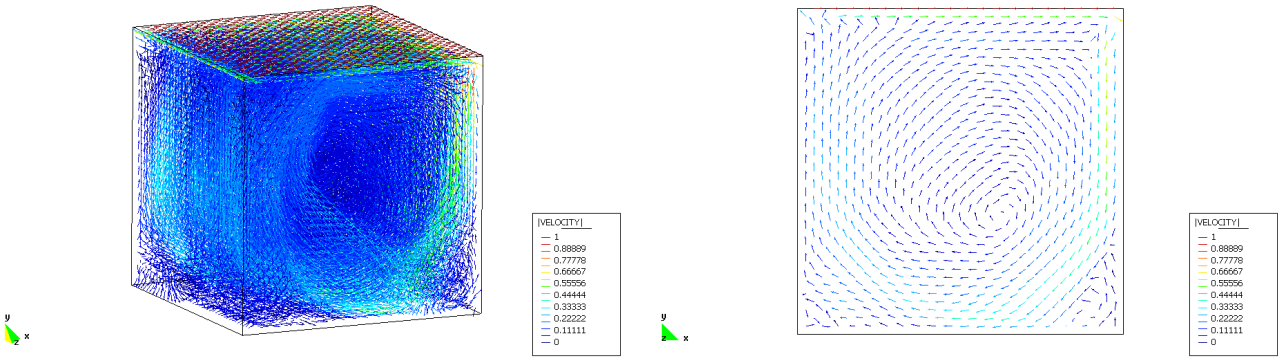

Figure 3.19: Cavity with $Re = 10000$, to the left: Velocity field, to the right: cut at z=0.5

Flow around a cylinder

Flow around a cylinder is an example which is widely used for testing and validation within computational fluid dynamics. The flow, even with relatively small Reynolds number, does not reach steady state but has a quasi-static solution. This comes from the fact that the flow separation point behind a cylinder is unsteady and changes in time causing un oscillating flow pattern downstream the cylinder with shedding vortices, often called a von Karman street. The periodic behavior of the von Karman street is quantified by the Strouhal number, named after the Czech physicist Vincenc Strouhal (1850-1922) who first investigated the steady humming or singing of telegraph wires in 1878 [32]. The Strouhal number is defined according to $S = \frac{f \cdot D}{|u|}$ where f is the shedding frequency of the vortices, D the diameter of the cylinder and $|u|$ the magnitude of the upstream velocity.

The problem setup is as follows. The geometry and the three different meshes used are shown in Figure 3.20. A unit horizontal inflow velocity is prescribed at the the left boundary, whereas at the upper and lower boundaries the velocity is free to slip. At the right boundary pressure is set to zero. Velocity is zero at the cylinder wall.

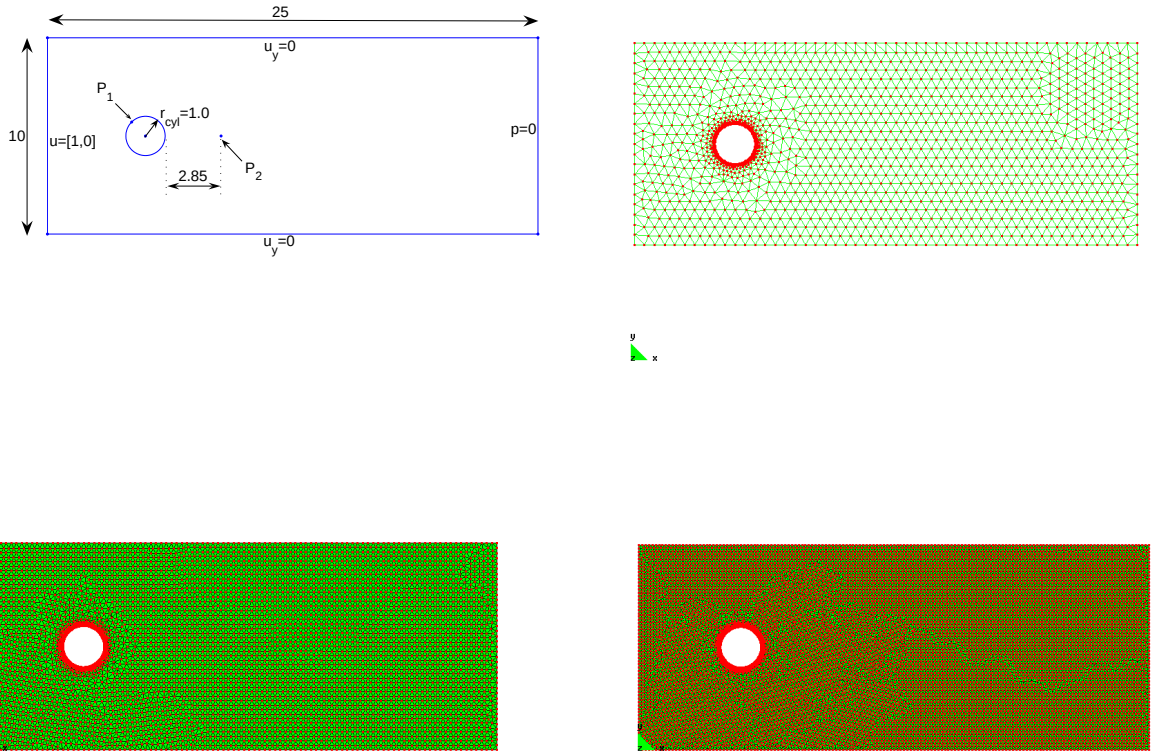

Figure 3.20: Flow around cylinder. Above to the right mesh A with 2920 elements. Below to the left mesh B with 10323 elements. Below to the right mesh C with 22129 elements

First a simulation for a flow with Reynolds number 300 is carried out. The time step is $\Delta t = 0.1$ s and in figure 3.21 the results using the three different meshes A, B and C (from above) are compared. The flow pattern is visualized at a certain time instant at the beginning of one vortex shedding period.

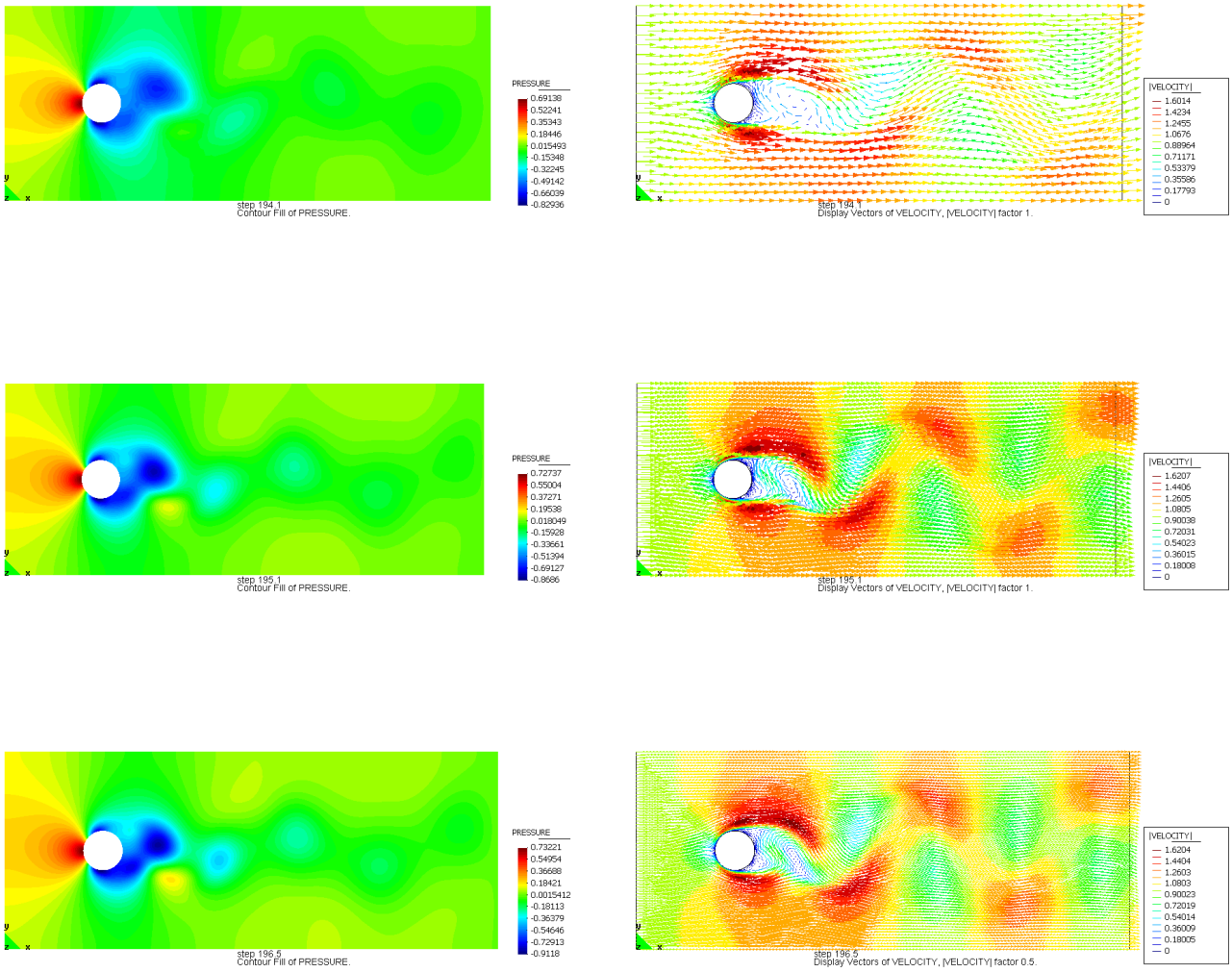

Figure 3.21: Flow around cylinder. Re =300, Mesh size 0.05-0.5, 0.025-0.25 and 0.01667-0.16667, pressure and velocity field

Below in figure 3.22 the time evolution of the pressure in the point P_1 at the cylinder wall and of the velocity in the point P_2 downstream of the cylinder are plotted. It can be seen that the mesh A is too coarse and does not capture well the flow pattern of the shedding vortices. The Strouhal number obtained for the finer grid is 0.181, see Table 3.4.

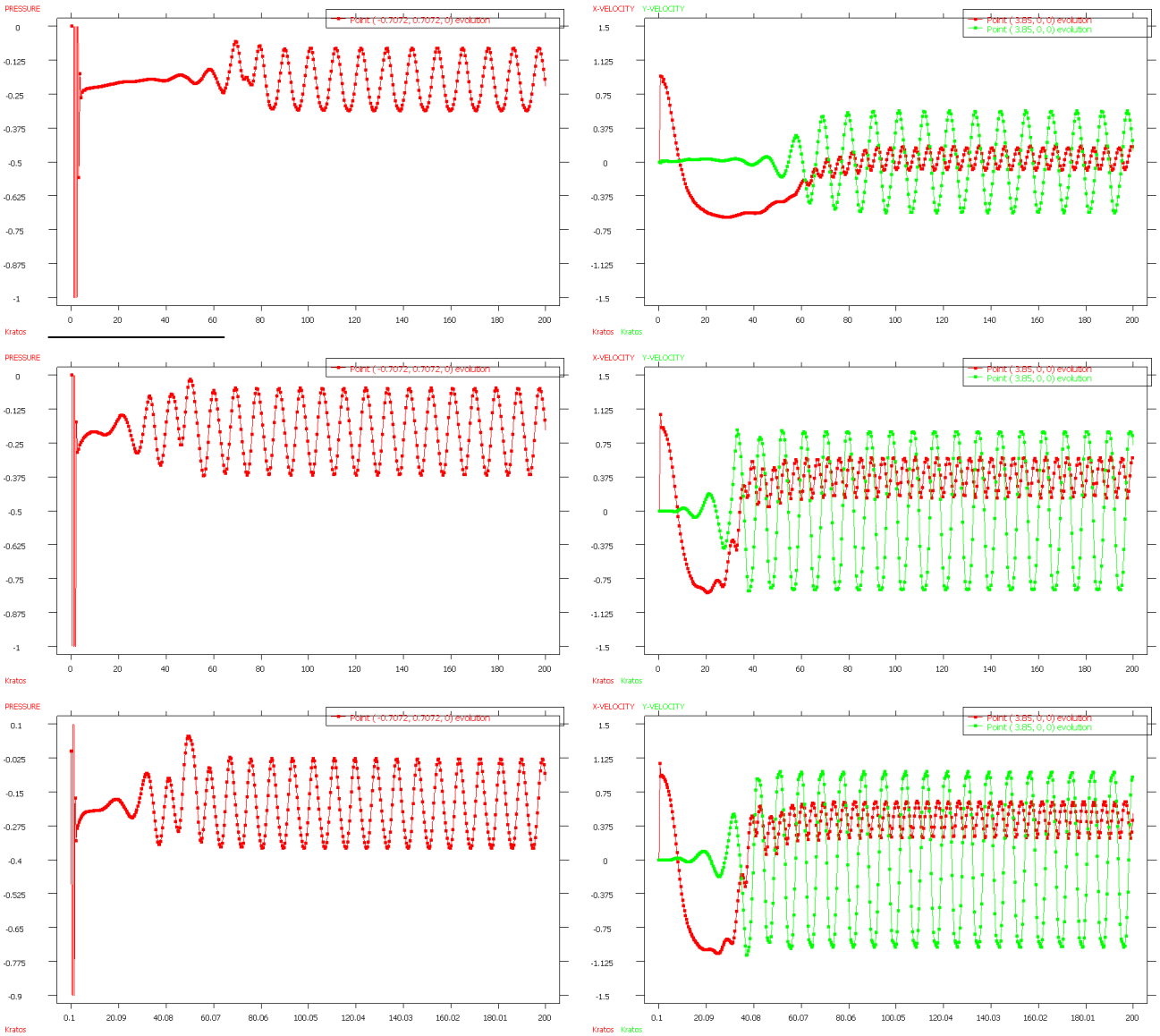

Figure 3.22: Flow around cylinder. Re =300, Mesh size 0.05-0.5, 0.025-0.25 and 0.01667-0.16667, pressure and velocity time development

Figure 3.23 shows the flow pattern of simulations using Reynolds number 2000. The same time step $\Delta t = 0.1$ s is used.

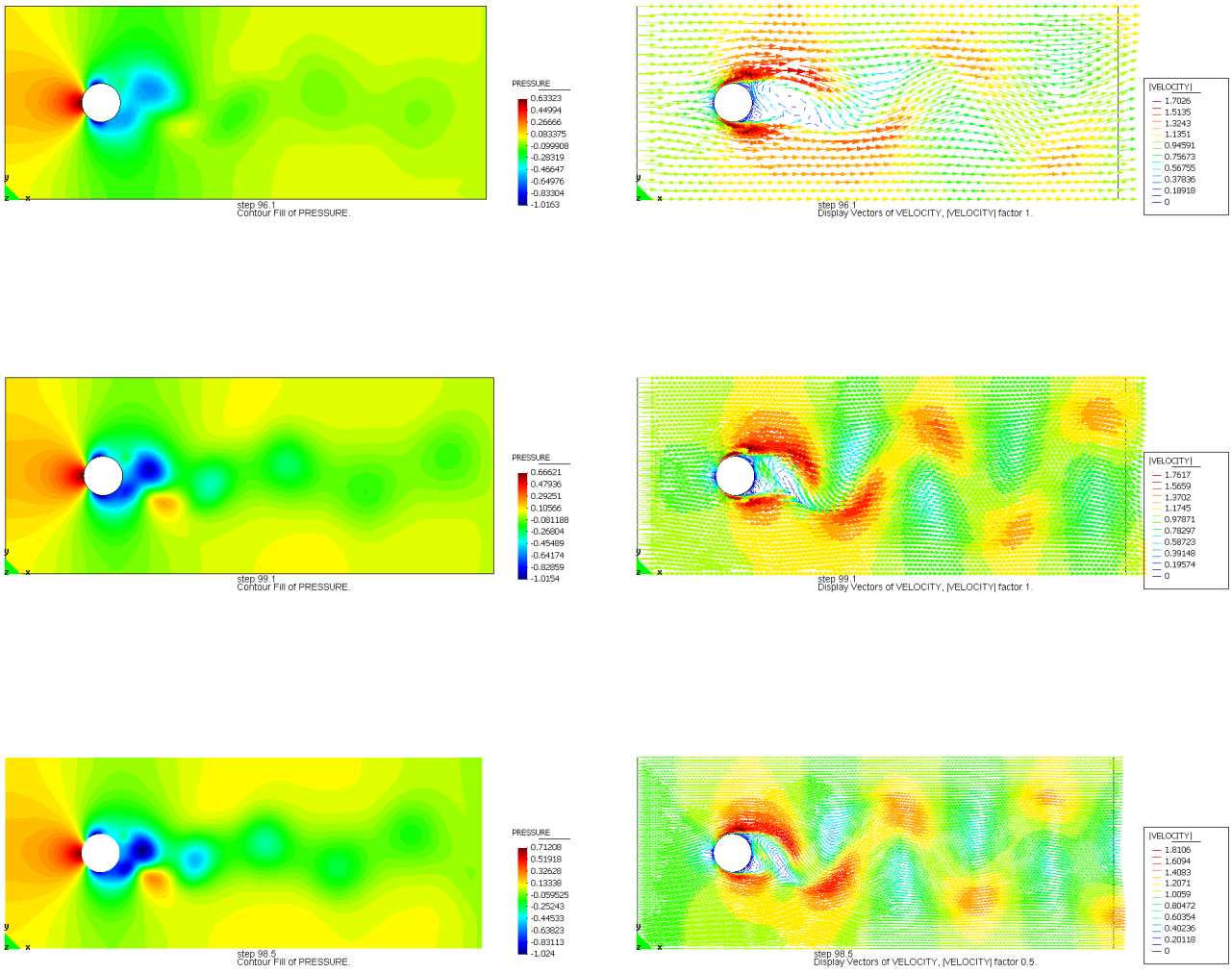

Figure 3.23: Re =2000, Mesh size 0.05-0.5, 0.025-0.25 and 0.01667-0.16667, pressure and velocity field

In figure 3.24 the pressure in P_1 and velocity in P_2 are plotted versus time. As before, comparing the outcome of the three different meshes used, it can be concluded that mesh A is too coarse. The Strouhal number is 0.192.

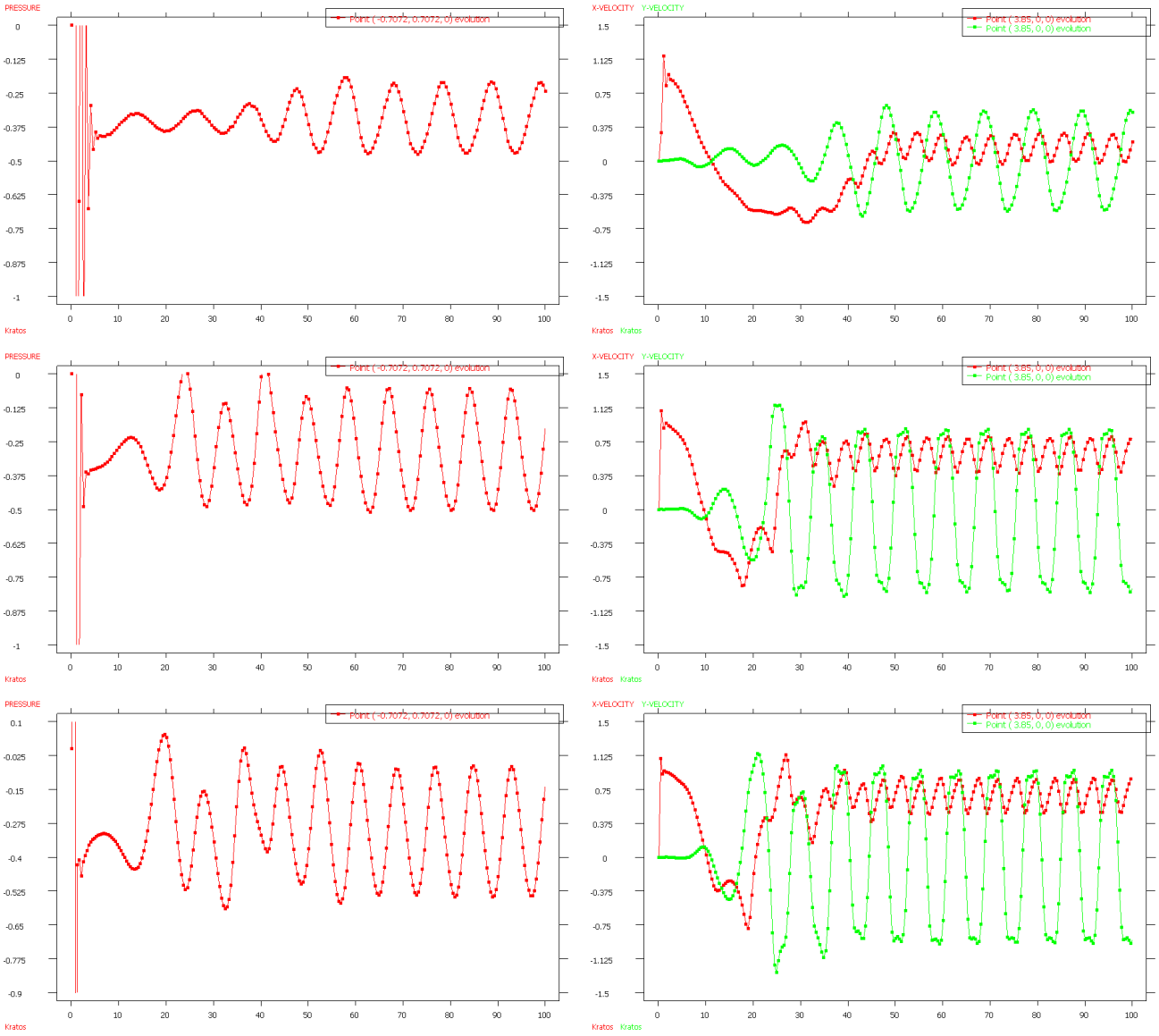

Figure 3.24: Flow around cylinder. Re =2000, Mesh size 0.05-0.5, 0.025-0.25 and 0.01667-0.16667, pressure and velocity evolution with time

For the above simulations of flow around cylinder using $Re = 300$ and $Re = 2000$ the drag and the lift forces are integrated and shown in figure 3.25.

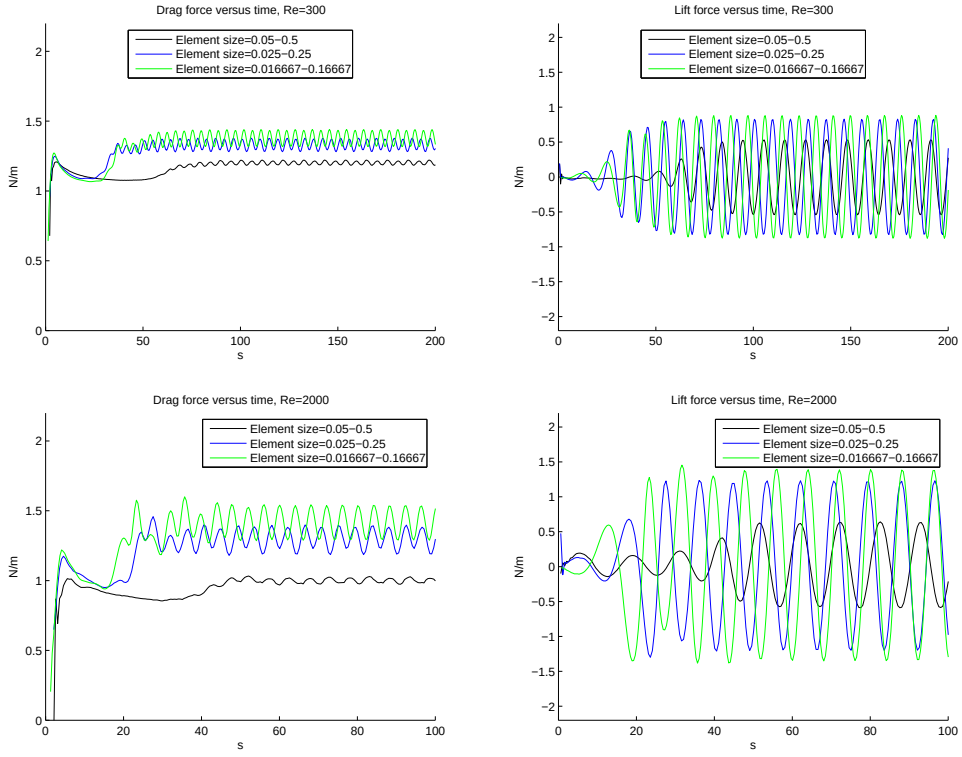

Figure 3.25: Flow around cylinder. Left: Drag force. Right: Lift force. Comparison using different mesh sizes and Reynolds number

Comparison of the computed Strouhal number is made in Table 3.4. Experimental values are taken from [33] and the monolithic values are obtained with the GLS formulation using linear elements in Section 3.1.3.

Table 3.4: Strouhal number

	$Re = 300$	$Re = 2000$
S (computed, 2D)	0.181	0.192
S (experimental)	0.202	0.208
S (monolithic, 2D)	0.19	0.20
S (computed, 3D)	0.176	0.192
S (Kalro Tezduyar [30])	0.203	-

The flow is also modeled in 3D by extending the z-axis 8 units, and the domain $\Omega : (25x10x8)$ is meshed with 300000 tetrahedral elements, see Figure 3.26. At the boundaries parallel to the xy-plane velocity slip conditions are imposed. For $Re = 300$ a von Karma vortex street is developed just as in the 2D case, but with slightly smaller Strouhal number. For $Re = 2000$ the von Karman vortex street is also present and here a certain 3D-effect is noted.

In Figure 3.27 the variation in time of the velocity components (u_x, u_y, u_z) is plotted in the point 2.85 units downstream of the cylinder, corresponding with P_2 in the 2D case.

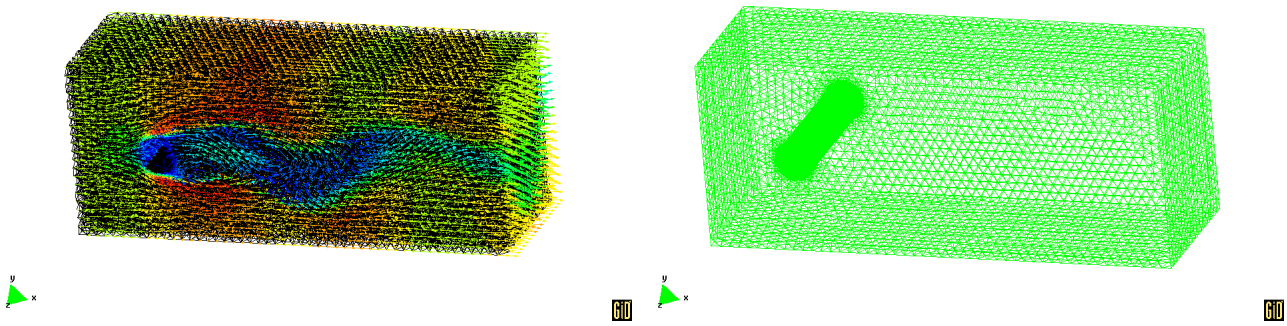

Figure 3.26: 3-dimensional flow over cylinder

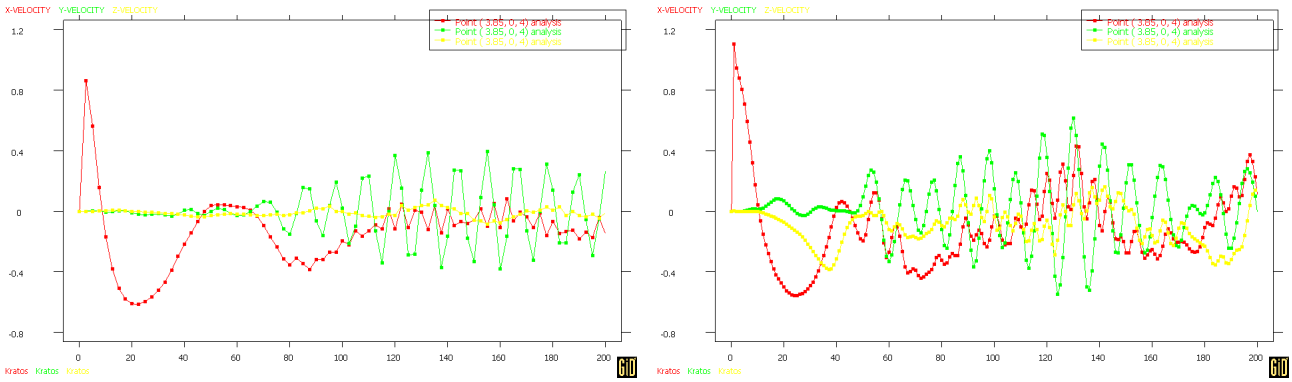

Figure 3.27: Time evolution of velocity components. left: Re =300 right: $Re = 2000$

Laminar backward-facing step flow problem

A backward-facing step flow simulation is carried out with the intention to reproduce experimental results obtained by Armaly [27]. Comparison is also made to the numerical results in Cruchaga [26]. In this case the flow is laminar and simulations with Reynolds numbers ranging from 100 to 1600 are carried out.

A fine mesh using 40000 triangular elements with size $l^e = 0.0002 - 0.001$ and a coarse mesh with 14000 elements with size $l^e = 0.0003333 - 0.001667$ are used.

Color plots of the x-component of the velocity are shown in Figure 3.29 and the reattachment length x_1/s and the position of the secondary recirculation area x_2/s and x_3/s are listed in Table 3.5. The sudden decrease in the reattachment length for $Re = 1600$ is because the flow is no longer laminar but in the transitional regime, as explained in [27].

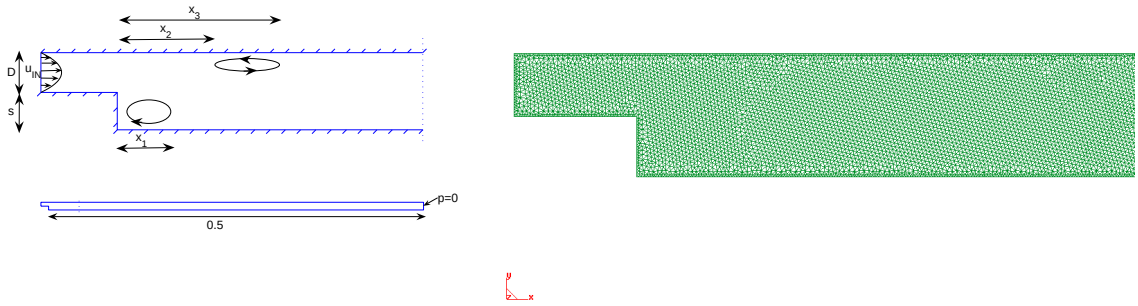

Figure 3.28: Geometry of the backward-facing step flow using the fine mesh of 40000 triangles.

Table 3.5: Backward-facing step

Re		Armaly	Cruchaga	fine mesh	coarse mesh
100	x_1/s	3.0	3.0	2.80	2.65
500	x_1/s	10.0	8.5	9.24	7.96
	x_2/s	8.0	8.0	8.59	9.24
	x_3/s	13.5	12.8	12.06	9.24
1000	x_1/s	16.25	12.93	13.04	10.49
	x_2/s	13.5	11.22	10.76	9.92
	x_3/s	21.8	22.79	22.65	16.69
1600	x_1/s	13.9	17.0	16.55	11.80
	x_2/s	9.5	14.6	13.94	11.14
	x_3/s	22.0	34.0	32.45	20.61

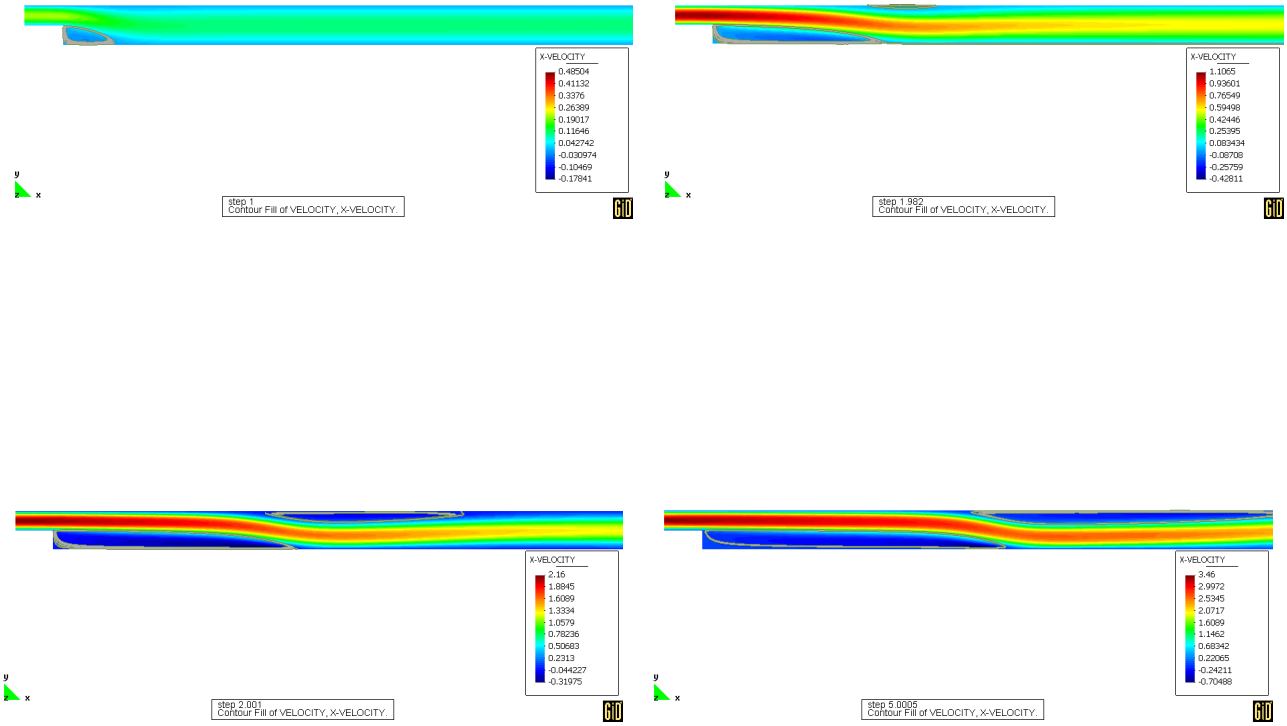

Figure 3.29: Backward-facing step flow simulations. Re =100, 500, 1000, 1600. The x-component of the velocity is plotted and streamlines indicating the vortices.

3.3.5 Turbulence

As this work partly addresses simulation of aero-elastic problems within a fluid-structure interaction framework with air flows at very high Reynolds number, turbulence will occur and needs to be properly dealt with. So far we have dealt with stabilized incompressible flows in the laminar regime at relatively low Reynolds numbers. The simulations for validating the GLS-model using linear and quadratic elements and the FIC-model using linear elements have been carried out using direct numerical simulation (DNS). It is accepted that the Navier-Stokes equations describe incompressible flows correctly also in the turbulent regime so that using DNS for turbulent flows is theoretically possible. The

drawback with DNS is however that the number of degrees of freedom needed to resolve the full-scale problem grows fast with an increasing Reynolds number according to the so-called Kolmogorov estimator, stating $\mathcal{O}(Re^{\frac{9}{4}})$. In practice this lies beyond the potential of today´s computational power and instead one has to rely on modeling of the turbulence phenomena in some way, that is regarding the effect of the the small scale on the large scale without having to calculate it exactly.

The first family of methods are the Reynolds Average Navier-Stokes (RANS) equations. The basic tool required for the derivation of the RANS equations from the instantaneous Navier-Stokes equations is the Reynolds decomposition. Reynolds decomposition refers to separation of the variables velocity u_i and pressure p into mean (time-averaged) values $\overline{u}_i,\ \overline{p}$ and fluctuating components $u_i',\ p'$.

$$u_i = \overline{u}_i + u_i'$$
$$p = \overline{p} + p'$$

By taking the average of the equations expressed with the decomposed variables and some further manipulation the time-average part of the solution $\overline{u}_i,\ \overline{p}$ can be solved. Here the fluctuating part u_i' is not solved but exists in the RANS equations in terms of so-called Reynolds stresses which account for the effect of the smaller scales on the larger ones.

Then we have the family of Large Eddy Simulations (LES). Here a filtering technique is used to separate the larger scales from the smaller scales, which remain unresolved compensating this by adding an eddy viscosity. LES is more computationally expensive than RANS simulations but can deliver more precise results and details about the turbulent flow at the desired level. Among these methods can be mentioned the Smagorinsky model, the Ladyzenskaja model and the variational multi-scale method first proposed by Hughes [22]. Using the variational multi-scale method the large scales are modeled separately from the small scales, which in turn can be split in resolved and unresolved scales. Besides treating the problem of turbulence it results in a completely stable method. Hence, there is no need to include any additional stabilizing term.

Inversely, a stabilizing method can be designed to replace the need to include an additional turbulence model. A conceptual frame for this "duality" principle between, on the one hand, stabilized numerical methods and, on the other hand, turbulence models is outlined by Valls [24] and Oñate et al. [25] using just a FIC stabilized formulation without introducing any additional turbulent viscosity terms. It is quite remarkable that the FIC formulation by itself allows the solution of a wide range of Reynolds numbers from low to high values while capturing all the features of turbulence effects.

Below are two examples where flow in the turbulent regime is simulated using the FIC formulation described in this section. The first is flow around a cylinder as already tried out for lower Reynolds numbers and secondly a backward-facing step flow simulation is carried out.

Turbulent flow around cylinder

Two simulations are carried out for the flow around a cylinder with a high Reynolds number. The geometry and boundary conditions are the same as before, see Figure 3.20. Mesh C is used in the simulations and the time step is $\Delta t = 0.05$ s. The results from the first simulation using Reynolds number 80000 is shown in Figure 3.30. The pressure and velocity is plotted as well as the drag and lift forces.

The computed Strouhal number is $S = 0.26$. This compares well with the experimental value represented in [33].

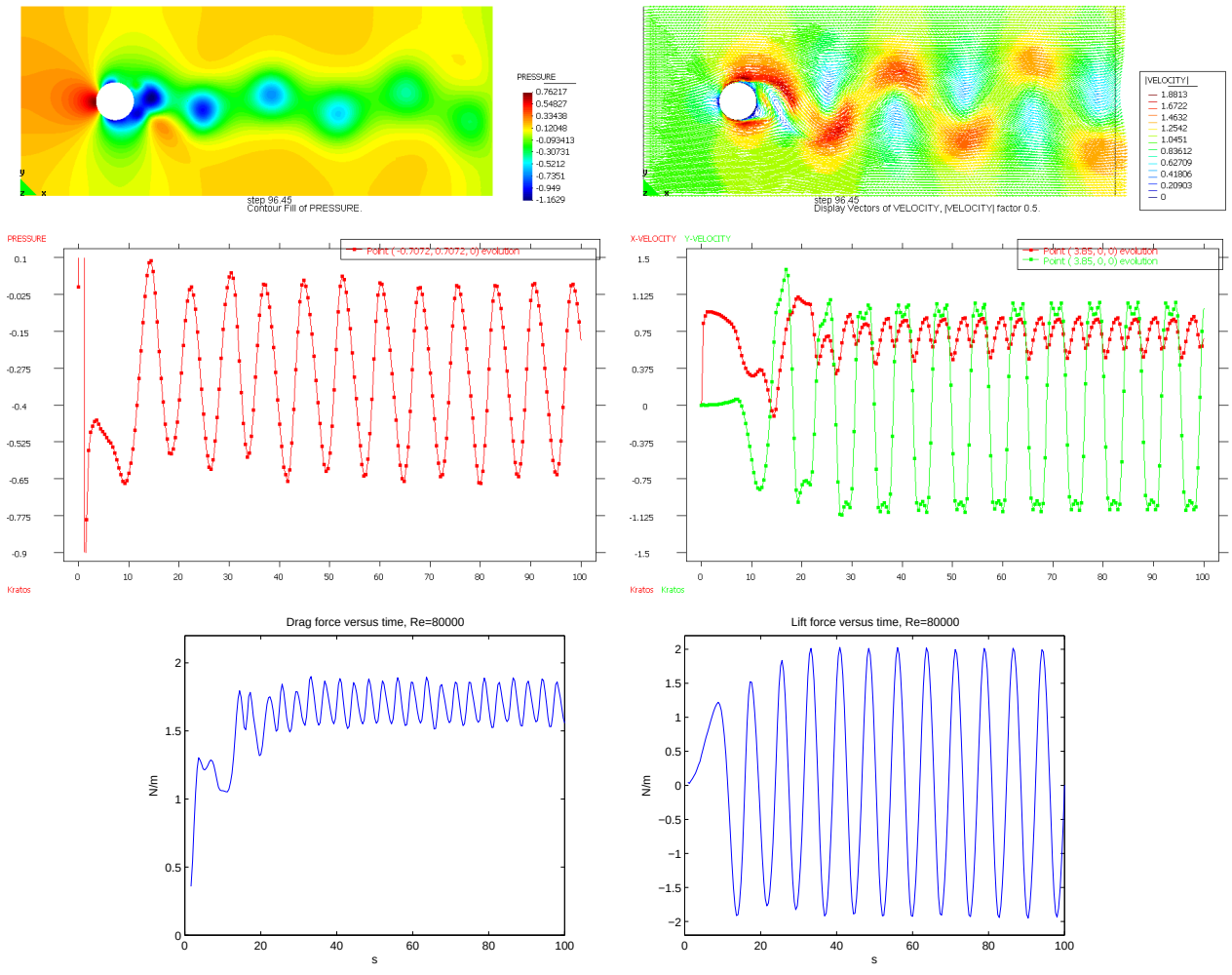

Figure 3.30: Flow around cylinder, Re =80000. From above pressure and velocity field, point evolution of pressure in point P_1 and velocity in point P_1, drag and lift forces.

In Figure 3.31 the results from the second simulation are shown. The Reynolds number is 10^6. It can be observed that they are similar to those obtained in the previous simulation using $Re = 80000$. The Strouhal number is 0.266.

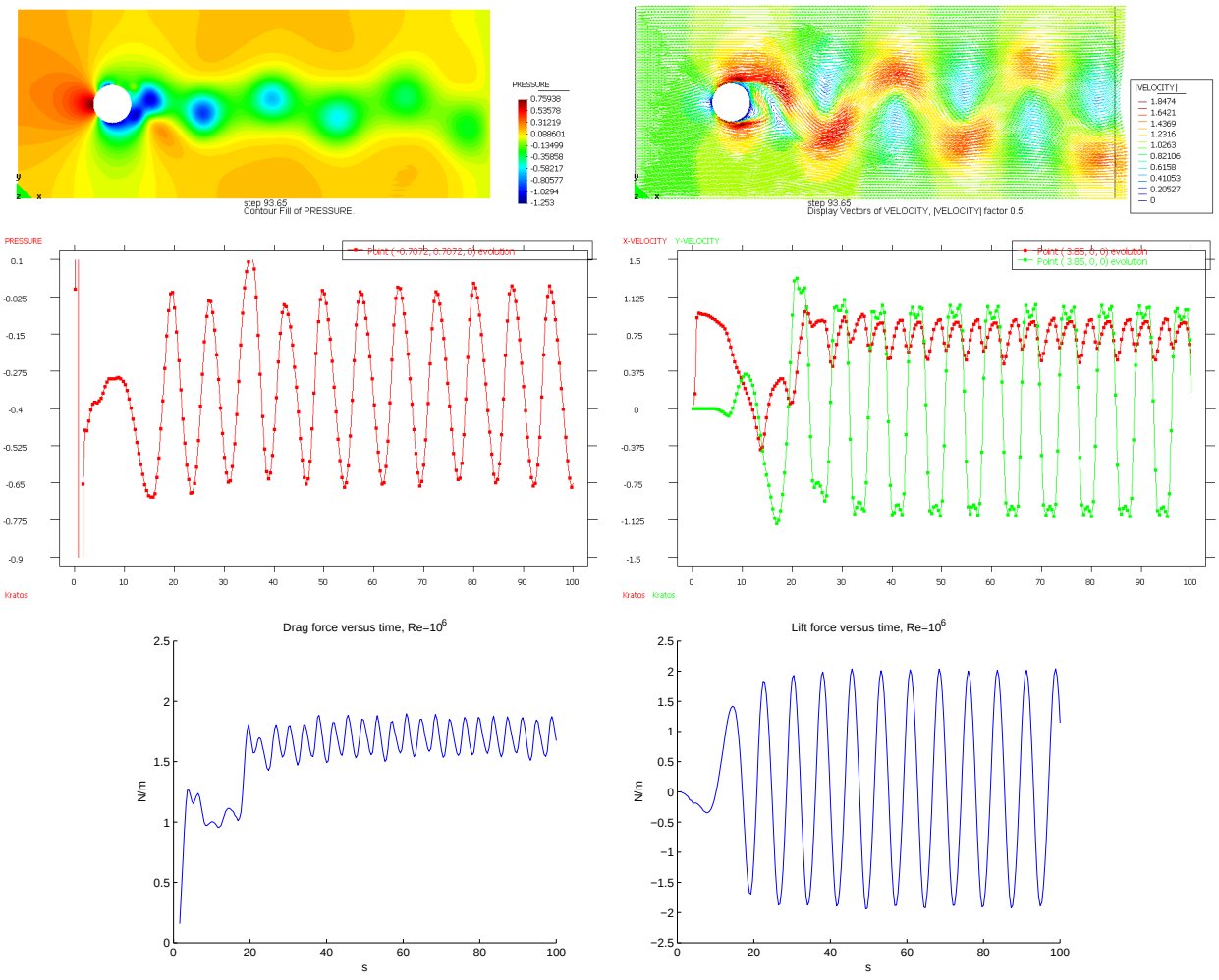

Figure 3.31: Flow around cylinder, Re =1000000. From above pressure and velocity field, point evolution of pressure in point P_1 and velocity in point P_2, drag and lift forces.

Turbulent backward-facing step flow problem

Below the backward-facing step flow simulation with Reynolds number 95000 is carried out with the following setup.

The inlet velocity is $u = [1,\ 0]$ and at the outlet boundary the pressure $p = 0$. Velocity slip conditions are assumed at the rest of the boundaries. After reaching steady-state, Figure 3.32, the length of the circulation area is $L = 5.67$. In table 3.6 comparison is made to other works where turbulence models are used.

Table 3.6: Backward-facing step, Re=95000

Model	Length(L)	Model	Length(L)
K-ϵ(Mansour)	5.2	Experimental(Kim)	6.0-7.0
K-ϵ(Pollard)	5.88	K-τ(Ilinca)	6.82
K-ϵ(Spalding)	6.0	FIC(Valls)	6.79
K-ϵ(Ilinca)	6.2	FIC(This work)	5.67

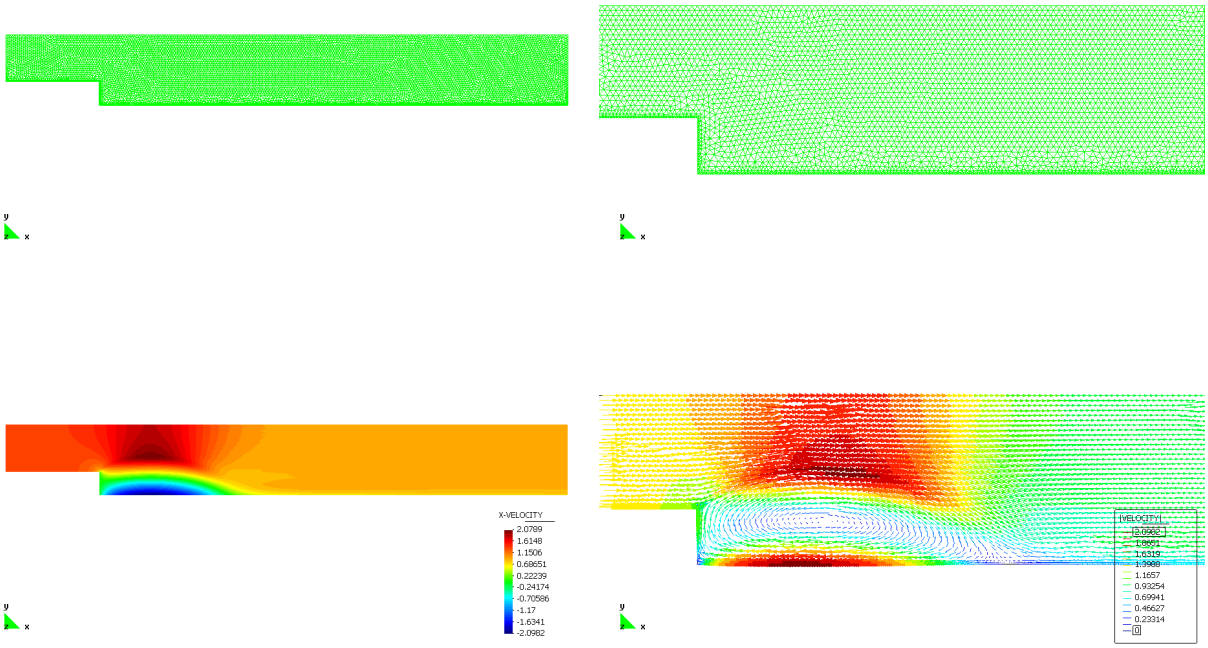

Figure 3.32: Backward-facing step using a mesh with 30262 elements. Re =95000. To the left the x-component of the velocity is plotted and to the right velocity arrays indicate the circulation area.

3.3.6 Wind simulation on telescope structure

The mechanical structure of the EURO 50 telescope not only has to support the optical elements but also, through a control system, keep the elements in exact position. This under the influence of wind, gravity and thermal effects and it must be able to rotate around two axes. The structure must be stiff enough for the displacement not to exceed the limits for the adapted control system under maximum mean wind speed during operation which is 12 m/s and to keep the lower eigenfrequencies as high as possible. Another important issue is to keep the flow pattern above the primary mirror as smooth and regular as possible, avoiding turbulence which decreases the visibility.

The main body of the telescope structure, the tube, has a parabolic shaped surface which represents the segmented primary mirror with a radius of 50 m. It can rotate around its elevation axis ranging from $\lambda = 20$ degrees to 90 where $\lambda = 90$ means the telescope tube is pointing towards zenith. A tripod structure bears the 4 m secondary mirror 46 m above the primary mirror surface. The tube is supported by the yoke structure with two bearings on which the elevation axis lies. The yoke structure in turn has 4 hydrostatic "shoes", each with 6 support points which lie on 2 circular rails where the whole structure can rotate $\varphi = \pm 270$ degrees around the azimuth axis. The telescope is protected by a concrete enclosure which also is supported on circular rails and thus rotatable. The enclosure has sliding doors in the front and on its roof which are open during observation.

In the aerodynamic simulations below a control volume of dimensions (300x450x176) m^3 surrounds the telescope and the enclosure. The inflow wind speed is 10 m/s pointing from $\varphi = 0$. The tripod structure is not regarded in these flow simulations. Velocity vertical cuts are plotted, one in wind direction and three cross wind direction at 0, 30 and 60 m from the center point, visualizing the flow pattern for different observation angles φ and λ

Among prior studies of the EURO 50 telescope in can be mentioned an eigenvalue analysis of only the structure using a finite element model with beam and shell elements which is performed in [45] where the first eigenmode refers to locked rotation around the elevation axis with $f_1 = 2.67$ Hz, the 2:nd to 6:th mode motion of the tripod structure with eigenfrequencies from $f = 4.12$ Hz until $f = 5.39$ Hz. An aerodynamic analysis carried out in [46], whose main objective was to examine the amount of wind-induced natural ventilation in the telescope building, also provides some data of the temperature distribution and the total force acting on the optical devices.

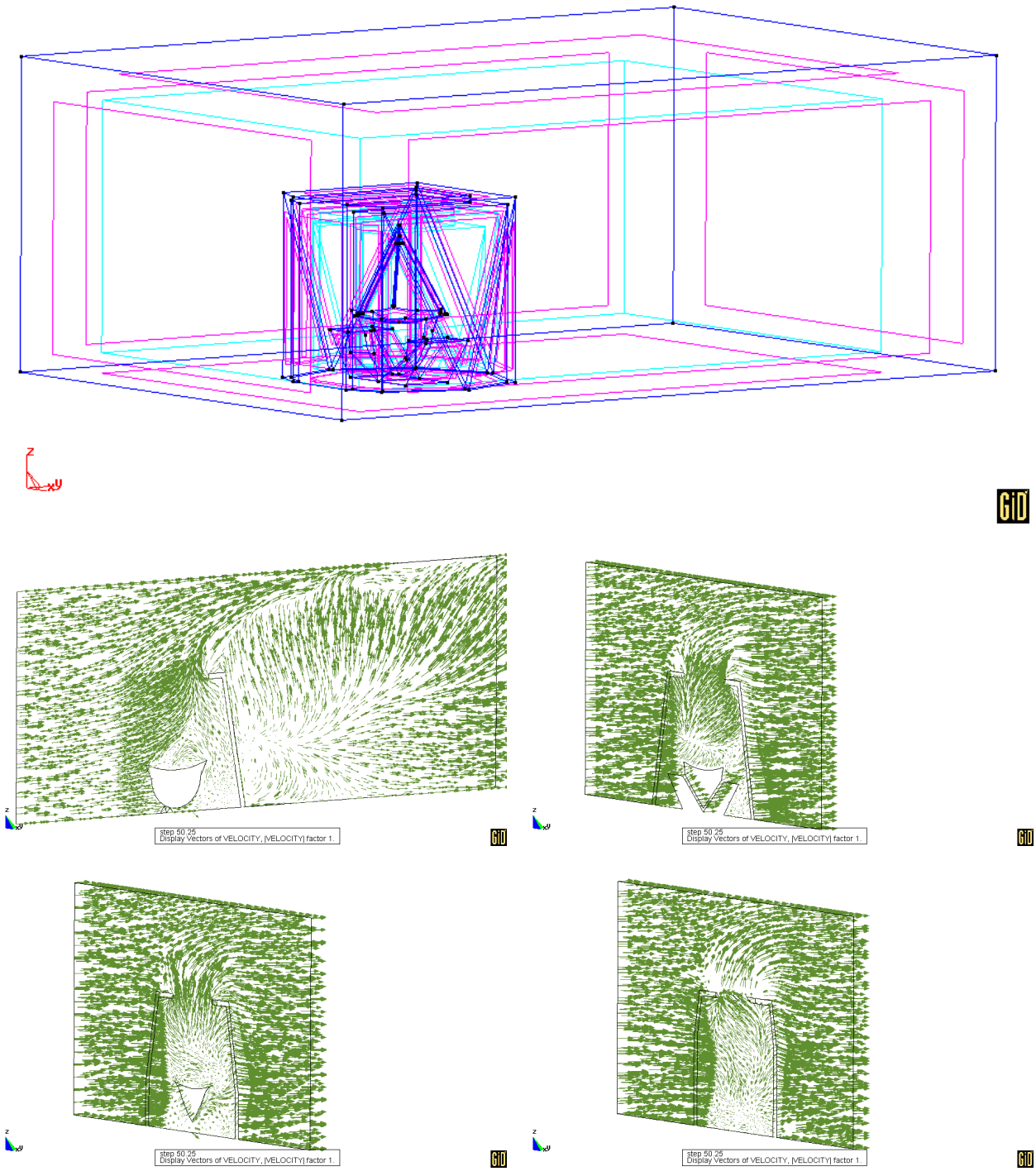

Figure 3.33: azimut angle $\varphi = 0$, elevation angle $\lambda = 90$

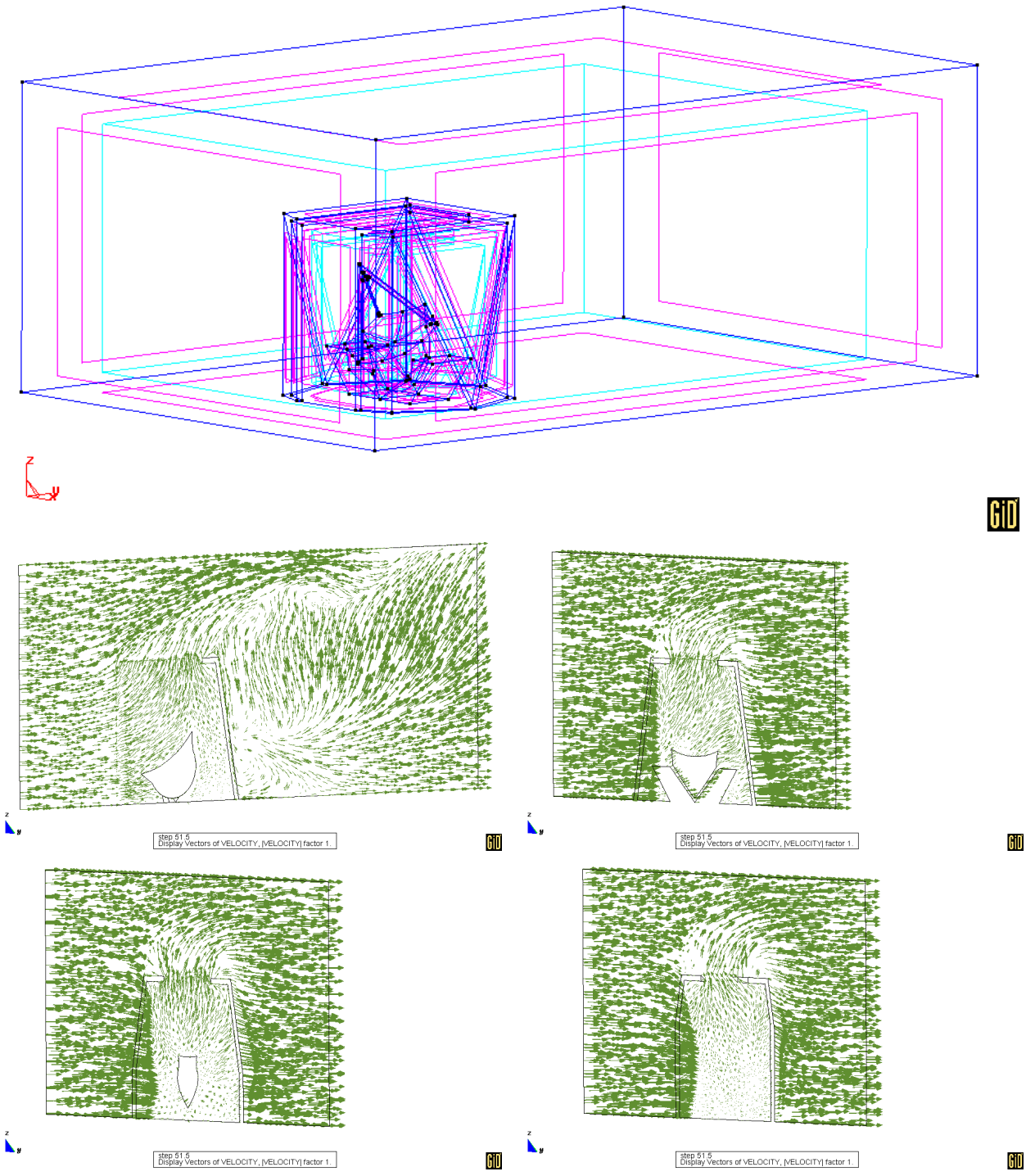

Figure 3.34: azimut angle $\varphi = 0$, elevation angle $\lambda = 60$

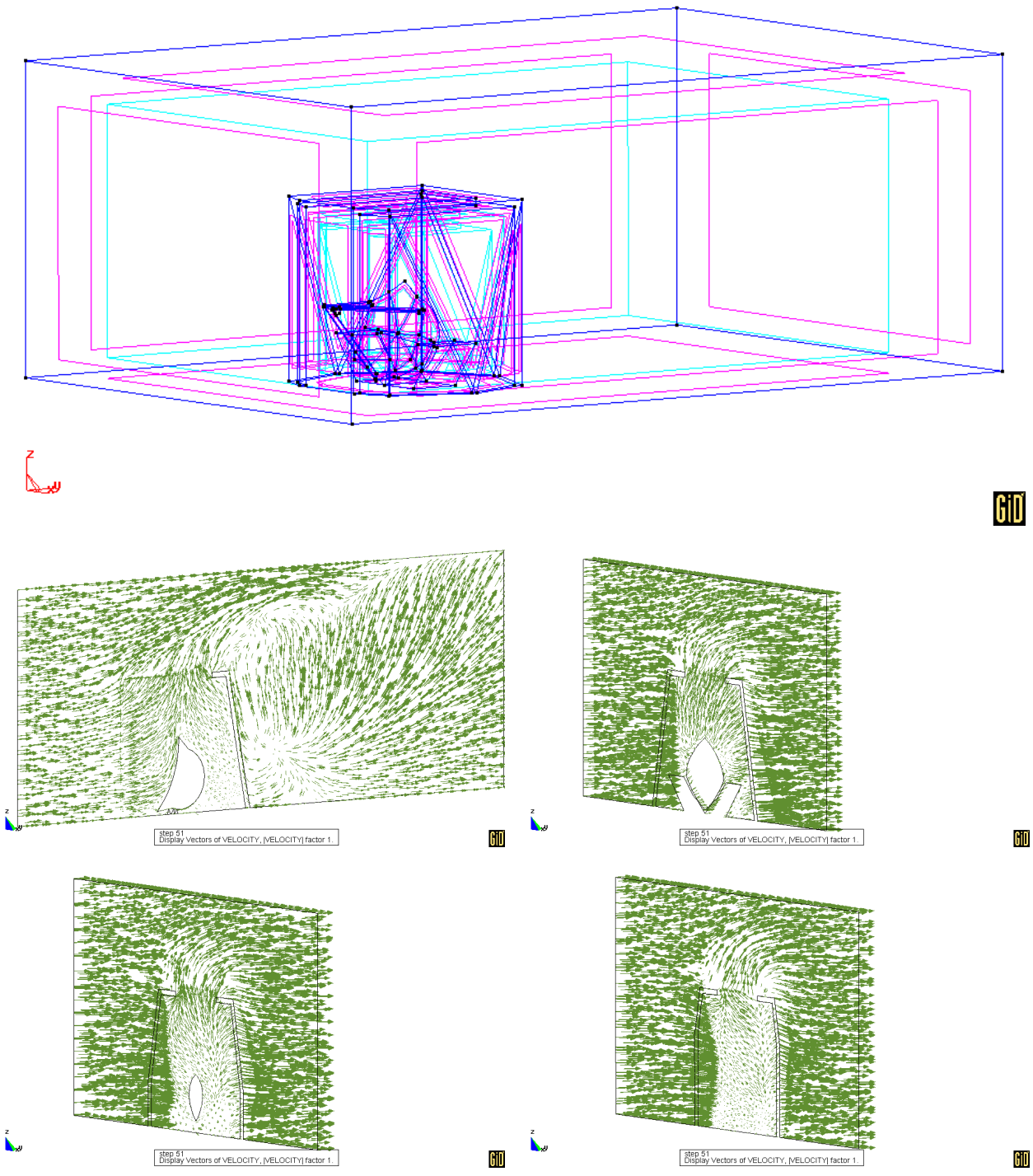

Figure 3.35: azimut angle $\varphi = 0$, elevation angle $\lambda = 20$

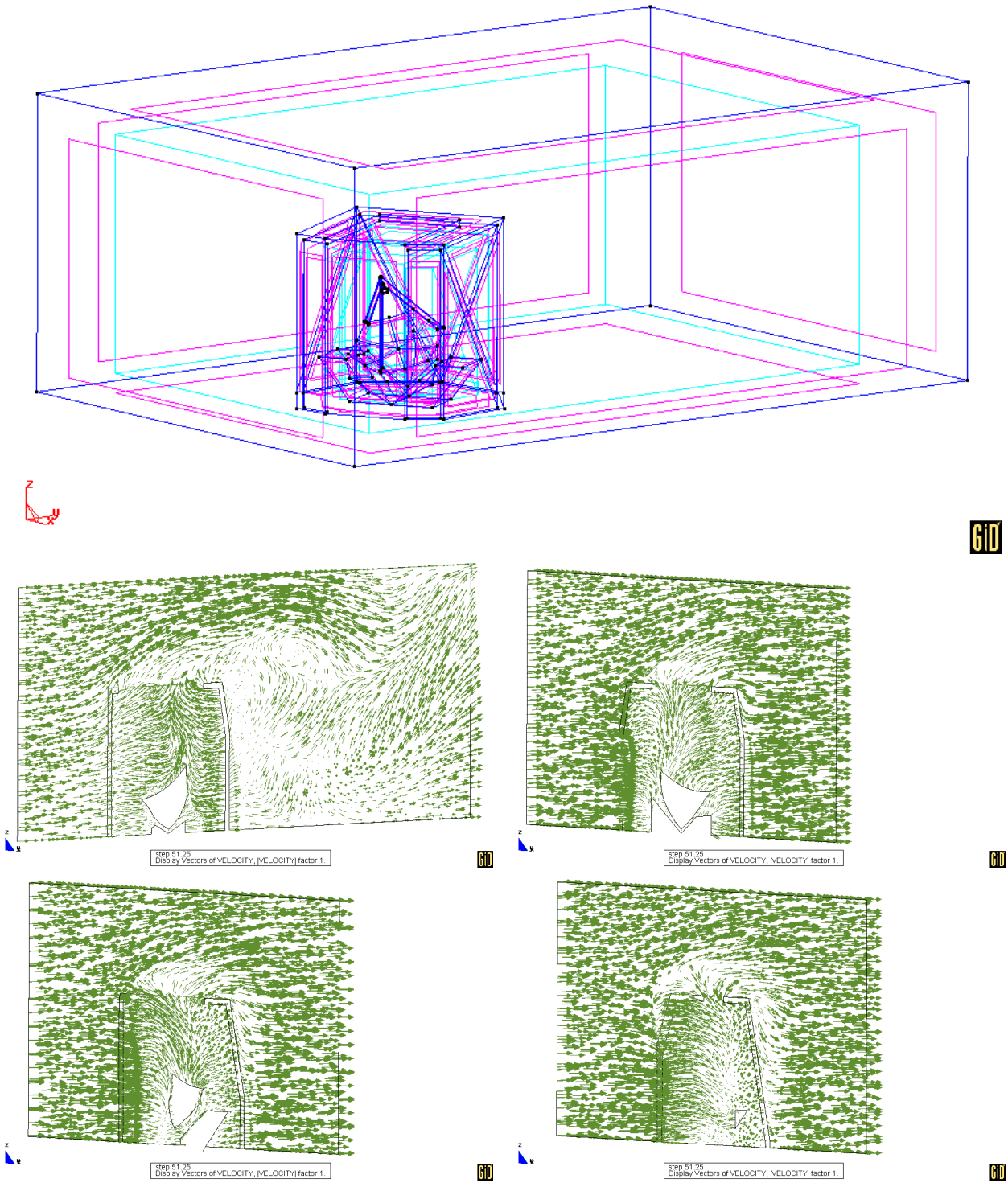

Figure 3.36: azimut angle $\varphi = 30$, elevation angle $\lambda = 60$

3.4 Concluding remarks

In this chapter, a stabilized finite element method for solving the incompressible Navier-Stokes equations have been developed. First the GLS-method is used allowing for equal order approximation of the pressure and the velocity. Linear as well as quadratic approximation is used. The GLS/FEM model allows flows in the laminar regime to be simulated which are of relatively low Reynolds numbers. Then, the equations are formulated using the FIC approach in the principle curvature directions, here approximated as the gradient. This is done in 2D and in 3D. Linear interpolation is used at the discretization. Apart from providing the necessary stabilizing effect the FIC/FEM model replaces the need for any additional turbulence model. In other words, the model can be used for simulating flows with a wide range of Reynolds numbers, for example airflows around large scale structures which typically are of high Reynolds numbers.

As the equations are written in an ALE framework and a mesh moving strategy is provided, the model applies to fluid-structure interaction problems involving aero-elasticity which is the issue in next chapter.

Chapter 4

Fluid-structure interaction

This chapter is an extension of the previous chapter where finite element methods for solving the incompressible Navier-Stokes equations were developed. The aim now is examining the ability of the FIC/FEM model to simulate fluid-structure interaction (FSI) problems with emphasis on aero-elasticity where the dynamic behavior of ground structures subjected to wind load is of interest.

FSI is a framework within computational mechanics where multi-physics problems are handled consisting of at least one fluid and one structural domain. The solution of each domain both depend on and affect the other. They are said to be coupled.

FSI has many different applications within engineering and natural sciences ranging from bioengineering such as interaction between blood flow and blood vessels, in marine engineering or aeronautics different kinds of shape optimization problems or in civil engineering. See [35] for a review of the field. These applications are often highly complex when comes to modeling point of view and therefore a wide range of rather different simulation approaches for FSI exist. A main categorization of solution strategies for FSI can be based on whether the fluid and the structure are strongly or weakly coupled.

The former is used in [36] where the complete set of nonlinear equations governing the fluid, the structure and the coupling is solved based on the Newton-Raphson methodology and incorporates the full linearization of the problem. In [37] shape optimization with respect to drag force of a flexible body in a surrounding fluid is carried out also using the strong coupling and an approximate Newton method.

Weak coupling is characterized by the presence of different solvers for the fluid and the structure and the data at the interface being transferred between the domains using so-called staggered algorithms, see e.g. [38].

Staggered algorithms in turn can be subdivided in sequential and iterative algorithms. The former, violating the kinematic condition, can lead to accuracy reduction and have the risk of numerical instabilities.

For many scientists being experts in one field and working with a single code adapted to either the fluid or the structure weak coupling is the preferable choice as it increases the flexibility in dealing with the other domain. This can be treated using a simplified model or, using code coupling, it can be modeled in another code specialized in this domain.

In [39] and in [40] iterative staggered algorithms are employed for FSI problems involving highly specialized models for nonlinear structural dynamics for thin-walled shell structures and membranes. These structural models are parts of CARAT (Computer

Aided Research Analysis Tool), the in-house code at the Chair of Structural Analysis at the Technical University of Munich. In [41] a strategy for numerical form finding of membranes is outlined.

Regarding the fluid model the governing equations, as previously mentioned, are the incompressible Navier-Stokes equations. They are formulated using the Finite Calculus (FIC) method [24]. The actual implementation is carried out within KRATOS [42], a finite element software environment for solving multi-physics problems developed at CIMNE. In Section 4.1 of this chapter the fluid solver is outlined.

Thereafter in Section 4.2 a weak and explicit coupling scheme for FSI is presented and the interface is defined where the exchange of variables in an FSI problem takes place using conforming meshes. As a first FSI application the flow induced vibration of a flexible beam is analyzed.

FSI is then applied on the Burj Dubai tower which ought to be the world´s tallest skyscraper, at the moment under construction in Dubai in the United Arab Emirates. Even though the tower has a complex shape a rather simple beam model is set up and some assumptions are made to take into account its mass and lateral stiffness and the aero-elastic behavior during wind load is simulated.

Dealing with more challenging FSI problems in the sense that sophisticated modeling within every single part of the coupled solver is required, might not be feasible within only one code. Increased computing power and tools for code coupling open up the doors for using solvers from two, or more, different codes for one problem.

For this reason an FSI application is tried out where code coupling is used. Airflow around an elastic cylinder is chosen and this is explained in Section 4.3. The cylinder is modeled in the code CARAT using shell elements. The fluid model in the code KRATOS and the structure model in CARAT are interfaced via MpCCI (Mesh-based parallel Code Coupling Interface) developed at the Fraunhofer Institute SCAI which is a program for coupling of different simulation codes. This interface work was carried out by the author of this monograph during a stay at the Technical University of Munich in collaboration with the Chair of Structural Analysis.

The results are also compared to a previous simulation with same problem set up in [40].

4.1 Fluid

The incompressible Navier-Stokes equations, which are written in an arbitrary Lagrangian-Eularian (ALE) form to account for a moving mesh, are

$$\begin{aligned}
\rho\frac{\partial u_i}{\partial t} + \rho(u_j - v_j)\frac{\partial u_i}{\partial x_j} - \mu\frac{\partial^2 u_i}{\partial x_j^2} + \frac{\partial p}{\partial x_i} - f_i = 0 \quad in\ \Omega \qquad a)\\
\frac{\partial^2 u_j}{\partial x_j^2} = 0 \quad in\ \Omega \qquad b)\\
n_j \cdot (\mu\frac{\partial u_i}{\partial x_j} - p\delta_{ij}) - \bar{t}_i = 0 \quad on\ \Gamma_N \qquad c)\\
u_i = \overline{u}_i \quad on\ \Gamma_D \qquad d)
\end{aligned} \tag{4.1}$$

4.1.1 Finite Calculus

Adapting the Finite Calculus method the equations are expressed in the principle curvature directions of the solution, according to

$$
\begin{aligned}
r'_{m_i} - \frac{1}{2} h'_{ij} \frac{\partial r'_{m_i}}{\partial \xi_j} = 0 \quad in\ \Omega \qquad a) \\
\frac{\partial u_j}{\partial x_j} - \tau \frac{\partial r_{m_j}}{\partial x_j} = 0 \quad in\ \Omega \qquad b) \\
n_j \cdot \left(\mu \frac{\partial u'_i}{\partial \xi_j} - p\delta_{ij} \right) - \overline{t}'_i + \frac{1}{2} h'_{ij} n_j \cdot r'_{m_i} = 0 \quad on\ \Gamma_N \qquad c) \\
u'_i = \overline{u}'_i \quad on\ \Gamma_D \qquad d)
\end{aligned}
\tag{4.2}
$$

The prime denotes that the principle curvature direction is taken as basis and r'_{m_i} is the residual of the momentum equation expressed in this basis.

$$
r'_{m_i} = \rho \frac{\partial u'_i}{\partial t} + \rho (u'_j - v'_j) \frac{\partial u'_i}{\partial \xi_j} - \mu \frac{\partial^2 u'_i}{\partial \xi_j^2} + \frac{\partial p}{\partial \xi_i} - f'_i
$$

Evaluating the principle curvature direction of the solution and computing the characteristic length vector h'_{ij} constitute the central part of the FIC method as already dealt with in previous chapters. It introduces the necessary additional diffusion in order to stabilize for the dominant convection term and circumvents the LBB condition allowing equal-order interpolation of velocity and pressure. Furthermore it provides the numerical scheme with intrinsic features to model flows also with high Reynolds number without any additional turbulence modeling, as already shown in [25].

After calculating h'_{ij} it is transformed back to the original coordinate system, as explained in Section 3.3.3. Projection terms are introduced, π_i for the pressure gradient and c_i for the convection term. The Galerkin procedure is carried out leading to the following weak form of the problem.

Find $u_i \epsilon \boldsymbol{S}$ and $(p,\ c_i,\ \pi_i) \epsilon \boldsymbol{Q}$ such that

$$
\begin{aligned}
\int_\Omega \left(\rho w_i \left(\frac{\partial u_i}{\partial t} + (u_j - v_j) \frac{\partial u_i}{\partial x_j} \right) + \frac{\partial w_i}{\partial x_j} \left(\mu \frac{\partial u_i}{\partial x_j} - p\delta_{ij} \right) - f_i \right) \, d\Omega - \int_{\Gamma_N} w_i \bar{t}_i \, d\Gamma + \\
\int_\Omega \rho \frac{h_{ij}}{2} \frac{\partial w_i}{\partial x_j} \left((u_j - v_j) \frac{\partial u_i}{\partial x_j} - c_i \right) \, d\Omega + \int_\Omega q \frac{\partial u_j}{\partial x_j} \, d\Omega + \int_\Omega \frac{\tau}{\rho} \frac{\partial q}{\partial x_j} \left(\frac{\partial p}{\partial x_j} - \pi_j \right) + \\
\int_\Omega \rho \zeta_i \left((u_j - v_j) \frac{\partial u_i}{\partial x_j} - c_i \right) \, d\Omega + \int_\Omega \chi_i \left(\frac{\partial p}{\partial x_i} - \pi_i \right) \, d\Omega = 0
\end{aligned}
\tag{4.3}
$$

for all $w_i \epsilon \boldsymbol{V}$ and $(q,\ \zeta_i,\ \chi_i) \epsilon \boldsymbol{Q}$

Finite element discretization in space, using linear shape functions N^a for both the velocity and the pressure as well as for the projection variables, is performed according to

$$
\begin{aligned}
u_i^h &= \sum_{a=1}^{number\ of\ nodes} N_i^a \cdot \hat{u}_i^a \\
p^h &= \sum_{a=1}^{number\ of\ nodes} N^a \cdot \hat{p}^a \\
c_i^h &= \sum_{a=1}^{number\ of\ nodes} N_i^a \cdot \hat{c}_i^a \\
\pi_i^h &= \sum_{a=1}^{number\ of\ nodes} N_i^a \cdot \hat{\pi}_i^a
\end{aligned}
$$

The finite element formulation of the problem then becomes

$$
\begin{aligned}
M \cdot \frac{\partial \hat{u}_i}{\partial t} + (A(u_j) + K + H) \cdot \hat{u}_i - G \cdot \hat{p} - C \cdot \hat{c}_i - F = 0 \\
G^T \cdot \hat{u}_j + \frac{\tau}{\rho} L \cdot \hat{p} - \frac{\tau}{\rho} Q \cdot \hat{\pi}_j = 0 \\
A(u_j) \cdot \hat{u}_i - M \cdot \hat{c}_i = 0 \\
Q^T \cdot \hat{p} - \frac{1}{\rho} M \cdot \hat{\pi}_i = 0
\end{aligned}
$$

as already derived in Section 3.3.1, see Equation (3.31) where also the matrices are defined.

For the solution a second-order fractional step method is used. The following scheme arises.

STEP 1
For each time step $n = 0..$ number of time steps
. Iterate $it = 1..$ max number of iterations or until convergence
. . For dimension $i = 1..$ number of dimensions
. . . • solve $\hat{u}_i^{*,it}$ from

$$M \cdot \frac{\hat{u}_i^{*,it} - \hat{u}_i^n}{\Delta t} + (A(u_j^{*,it-1}) + K + H) \cdot \hat{u}_i^{*,it} - G \cdot \hat{p}^n - C \cdot \hat{c}_i^n - F = 0$$

. . End For i
. End Iterate it
End For n

STEP 2
. • solve $\hat{p}^{n+1}$ from

$$G^T \cdot \hat{u}_j^* + \frac{\Delta t}{\rho} L \cdot \left(\hat{p}^{n+1} - \hat{p}^n\right) + \frac{\tau}{\rho} L \cdot \hat{p}^{n+1} - \frac{\tau}{\rho} Q \cdot \hat{\pi}_j^n = 0$$

STEP 3
. • solve $\hat{c}_i^{n+1}$ from

$$A(u_j^*) \cdot \hat{u}_i^* - M_d \cdot \hat{c}_i^{n+1} = 0$$

STEP 4
. • solve $\hat{\pi}^{n+1}$ from

$$Q^T \cdot \hat{p}^{n+1} - M_d \cdot \hat{\pi}_i^{n+1} = 0$$

STEP 5
. • solve $\hat{u}_i^{n+1}$ from

$$M_d \cdot \frac{\hat{u}_i^{n+1} - \hat{u}_i^*}{\Delta t} - G \cdot (\hat{p}^{n+1} - \hat{p}^n) = 0$$

where M_d is the lumped mass matrix.

In the fluid simulations below in which airflow is considered velocity slip boundary conditions are assumed neglecting the viscous resistance at the walls. This is implemented by projecting the fractional velocity $\hat{u}_i^{*,it}$ in step 1 and the velocity $\hat{u}_i^{n+1}$ in step 5 on the surface were the slip boundary condition is desired.

4.1.2 Mesh Moving strategy

For the evaluation of the mesh velocity v_i^n a mesh moving strategy is adapted where the displacement d_i^n in each dimension i has to fulfil the laplacian equation.

$$\frac{\partial^2 d_i^n}{\partial x_j^2} = 0 \qquad in\ \Omega_F \tag{4.4}$$

In the finite element space following equations are solved

$$\hat{L} \cdot \hat{d}_i^n = 0 \qquad in\ \Omega_F \tag{4.5}$$

where

$$\hat{L} = \int_\Omega \frac{1}{\Lambda^a} \frac{\partial N^a}{\partial x_j} \frac{\partial N^b}{\partial x_j} d\Omega \tag{4.6}$$

Here Λ^a stands for the nodal influence area (or volume in case of 3D). Division by Λ^a makes smaller elements stiffer than larger which results in the mesh being less likely of becoming inverted while moving the nodes.

When the nodal displacement $\hat{d}_i^n$ is obtained and the mesh is moved the mesh velocity at each time step n
is calculated as

$$\hat{v}_i^n = \frac{\hat{d}_i^n - \hat{d}_i^{n-1}}{\Delta t} \tag{4.7}$$

4.2 FSI Interface via KRATOS

The objective in this section is to describe how the FSI interface works. Its implementation and the computing of an FSI problem is carried out in KRATOS. For pre- and postprocessing is used GiD to which KRATOS has an interface that reads the generated input files and writes the calculated data for the fluid model part and the structure model part, respectively.

The input files contain the mesh information with the original node coordinates, its connectivity as well as material properties and boundary conditions for the fluid and the structural domain, respectively. They also contain the coupling conditions at the FSI interface.

The meshes of the fluid respectively the structure model part are made of 4-node tetrahedra (in 3D) or 3-node triangles (in 2D). The meshes are conforming with matching nodes. The coupling at the interface on the one hand consists in pairs of nodes, one from the fluid and one from the structure model part, defining where the mapping of variables from one physical domain to the other is to take place. On the other hand a boundary mesh made of triangles (in 3D) or lines (in 2D) is generated in order to calculate a weighted normal which is needed for the pressure to be applied on the structure in terms of nodal forces.

First the different steps are outlined for the computation of an FSI problem using an explicit scheme.

4.2.1 Computing scheme for fluid-structure interaction

The actual computing algorithm looks as follows:

- Set fluid model part Ω_F
- Read fluid model argument
- Get fluid mesh
  read nodes in Ω_F
  read properties in Ω_F
  read elements NavierStokesElement in Ω_F
  read face elements CalculateNormal at slip velocity boundary condition $\Gamma_{\|}$ and at FSI interface Γ_{FS}
  read conditions $\overline{u}_i, \overline{p}, \overline{d}_i$ at prescribed boundary Γ_D
- Read independent parameters
  FracStep, FSI, DomainSize, StepsBetweenPrinting, DeltaTime, EndTime
- Initialize variables in Ω_F
  Velocity, Pressure, Normal, FractVel $(u_i, p, An_i, u_i^*)^0$
  ConvProj, PressProj, NodalArea, MeshVelocity,Displacement $(c_i, \pi_i, \Lambda, v_i, d_i)^0$
- Set fluid solving strategy ResidualBasedFluidStrategy in Ω_F
- Set mesh movement solving strategy LaplacianMeshMovingStrategy in Ω_F
- Set structure model part Ω_S
- Read structure model argument
- Get structure mesh
  read nodes in Ω_S
  read properties in Ω_S
  read elements TotalLagrangianElement in Ω_S

read conditions $\overline{d}_i$ at prescribed boundary Γ_D
- Initialize variables in Ω_S
  Displacement, Velocity, Acceleration, Normal, Pressure $(d_i, u_i, a_i, An_i, p)^0$
- Set structure strategy ResidualBasedNewtonRaphsonStrategy in Ω_S
- Read coupled nodes at Γ_{FS}
- Define structure to fluid mapper at Γ_{FS}
- Define fluid to structure mapper at Γ_{FS}
- Initialize current process info (Time, DeltaTime)

While(Time<EndTime)
- Time += DeltaTime
- Set $An_i^n = 0$ in Ω_F

  Loop over fluid model part boundary elements
  - Calculate An_i^n
  - Distribute An_i^n to nodes
- Solve fluid $(u_i, p, c_i, \pi_i)^{n+1}$, auxiliary var u_i^*, Λ, input var $(v_i, An_i)^n$
- Map fluid to structure (p^{n+1}, An_i^n)
- Solve structure d_i^{n+1}, input var (p^{n+1}, An_i^n)
- Move nodes in Ω_S
- Map structure to fluid d_i^{n+1}
- Solve mesh movement $(d_i, v_i)^{n+1}$
- Move nodes in Ω_F
- Write $(u_i, p, c_i, \pi_i, d_i, v_i)^{n+1}$ in Ω_F
- Write d_i^{n+1} in Ω_S

End While

To illustrate how the FSI scheme works a 2D example is shown below in figure 4.1 with a unit square fluid domain Ω_F to the left and a unit square structure domain Ω_S to the right. For a certain time step n is plotted the weighted normal An_i^n at Γ_{FS}, the velocity u_i^{n+1} and the pressure p^{n+1} in Ω_F and finally the displacement d_i^{n+1} in both Ω_S and Ω_F using the deformed mesh.

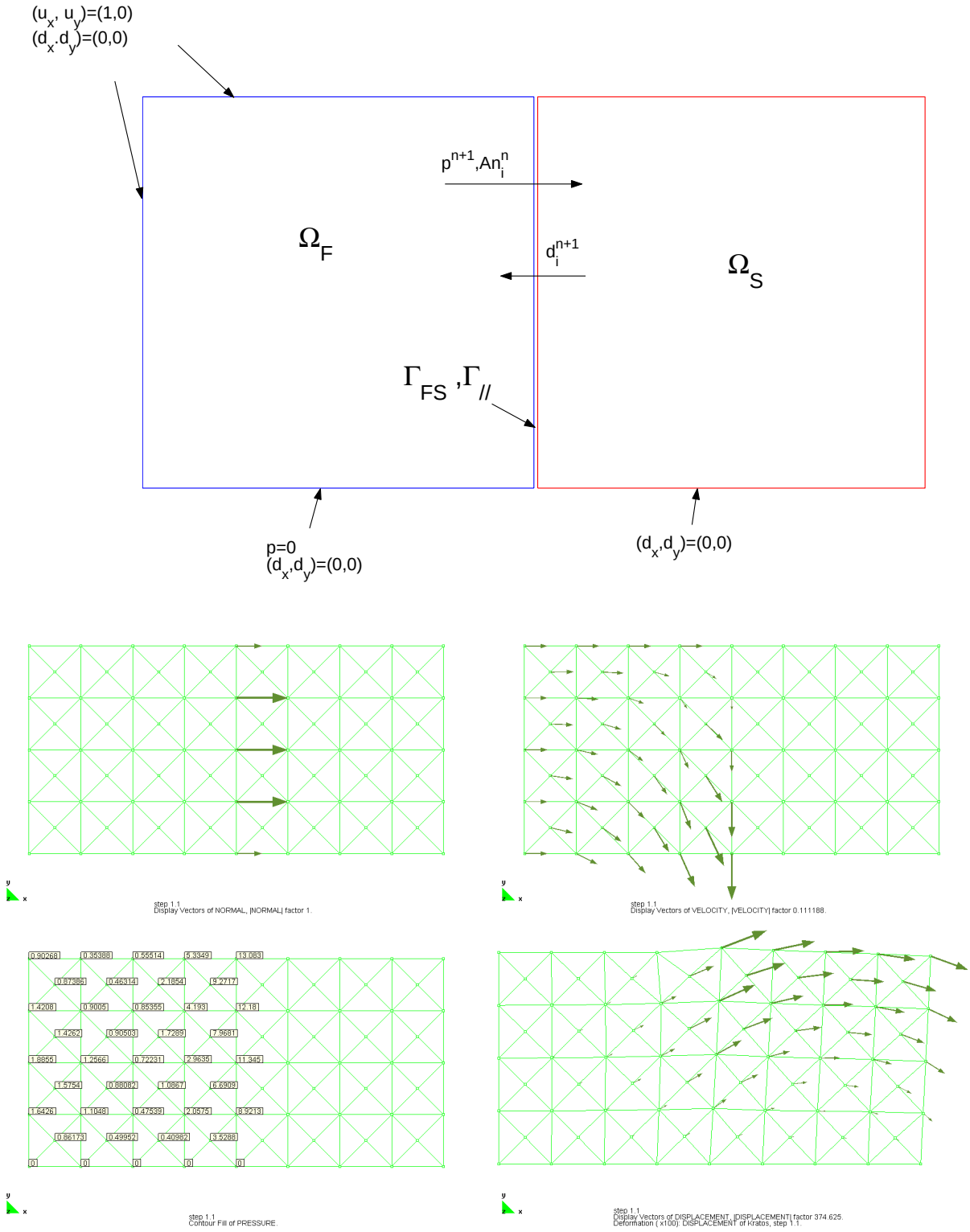

Figure 4.1: Above: conditions Top left: weighted normal, Top right: velocity field Bottom left: pressure, Bottom right: displacement field on deformed mesh

4.2.2 Flow-induced vibration of flexible beam

As a first application for trying out the FSI model is chosen a flow around a rigid unit square that induces vibration of an elastic beam which is attached downstream of the square. The geometry is taken from [36].

The problem setup is as follows. The beam is modeled by 2400 triangular total Lagrangian elements and has the following properties. Density $\rho_s = 1$ kg/m^3, Young´s modulus $E = 5 \cdot 10^6$ N/m^2, Poisson´s ratio $\nu = 0.35$. The nonlinear structural equations are linearized according to Newton-Raphson and solved with a Newmark scheme. The fluid domain is meshed with 7000 triangular incompressible Navier-Stokes elements with the properties $\mu = 0.000182$ kg/(m·s), $\rho_f = 0.00118$ kg/m^3. The inflow velocity is $u = 51.3$ m/s giving a Reynolds number of 333, no-slip conditions are set at the structure surface whereas at the lower and upper boundary the velocity is free to slip. The pressure is zero at the outflow. Employing the weak FSI coupling scheme described above a simulation is carried out using time step $\Delta t = 0.01$ s.

The flow invokes movement of the beam and it starts swinging with a frequency of $f = 1.12$ Hz, close to the first eigenfrequency of the beam, which is $f_1 = 1.37$ Hz. Below is plotted the pressure field on the deformed model at time instants $t = 5.51$ s and $t = 5.95$ s. In figure 4.3 to the left is shown the velocity component u_y versus time downstream of the structure which oscillates with the shedding frequency $f_s = 4.65$ Hz. To the right is plotted u_y at a point just upstream of the square. Here both the shedding frequency and the frequency of the swinging beam is present. Figure 4.4 shows the vertical displacement of the tip of the structure. The amplitude of this movement is 1.4 m which coincides with the one obtained in [36]. However, a just comparison with this work can not be done as the structure in [36] is lighter, $\rho_s = 0.1$ kg/m^2. This value of ρ_s could not be used in the current simulation as the ratio $\frac{\rho_s}{\rho_f}$ would be to small and the solution blow up. This is a drawback of the FSI scheme being explicit and violating the kinematic conditions at the interface.

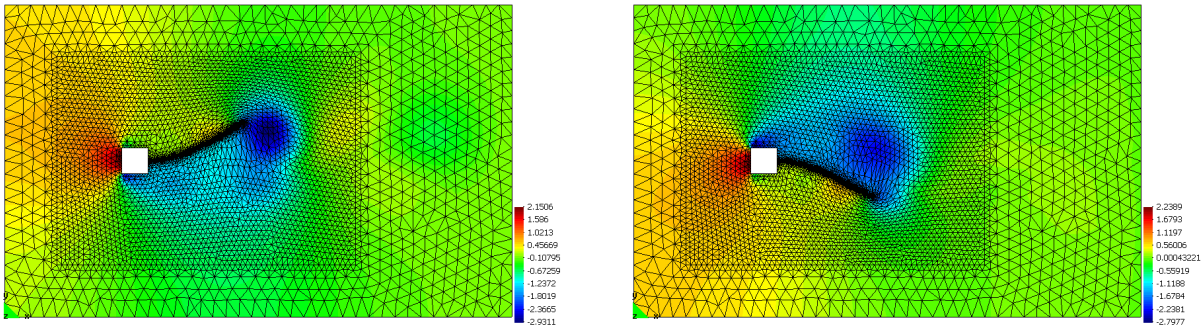

Figure 4.2: Flow induced vibration of a flexible beam: Pressure fields on the deformed model

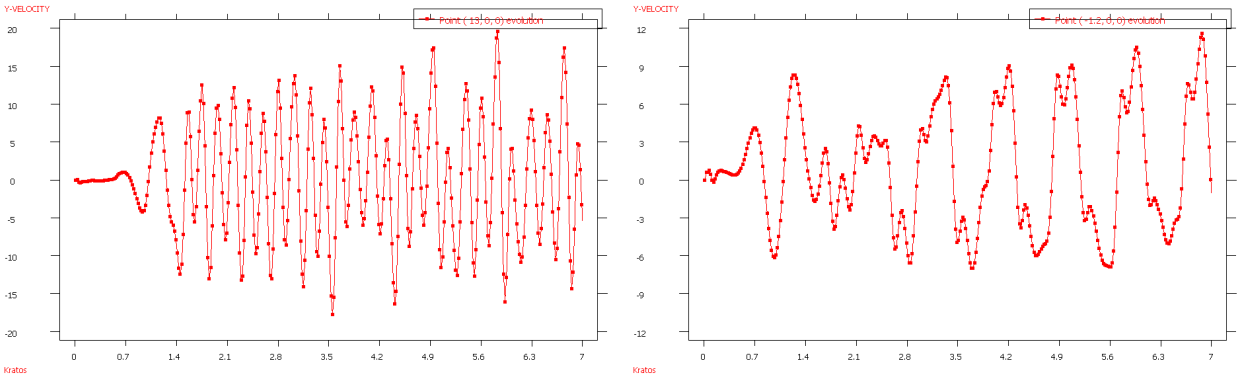

Figure 4.3: Flow induced vibration of a flexible beam: Vertical component of velocity versus time

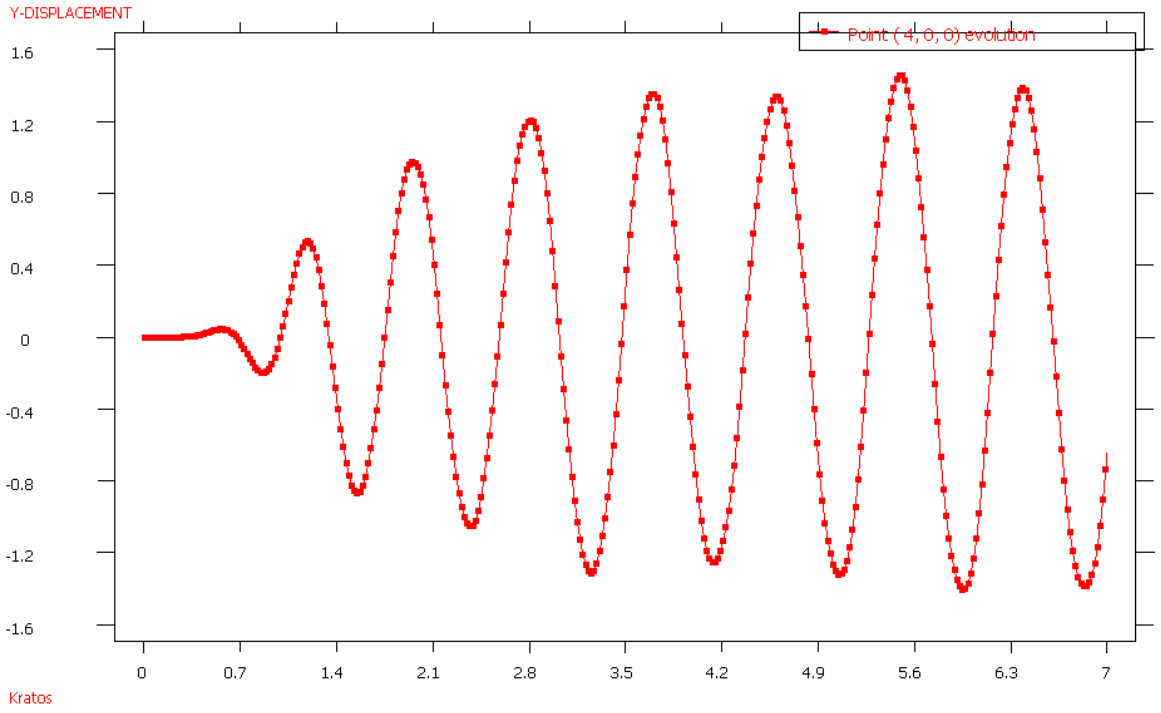

Figure 4.4: Flow induced vibration of a flexible beam: Vertical displacement of the tip of the structure versus time

4.2.3 Application to the Burj Dubai tower

The structure chosen for performing an aero-elastic analysis using the presented FSI approach is the skyscraper Burj Dubai. This building is under construction in Dubai, the United Arab Emirates.

The exact design and geometry of the tower is at the moment secret, including its total height, and no blueprints are to be obtained. The information about its total height vary between 705 and 808 m. In the FSI simulations below the height is set to 750 m and cross-section plans which are to be found on the official website of the project are used. The tower is placed in an air volume of dimensions (800x400x800) m^3 as visualized in Figure 4.5. The inflow velocity is set to moderate 10 m/s. This is of course is far below the velocities for which the tower has to be designed for, but there are no intentions in this work of penetrating design matters. Just an FSI model is tried out. Velocity slip conditions are adapted on the walls and the pressure at the outflow is set to zero.

The tower in itself is modeled as a 750 m vertical column made out of 5 m beam elements of varying bending stiffness $k[\mathrm{Nm}^2]$ around two axes and distributed mass $m[\mathrm{kg/m}]$. The stiffness is estimated assuming the outer walls taking all bending moment like a tube structure where the perimeter has a stiffness per unit length of $2.94\dot{1}0^9\mathrm{N/m}$. This corresponds to steel columns with cross-section $139\mathrm{cm}^2$ placed each meter round the circumference, which was the case for the World Trade Center (WTC) towers. The distributed mass is estimated assuming a dead load of 1 ton/m^2 floor surface. This value also originates from the WTC towers. No damping is assumed.

Torsion and vertical displacement are neglected so the structure model has 4 degrees of freedom, 2 displacement and 2 rotations, at each node of the 150 beam elements discretizing the beam length.

As the structure nodes do not coincide with the fluid nodes at the building surface the meshes are said to be non-conforming, in contrast to the described FSI-algorithm in previous section 4.2.1. An interpolation procedure is usually adapted in order to exchange the variables correctly between the domains at the interface for non-conforming meshes. This is dealt with in next section 4.3. However, in this application, for each fluid node at the interface a search algorithm is performed for the closest structure node which then is taken as the coupled node. Here the exchange of variables takes place: pressure p and weighted normal An_i in the fluid-structure direction and displacement d_i in the structure-fluid direction.

A simulation is performed during 500 s with $\Delta t = 0.2$ s. In Figure 4.7 the pressure and the displacement are plotted at time $t = 272.2$ s. In Figure 4.8 the top displacement versus time is shown. The maximal displacement of the top point during the simulation is 0.49 m, the mean displacement 0.244 m and it sways in the first mode with a frequency of $f = 0.031$ Hz.

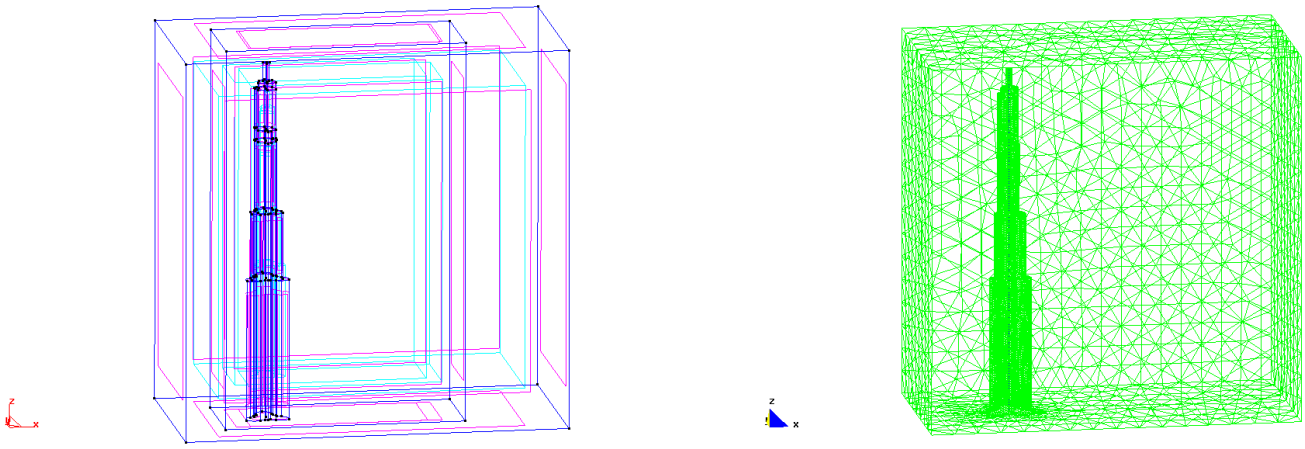

Figure 4.5: Model of Burj Dubai tower

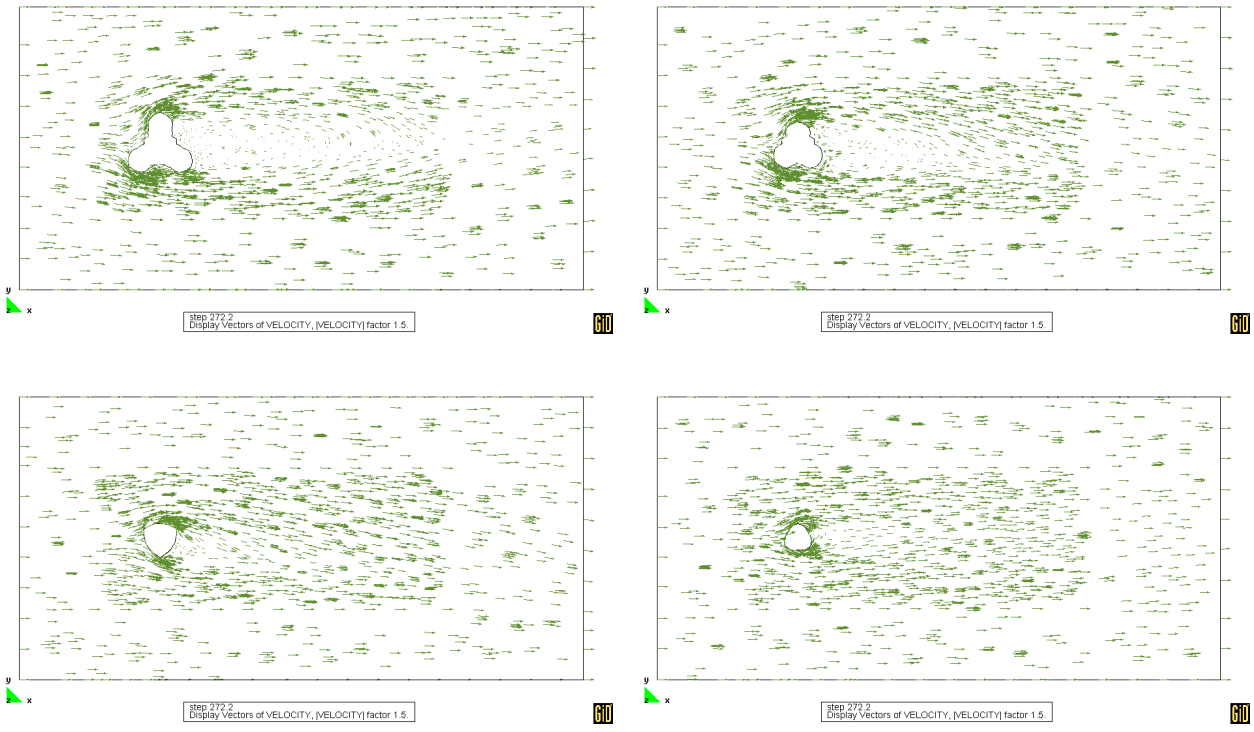

Figure 4.6: Velocity profiles at heights 100, 300, 500 and 700 m at time 272.2 s

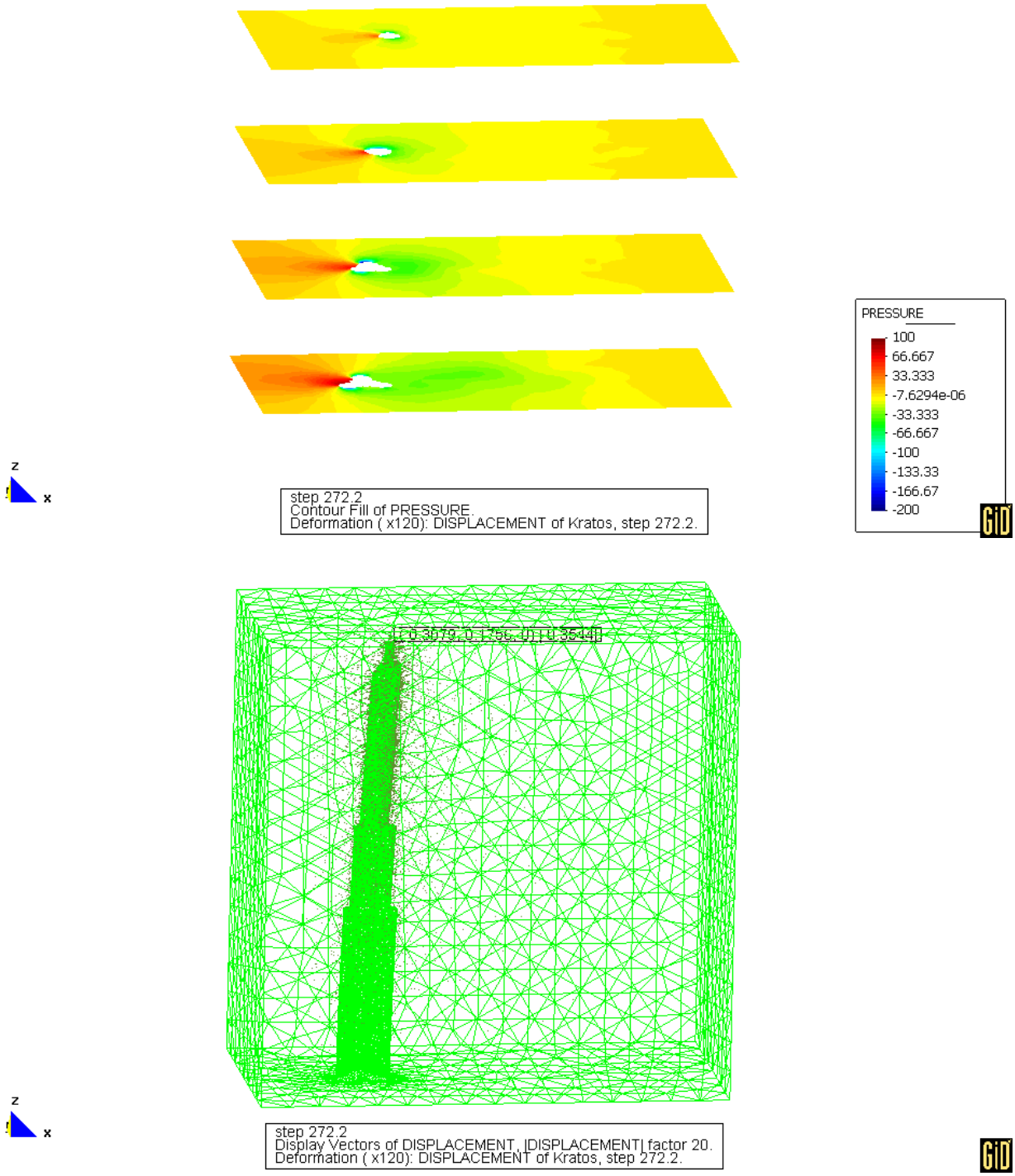

Figure 4.7: Pressure and displacement at time 272.2 s

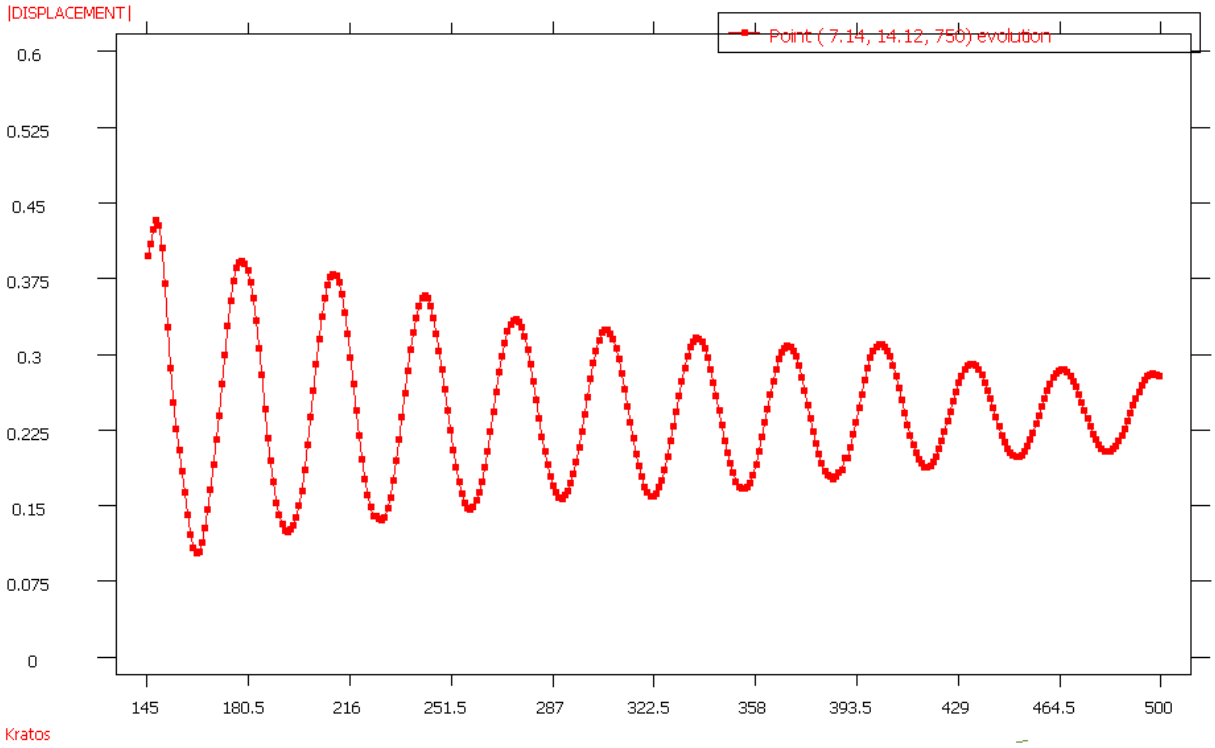

Figure 4.8: Burj Dubai Tower. Top displacement versus time

4.3 FSI analysis via coupling KRATOS, CARAT and MpCCI

In this section a strategy is set up for coupling the fluid solver in the code KRATOS with a structural solver in the code CARAT. The coupling is explicit using a sequential staggered scheme and non-conforming meshes, so each time step variables on the fluid side of the FSI interface has to be interpolated and transferred to the structure side and vice versa. For this purpose MpCCI (Mesh-based parallel Code Coupling Interface), developed at the Fraunhofer Institute SCAI, is used. MpCCI is a tool designed for the coupling of different simulation codes. A coupled simulation is the carried for a flow around an elastic cylinder.

4.3.1 Flow around an elastic cylinder

The fluid domain Ω_F is (1.5x1.0) m^2 with a circular hole $\phi = 0.0762$ m in the middle at the distance 0.5 m from the inflow at the left edge. The fluid is free to slip at the lower and upper edge but not at the circular hole, which constitutes the FSI interface Γ_{FS}. The inflow velocity is 16.6 m/s and at the outflow pressure is set to 0 Pa.

The thin-walled elastic cylinder is modeled in CARAT using geometrically nonlinear shell elements. At 4 points on the cylinder surface the tangential displacement is prescribed to zero, see Figure 4.9. In the first run the structure has the following properties: Young´s modulus $E = 11.26 \cdot 10^9$ N/m^2, Poisson´s ratio $\nu = 0.4$, density $\rho = 913.3$ kg/m^3 and a thickness of $t = 0.497$ mm.

The fluid has the properties of air, the flow has the Reynold´s number 75000 and the mesh consists of 8560 triangular elements of size $h = 0.001 - 0.015$ m, see Figure 4.10.

The pressure and the velocity for a certain time step is visualized in Figure 4.11. The flow shows an oscillatory behavior with a vortex shedding frequency of $f_s = 43.1$ Hz which gives a Strouhal number of $S = 0.198$. The Strouhal number corresponds well to experimental value $S = 0.194$ taken from [33]. The vortex shedding causes a periodic load on the cylinder transversal to the flow direction with the same frequency. Combined with the radial boundary conditions at 4 points this load enforces a vibrating ellipsoidal movement. In Figure 4.12 the pressure and the x-component of the displacement versus time is plotted at a reference point at the cylinder surface. This reference point lies 135 degrees counterclockwise from flow direction as shown in Figure 4.10. The amplitude of the vibration is approximately $4{\cdot}10^{-5}$ m. In Figure 4.13 the deformed cylinder is shown at two extreme points. The fourier transform of the x-displacement confirms this forced movement but also indicate presence of the higher frequency $f = 148$ Hz.

This frequency lies between 3 times f_s and the first eigenfrequency of the so-called ovalling effect $f_1 = 161$ s^{-1}. The ovalling effect of order k is the periodic oscillation of the cylinder with $k + 1$ wavelengths around its circumference, see [48] and [49].

Comparison is made to a simulation in [40] using the same geometry and material properties as above. Here the higher frequency does not occur. Instead a much cleaner vibration in the first mode can be observed. The amplitude of the displacement in the reference point is $3{\cdot}10^{-4}$ m. The Strouhal number in this simulation is $S = 0.243$.

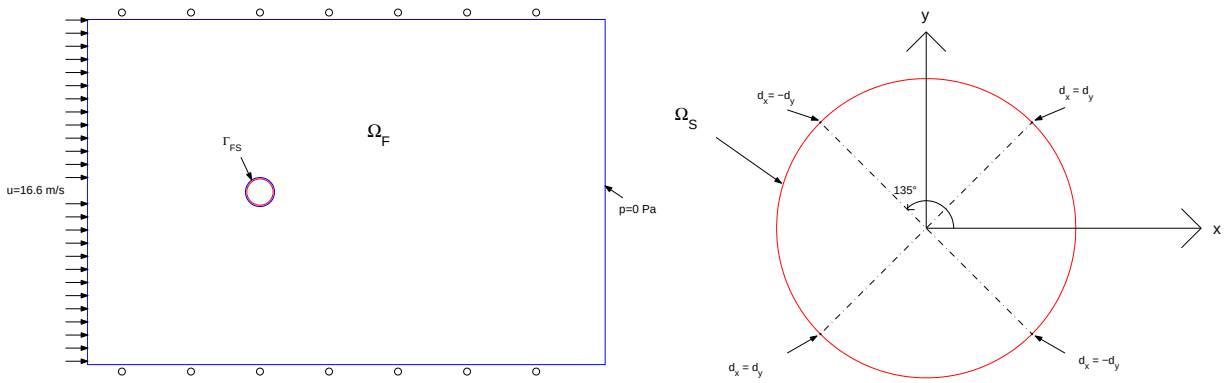

Figure 4.9: Flow around elastic cylinder. Geometry and conditions

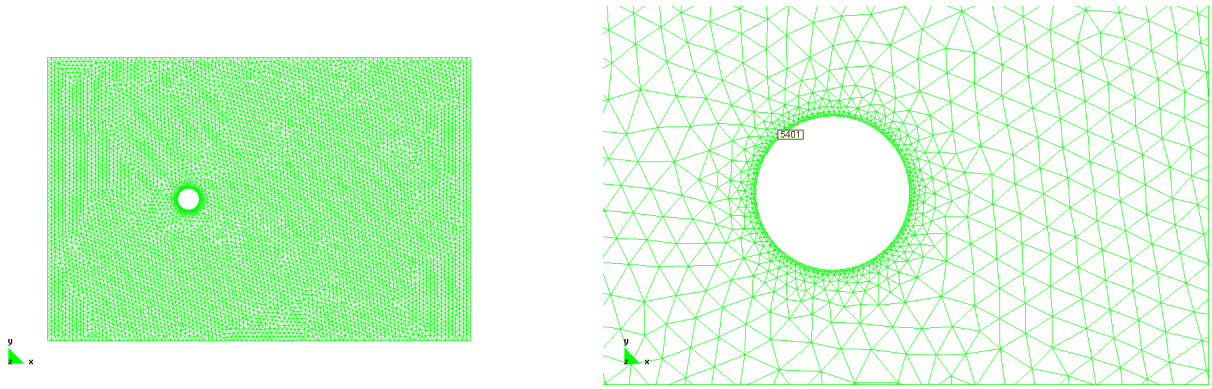

Figure 4.10: Fluid mesh

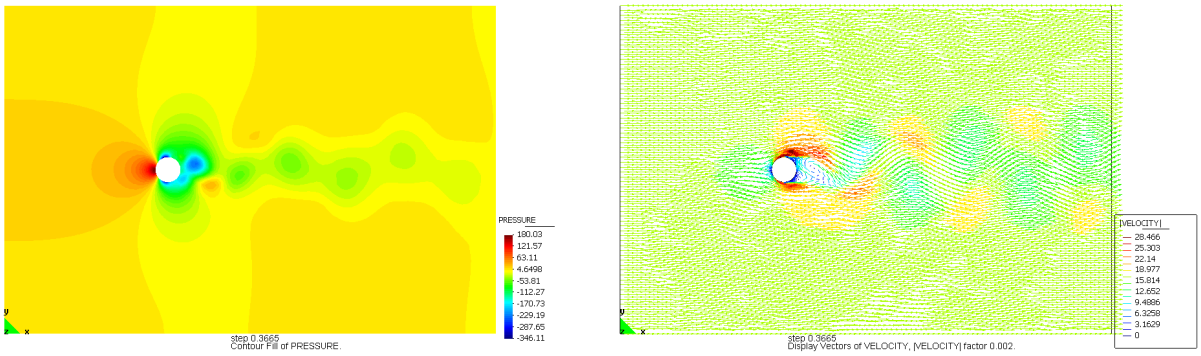

Figure 4.11: Pressure and velocity field at time $t = 0.3665$ s

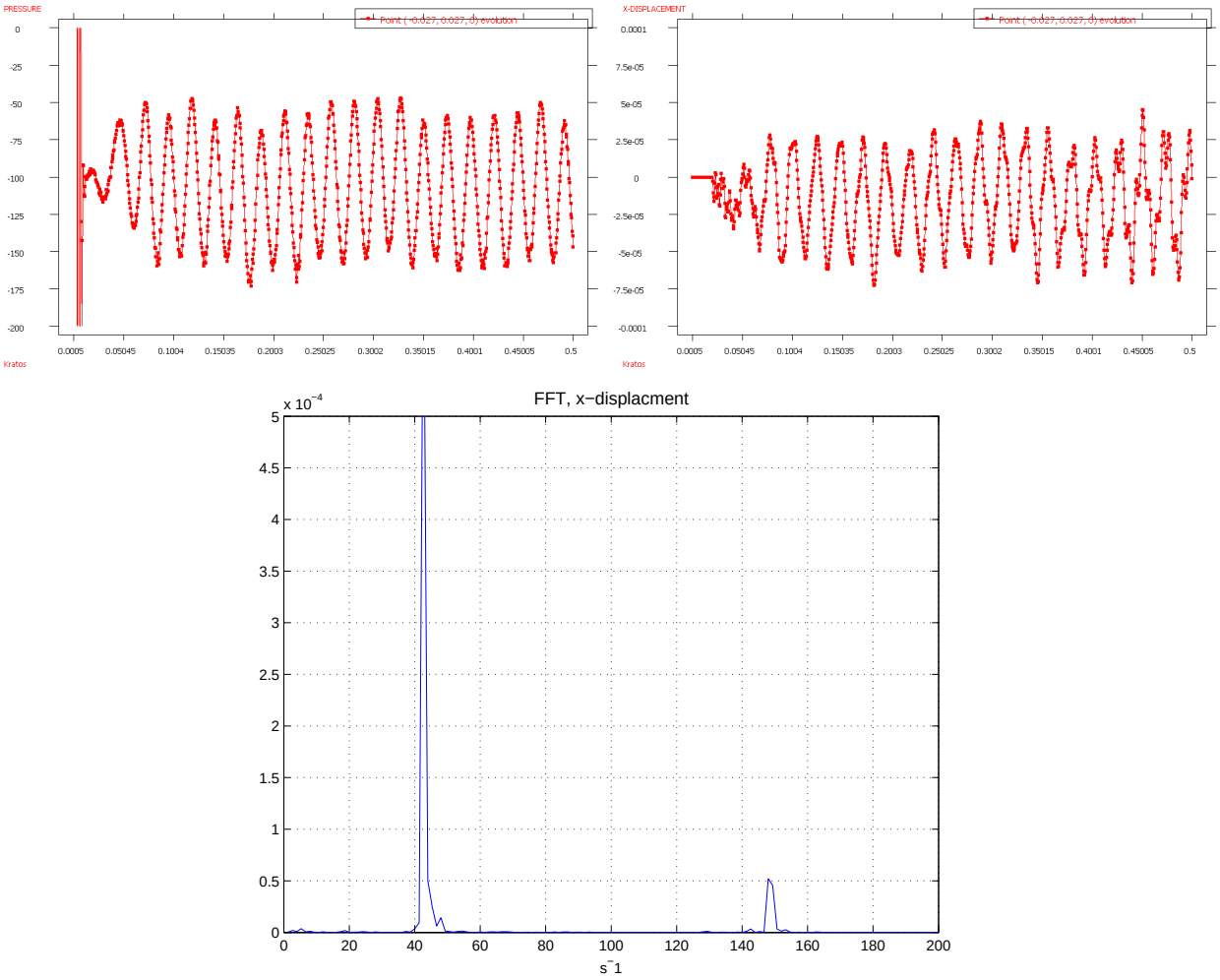

Figure 4.12: Above: Pressure and x-displacement versus time at point 5401. Below: FFT analysis of x-displacement

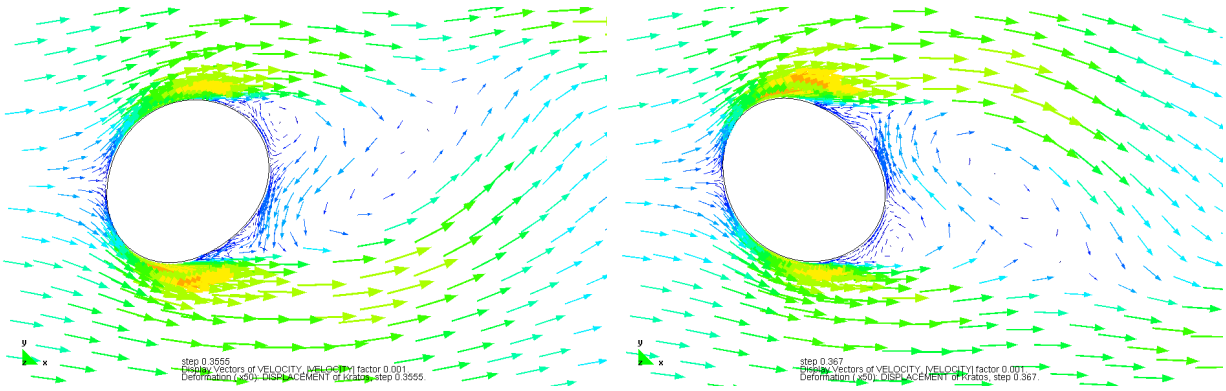

Figure 4.13: Velocity field around cylinder surface at time $t = 0.3555$ and $t = 0.367$. (Deformation amplified x 50)

In a second run the material properties of the structure are the following: $E = 15.58 \cdot 10^9$ N/m^2, $\nu = 0.4$, $\rho = 18000$ kg/m^3 and $t = 0.5$ mm. In this case resonance is obtained as the eigenfrequency of the ovalling effect in the first mode coincides with the shedding frequency, thus $f_1 = f_s = 43.1$ Hz. Figure 4.14 shows the pressure and displacement variation with time at the reference point 5401. Due to this resonance the amplitude is larger than in the previous run in spite the fact that that the structure is stiffer and significantly heavier. In figure 4.15 the deformation at two extreme points is plotted.

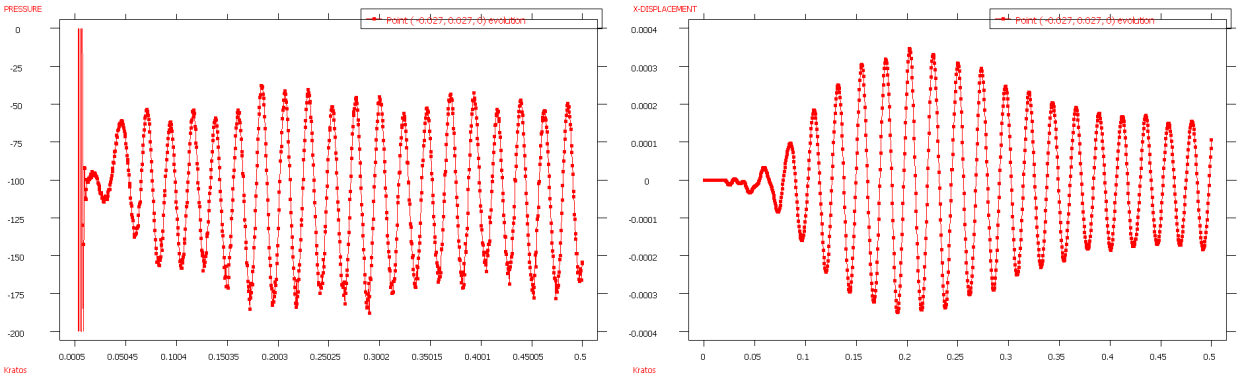

Figure 4.14: Pressure and x-displacement versus time at point 5401.

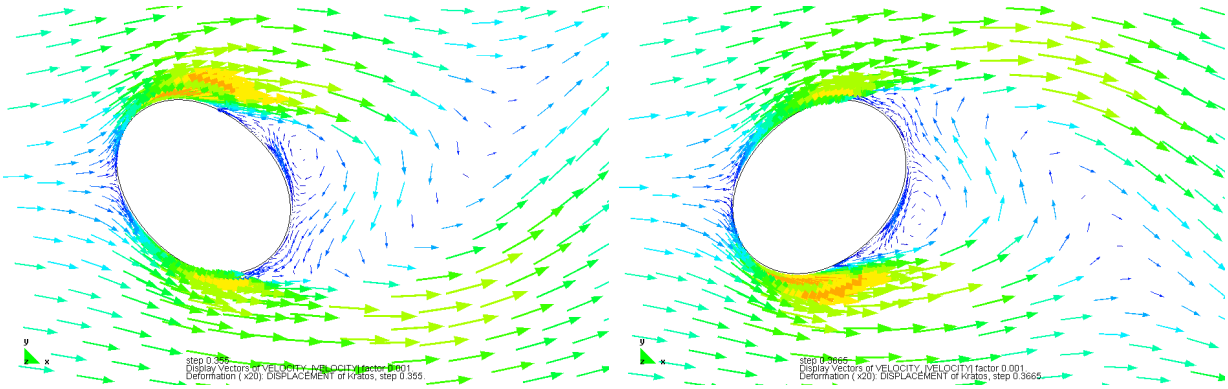

Figure 4.15: Velocity field around cylinder surface at time $t = 0.355$ and $t = 0.3665$. (Deformation amplified x 20)

A third simulation is carried out where the structure is modeled with total lagrangian elements and using conforming meshes, in accordance to the described FSI model in section 4.2.1. The material properties in this run coincide with the ones used in [40]: $E = 5.6 \cdot 10^8$ N/m^2, $\nu = 0.3$, $\rho = 18000$ kg/m^3 and $t = 0.5$ mm. The first 3 eigenfrequencies are $f_1 = 7.9$ Hz, $f_2 = 22.2$ Hz and $f_3 = 42.6$ Hz respectively corresponding to 2, 3 and 4 wavelengths along the cylinder circumference.

Figure 4.16 shows the radial displacement at the reference point 5401. Figure 4.17 shows the deformed cylinder at time instants $t = 3.565$ s and $t = 0.368$ s.

It is observed that $f_3 = 42.6$ Hz, which is very similar to the shedding frequency $f_s = 43.1$ Hz, is predominant in the FFT-diagram.

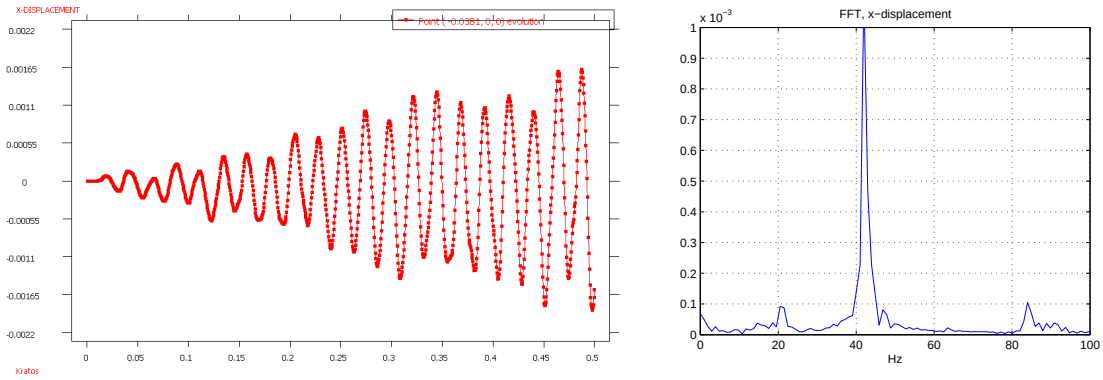

Figure 4.16: Radial displacement versus time at point 5401.

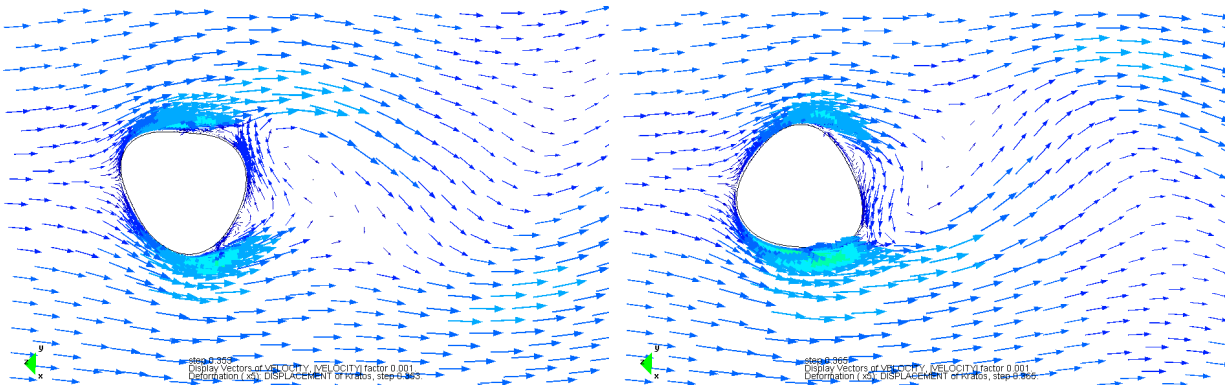

Figure 4.17: Velocity field around cylinder surface at time $t = 0.353$ and $t = 0.365$. (Deformation amplified x 5)

4.4 Concluding remarks

In this chapter, the FIC/FEM model developed in previous chapter is extended to an FSI model designed for aeroelastic problems involving airflow around a flexible structure. The structure is assumed to be much heavier than the air and therefore explicit coupling is used based on a sequential staggered algorithm. Furthermore, as airflow typically is of high Reynolds number the viscous forces at the interface are neglected. Only the pressure forces take part in the coupling. This defines the FSI model, which is tested using a geometrically non-linear solid as the structural part. The solid elements are of same shape as the fluid elements, triangles in 2D and tetrahedra in 3D, and the meshes are conforming.

For the application to the skyscraper Burj Dubai a simplified beam model is used instead of solid elements and the meshes are non-conforming. It shows that the model can simulate the dynamic behavior of large-scale ground structures.

Finally, using the nonlinear shell model in CARAT and coupling it to the FSI model in KRATOS, airflow around an elastic cylinder is simulated. The ovalling phenomena can be observed in the flow-induced vibrations of the cylinder. Furthermore, the success in coupling the FSI model with a structural model from another code indicates the possibility of simulating more FSI problems within aeroelasticity where highly specialized modeling of the structure is required.

Chapter 5

Conclusions

In this monograph the main objective has been to develop a numerical method for solving the incompressible Navier-Stokes equations by means of the finite element method (FEM). This has been achieved by adapting the Finite Calculus (FIC) technique and the well known problems with numerical instabilities associated with these equations have been solved. These include oscillations in the velocity field due to a dominant convection term and oscillations in the pressure field due to the incompressibility condition.

As the numerical solution of the convection-diffusion equation also is subject to the first of these sources of instabilities, oscillations in the solution field due to a dominant convection term, a whole chapter has been dedicated to this equation. Here the FIC method in the principle curvature directions has been implemented and tried out using elements with linear as well as quadratic interpolation. Comparison with other standard stabilization methods has been made. Using linear elements the principle curvature directions are approximated with the gradient of the solution and excellent results have been obtained. This is also reported from other authors in this field using the FIC approach, for example in [7]. As for the quadratic elements and using the actual principle curvatures, which is a new feature, in general the results are also fine. But for some examples linear elements are more suitable, it depends on the problem type. The use of quadratic elements for the FIC model still requires some further investigation before it is safe to apply it to more complex problems. As the FIC model for the convection diffusion problem in this monograph first was to be extended to an incompressible fluid model and then also involving fluid-structure interaction, this has been done using linear elements. Another reason for this choice is that linear elements are computationally cheaper.

However, before the actual FIC/FEM fluid model was set up, the implementation of the incompressible Navier-Stokes equations has been carried out using the GLS-method. Like the FIC method, GLS is a stable method and equal order interpolations of the pressure and the velocity can be employed. Here linear as well as quadratic interpolation is used. The GLS/FEM model allows flows in the laminar regime to be simulated which are of relatively low Reynolds numbers. The equations are written in an ALE framework and a mesh moving strategy is provided.

As the next step the FIC/FEM fluid model has been implemented using linear elements. It has already been concluded that its features provide the necessary stabilization for the convection term as well as for the incompressibility condition, allowing equal order interpolations of the velocity and the pressure. Moreover, one of its intrinsic characteristics

is that it filters turbulent flow fields without having to introduce any additional turbulence model. This makes the model suitable also for flows with high Reynolds numbers. This is of major importance as the modeling of air flows has been addressed in order to deal with aeroelastic problems using a fluid-structure interaction (FSI) model. For this purpose a sequential staggered algorithm for FSI has been introduced. This obliges the structure to be much more dense than the fluid but this is a reasonable assumption for large-scale structures surrounded by air. The dynamic behavior of the skyscraper Burj Dubai subjected to wind load has been simulated. Finally the FSI model in KRATOS has been coupled to a structural solver in CARAT and the ovalling phenomena is observed for an elastic cylinder interacting with surrounding airflow. The use of code coupling is indeed a promising task and will open up doors for new challenging FSI applications where highly specialized solvers are required for both the fluid and the structure.

Bibliography

[1] Codina R. A Finite Element Formulation for the Numerical Solution of the Convection-Diffusion Equation. Monograph 14, CIMNE, January 1993.

[2] Codina R. Comparison of some Finite Element Methods for Solving the Diffusion-Convection-Reaction Equation. *Computer Methods in Applied Mechanics and Engineering* 156 (1998) 185-210.

[3] Hughes T.J.R. Feijoo G.R. Mazzei L. Quincy J.B. The Variational Multiscale Method-a Paradigm for Computational Mechanics. *Computer Methods in Applied Mechanics and Engineering* 166 (1998) 3-24.

[4] Camprubí N. Colominas I. Navarrina F. Casteleiro M. Galerkin, Least-Squares and G.L.S. Numerical Approaches for Convective-Diffusive Transport Problems in Engineering. *European Congress on Computational Methods in Applied Sciences and Engineering*, Barcelona, 11-14 September 2000.

[5] Oñate E. Manzan M. Stabilization Techniques for Finite Element Analysis of Convection-Diffusion Problems. Publication 183, CIMNE, February 2000.

[6] Oñate E. Multiscale Computational Analysis in Mechanics Using Finite Calculus: an Introduction. *Computer Methods in Applied Mechanics and Engineering* 192 (2003) 3043-3059.

[7] Oñate E. Zárate F. Idelsohn S.R. Finite Element Formulation for Convective-Diffusive Problems with Sharp Gradients Using Finite Calculus. *Computer Methods in Applied Mechanics and Engineering* 195 (2006) 1793-1825.

[8] Oñate E. Possibilities of Finite Calculus in Computational Mechanics. *International Journal for Numerical Methods in Engineering* 60 (2004) 255-281.

[9] Codina R. A Discontinuity-Capturing Crosswind Dissipation for the Finite Element Solution of the Convection-Diffusion Equation *Computer Methods in Applied Mechanics and Engineering* 110 (1993) 325-342.

[10] Donea J. Huerta A. Finite Element Methods for Flow Promblems. *Whiley*, 2003.

[11] Codina R. Blasco J. A Finite Element Formulation for the Stokes Problem Allowing Equal Velocity-Pressure Interpolation. *Computer Methods in Applied Mechanics and Engineering* 143 (1997) 373-391.

[12] Codina R. A Stabilized Finite Element Method for Generalized Stationary Incompressible Flows. *Computer Methods in Applied Mechanics and Engineering* 190 (2001) 2681-2706.

[13] Codina R. Pressure Stability in Fractional Step Finite Element Methods for Incompressible Flows. *Journal of Computational Physics* 170 (2001) 112-140.

[14] Idelsohn S.R. Oñate E. Del Pin F. The Particle Finite Element Method: A Powerful Tool to Solve Incompressible Flows with Free-surfaces and Breaking Waves. *International Journal for Numerical Methods in Engineering* 61 (2004) 964-989.

[15] Donea J. Huerta A. Ponthot J.-Ph. Rodríguez-Ferran A. Arbitrary Lagrangian-Eulerian Methods. *The Encyclopedia of Computational Mechanics* 1 (2004) 413-437.

[16] Fourestey G. Piperno S. A Second-Order Time-Accurate ALE Lagrange-Galerkin Method Applied to Wind Engineering and Control of Bridge Profiles. *Computer Methods in Applied Mechanics and Engineering* 193 (2004) 4117-4137.

[17] Hermann L.R. Laplacian-Isoparametric Grid Generation Scheme. *Journal of the Engineering Mechanics Division of the ASCE* 102 (1976) 749-756.

[18] Oñate E. García J. A Finite Element Method for Fluid-Structure Interaction with Surface Waves using a Finite Calculus Formulation. *Computer Methods in Applied Mechanics and Engineering* 191 (2001) 635-660.

[19] Oñate E. García J. Bugeda G. Idelsohn S.R. A General Stabilized Formulation for Incompressible Fluid Flow Using Finite Calculus and the Finite Element Methods. Publication 223, CIMNE, March 2003.

[20] Harvey S.H.L. Overview of Turbulent Flows. Mechanical Engineering, Stanford University, February 2004.

[21] Wang M. Catalano P. Iaccarino G. Prediction of High Reynolds Number Flow over a Circular Cylinder using LES with Wall Modeling. *Center for Turbulence Research, Annual Research Briefs* (2001) 45-50.

[22] Hughes T.J.R. Mazzei L. Jansen K.E. Large Eddy Simulation and the Variational Multiscale Method. *Computing and Visualization in Science* 3 (2000) 47-59.

[23] Gravemeier V. The Variational Multiscale Method for Laminar and Turbulent Incompressible Flow. PhD Thesis, University of Stuttgart.

[24] Valls A. García J. Oñate E. LES Turbulence Models. Relation with Stabilized Numerical Methods. CIMNE.

[25] Oñate E. Valls A. García J. FIC/FEM Formulation with Matrix Stabilizing Terms for Incompressible Flows at Low and High Reynolds Numbers. *Computational Mechanics* 38 (2006) 440-455.

[26] Cruchaga M.A. Oñate E. A Finite Element Formulation for Incompressible Flow Problems Using a Streamline Operator. *Computer Methods in Applied Mechanics and Engineering* 143 (1997) 49-67.

[27] Armaly B.F. Durst F. Pereira J.C.F. Schönung B. Experimental and Theoretical Investigation of Backward-Facing Step Flow. *Journal of Fluid Mechanics* 127 (1983) 473-496.

[28] Ghia U. Ghia K.N. Shin C.T. High-Re Solutions for Incompressible Flow Using the Navier-Stokes Equation and Multigrid Method. *Journal of Computational Physics* 48 (1982) 387-411.

[29] Tanaheshi T. Okanaga H. Saito T. GSMAC Finite Element Method for Unsteady Incompressible Navier-Stokes Equation at High Reynolds Numbers. *International Journal for Numerical Methods in Fluids* 11 (1990) 479-499.

[30] Kalro V. Tezduyar T. Parallel 3D Computation of Unsteady Flows around Circular Cylinders. *Parallel Computing* 23 (1997) 1235-1248.

[31] Bochev P. Least-Squares Methods for the Navier-Stokes Equations: Trends and Development. Department of Mathematics, University of Texas, Arlington.

[32] Strouhal V. Über eine besondere Art der Tonerregung. *Vorgetrag bei der physikalisch-medizinischen Gesellschaft*, Würzburg, 16 February 1878.

[33] Norberg C. Effect of Reynolds Number and a Low-Intensity Freestream Turbulence on the Flow Around a Circular Cylinder. Department of Applied Thermodynamics and Fluid Mechanics, Chalmers University of Technology, Göteborg, May 1987.

[34] Chopra A.E. Dynamics of Structures. *Prentice Hall*, New Jersey, 1995.

[35] Ohayon W. Felippa . Advances in Computational Methods for Fluid-Structure Interaction and Coupled Problems. *Computer Methods in Applied Mechanics and Engineering* 190 (2001) 2977-2978.

[36] Dettmer W. Peric D. A Computational Framework for Fluid-Structure Interaction: Finite Element Formulation and Applications. *Computer Methods in Applied Mechanics and Engineering* 195 (2006) 5754-5779.

[37] Lund E. Møller H. Jakobsen L.A. Shape Design Optimization of Steady Fluid-Structure Interaction Problems with Large Displacements. *American Institute of Aeronautics and Astronautics* 2001-1624.

[38] Farhat C. Lesoinne M.W. Two Efficient Staggered Algorithms for the Serial and Parallel Solution of Three-Dimensional Nonlinear Transient Aeroelastic Problems. *Computer Methods in Applied Mechanics and Engineering* 182 (2000) 499-515.

[39] Ramm E. Wall W.A. Interaction of Fluids and Thin Structures. *European Conference on Computational Mechanics*, Cracow, 26-29 June 2001.

[40] Bletzinger K.-U. Wüchner R. Kupzok A. Algorithmic Treatment of Shells and Free Form Membranes in FSI. *Lecture Notes in Computational Science and Engineering* 53 (2006) 336-355.

[41] Wüchner R. Bletzinger K.-U. Stress-Adapted Numerical Form Finding of Pre-Stressed Surfaces by the Updated Reference Strategy. *International Journal for Numerical Methods in Engineering* 64 (2005) 143-166.

[42] Dadvand P. A Framework for Developing Finite Element Codes for Multi-Disciplinary Applications. PhD Thesis, Technical University of Catalonia, Barcelona, July 2007.

[43] Badia S.I. Stabilized Pressure Segregation Methods and their Application to Fluid-Structure Interaction Problems. PhD Thesis, Technical University of Catalonia, Barcelona, December 2005.

[44] Rossi R. Light weight Structures: Structural Analysis and Coupling Issues. PhD Thesis, University of Bologna, May 2005.

[45] Andersen T. Ardeberg A. Owner-Petersen M. Design Study of a 50 m Adaptive Optics Telescope. *www.astro.lu.se/ torben/euro50/index.html* Lund Observatory, Lund, August 2003.

[46] Codina R. Morton C. Oñate E. Soto O. Numerical Aerodynamic Analysis of Large Buildings using a Finite Element Model with Application to a Telescope Building. *International Journal of Numerical Methods for Heat & Fluid Flow* Vol. 10 No. 6 (2000) 616-633.

[47] Marshall S. Software Engineering: Engineering Failures: Tacoma Narrows. *www.vuw.ac.nz/staff/stephen_marshall/SE/Failures/SE_Tacoma.html* Wellington, May 2002.

[48] Johns D.J. Sharma C.B. On the Mechanism of Wind-Excited Ovalling Vibrations of Thin Circular Cylindrical Shells. *Naudascher E. Flow-induced Structural Vibrations* Springer Verlag, Berlin, 1974.

[49] Israel U. Strömungsinduzierte Ovallingschwingungen von Zylinderschalen: Theorie und Numerische Simulation unter Berücksichtigung der Fluid-Struktur-Interaktion. Diplomarbeit, Technische Universität München.